Electrochemical investigations into Electrode directed Taxis and Extracellular Electron Transfer Mechanisms of *Shewanella oneidensis* MR-1

Joseph John Oram

Submitted in accordance with the requirements for the degree of

Doctor of Philosophy

The University of Leeds

School of Biomedical Sciences

December 2017

The candidate confirms that the work submitted is his own, except where work which has formed part of jointly authored publications has been included. The contribution of the candidate and the other authors to this work has been explicitly indicated below. The candidate confirms that appropriate credit has been given within the thesis where reference has been made to the work of others.

The chapters within the thesis that have been based on work from jointly authored publications are chapters 2, 3, and 4.

Chapters 2 and 4

Oram, J., and Jeuken L. J. C. (2017). *Shewanella oneidensis* MR-1 electron acceptor taxis and the perception of electrodes poised at oxidative potentials, *Curr. Op. Electrochem*. 5, 99-105.

Joseph Oram reviewed the literature and wrote the manuscript. L. J. C. Jeuken provided guidance, and contributed to the discussion and the writing of the manuscript.

Chapter 3

Oram, J., and Jeuken L. J. C. (2016). A re-evaluation of electron transfer mechanisms in microbial electrochemistry: Shewanella releases iron that mediates extracellular electron transfer. *ChemElectroChem*, **3**, 829-835.

Joseph Oram prepared the samples (Suspensions of microaerobically grown bacteria and modified electrodes), planned and conducted the electrochemical experiments, analysed the experimental data, and wrote the manuscript. L. J. C. Jeuken provided guidance regarding the design of experiments, data analysis, and contributed to the discussion and the writing of the manuscript.

Acknowledgements

I would like to thank my supervisors, Professor Lars Jeuken and Dr Kevin Critchley, for their advice and support during my PhD. Additional thanks go to Professor Paul Millner for his advice and useful tips.

For their technical and moral support, I would like to thank Theodoros Laftsoglou, Dr Valentin Radu, Thanisorn Mahatnirunkul (Ploy), Matthias Gantner, Dr Vlad Vasilca, Dr Mengqiu Li, Anna Wroblewska-Wolna, Dr Ee Taek Hwang, Dr Sunjie Ye, Dr George Heath, Dr Khizar Sheikh, Riitta Partanen, and Honglin Rong.

Finally, I would like to thank my family for their unconditional support.

Even more finally, many special thanks go to Wai Yi Wong and my mum Dr Catherine House.

Abstract

Shewanella oneidensis MR-1 is capable of respiring on an extraordinarily large and diverse array of terminal electron acceptors, including extracellular insoluble metal oxides and electrodes. The ability to perform extracellular electron transfer (EET) has sparked great interest in MR-1 which has become both a model organism for fundamental research into EET and a candidate microbe for microbial electrochemical systems. Here, cyclic voltammetry was used to determine the relationship between the surface chemistry of electrodes (modified gold, ITO and carbon) and the EET mechanism. On ultra-smooth gold electrodes modified with self-assembled monolayers containing carboxylic acid terminated thiols, an EET pathway dominates with an oxidative onset at 0.1 V (SHE). Addition of the siderophore deferoxamine abolishes this signal, leading us to conclude that this pathway proceeds via an iron mediated electron transfer (MET) mechanism. The same EET pathway is observed on other electrodes but the onset potential is dependent on the electrolyte composition and electrode surface chemistry. EET pathways with onset potentials above -0.1 V (SHE) have previously been ascribed to direct electron transfer (DET) mechanisms via outer membrane cytochromes (MtrC/OmcA). We propose that the previously identified DET mechanisms of MR-1 need to be re-evaluated.

It has been proposed that MR-1 could use flavins for locating insoluble electron acceptors, including electrodes. To assess the role of flavins in MR-1 taxis towards electrodes we performed video microscopy cell tracking using a specifically designed capillary cell and tracking algorithm suited to low frame rates. Analysis of trajectories from WT MR-1 and mutants (*ΔmtrC/ΔomcA* and *Δbfe*), showed that MR-1 had a tactic response towards electrodes poised above the midpoint potential of riboflavin (> -0.15 V vs SHE) and a negative response on switching to potentials below the midpoint potential (< -0.25 V vs SHE). The Mtr EET pathway was essential for this response.

Table of Contents

List of Tables

List of Schemes

List of Figures

List of abbreviations

EET - extracellular electron transfer

ET - electron transfer

DET - direct electron transfer

MET - mediated electron transfer

CV - cyclic voltammetry/voltammogram

EIS - electrochemical impedance spectroscopy

MR-1 - *Shewanella oneidensis* MR-1

SHE - standard hydrogen electrode

ITO - Indium tin oxide

SAM - self assembled monolayer

TSG - template striped gold

LB - Lysogeny broth

OCP - open circuit potential

MOPS - 3-(N-morpholino)propanesulfonic acid

EDTA - ethylenediaminetetraacetic acid

MFC - microbial fuel cell

MES - microbial electrochemical system

1. Introduction

Shewanella are a diverse genus of facultative anaerobic gram negative bacteria that thrive in a range of marine and freshwater environments. The variation in environments *Shewanella* occupy can be attributed to their ability to utilise an unparalleled array of dissimilar terminal electron acceptors in the absence of oxygen. Their ecological roles are equally diverse and *Shewanella* has been implicated in biogeochemical metal cycling, corrosion, subsurface bioremediation, food spoilage, opportunistic pathogenicity and symbiotic relationships. In addition, multiple *Shewanella* species are employed in research, for fundamental studies in extracellular electron transfer and potential use in biotechnological applications, including biosensing and energy production. From the *Shewanella* genus, *Shewanella oneidensis* MR-1 (MR-1) is a strain of particular notability and, since its discovery in 1988, it has become a model organism for extracellular electron transfer and microbial fuel cells (MFC) [1-3].

The first species of *Shewanella* to be encountered was *Shewanella putrefaciens* which was discovered in 1931 by Derby and Hammer from a sample of tainted Canadian butter. Originally this new organism was designated *Achromobacter putrefaciens* [4] after which it was reclassified numerous times due to biochemical advances, firstly to *Pseudomonas* in 1941 and then *Alteromonas* in 1977. But it was not until 1985 that the organism was given the new genus *Shewanella* by MacDonell and Colwell [5].

Since the discovery of the first *Shewanella*, approximately 50 additional species have been classified under the same genus [6]. Collectively, species of the *Shewanella* genus are able to utilise over 20 different terminal electron acceptors including, insoluble minerals containing metals and metal oxides, sulphur compounds, nitrates, and organic compounds [7]. The diversity in terminal electron acceptors allows *Shewanella* to respire in almost any environment [8]. Growth at low temperatures is another hallmark of *Shewanella* with many able to grow at temperatures below 5°C even though their optimal growth temperature is significantly higher (e.g. 30 °C in the case of MR-1) [8]. This unusual ability of Shewanella to adapt to much lower temperatures than their ideal is not fully understood and is likely to be the result of multiple factors. In general, subjection of bacterial species with ideal temperatures around 30 °C to low temperatures (< 5 °C) would severely affect their respiration. At low temperatures, phospholipid fatty acids in the membrane transition from a fluid phase into a more rigid gel phase which retards the essential interaction between quinones and redox active membrane proteins. It is thought many Shewanella disturb the gel transition of their lipid bilayers by increasing the amount of short highly branched lipids (supress the transition temperature) along with incorporating eicosapentaenoic acid into their bilayers (disrupt gel phase islands) [9, 10].

As mentioned, MR-1 is a model organism which has been employed extensively for studying EET mechanisms and evaluating potential MES applications [11, 12]. MR-1's role as a model organism for EET is shared with species from the *Geobacter* genus [13-15]. *Geobacter* sp. generally yield higher current densities in MES but, as obligate anaerobes, stringent culture conditions are required [16]. In contrast, MR-1 is a facultative anaerobe thus exposure to oxygen is not detrimental and consequently MR-1 is easier to work with. MR-1 is also capable of transferring electrons to an unmatched array of terminal acceptors making it an attractive choice for mechanistic studies into respiration and EET.

1.1 Microbial Electrochemical Systems (MES)

The necessity for alternative energy sources along with reducing the energy requirements and cost of wastewater treatment was an early driving force behind research into MR-1 and other exoelectrogens. The general idea was to employ EET capable organisms in MFCs which can break down undesirable organic matter in wastewater whilst generating electrical power. A basic MFC design (**figure 1.1**) consists of two separated compartments, each with an electrode connected to the other by an electrical circuit. The compartments are commonly separated using an ion or proton exchange membrane to prevent exchange of dissolved gasses (e.g. oxygen and hydrogen). One of the compartments contains an anaerobic suspension including exoelectrogenic bacteria and a metabolisable carbon/electron source (e.g. organic material in waste water) [17, 18]. For the other compartment a sustainable oxidiser is required (e.g. oxygen). The electrode in the anaerobic compartment with exoelectrogenic bacteria functions as the anode whilst the electrode exposed to the oxidiser functions as the cathode. Bacteria in the anode chamber oxidise/metabolise carbon sources, generating an excess of electrons and protons in the process. A relatively negative potential is then generated at the anode surface by transfer of elections from respiring exoelectrogenic bacteria to the anode through mediators or directly through outer membrane cytochromes. At the cathode, electrons are transferred out of the electrode to the oxidiser, generating a positive charge/potential. In the case with oxygen as the oxidiser, protons built up in the anaerobic chamber and diffuse across a proton exchange membrane into the cathode chamber where they combine with oxygen on the cathode surface in a redox reaction to form water. The net potential difference between anode and cathode can then be used for useful work.

There has been substantial development in MFC technologies since their original inception, but their use remains very limited in practical applications, particularly those concerning energy production, mainly due to low power output along with high internal resistances and prohibitive material costs (required for cathodes of the more efficient MFCs) [3, 19, 20]. Typical MFCs for waste water treatment can at best produce power densities between 0.1-0.5 W/m^2 [3, 21]. Crucially, MFC power output tends to scale poorly with increasing reactor volumes. Power densities of MFC with reactor volumes 1 L or greater fall below the required threshold for feasibility in industrial applications such as recovering energy from organic material in wastewater [17, 22]. Difficulties and limitations in improving the efficiency of MFC's have, in part, led to a diversification in the potential applications being explored, leading to an explosion in numbers of related devices collectively known as microbial electrochemical systems (MES). Potential MES applications range from bioremediation and waste water treatment to microbial electrosynthesis and biosensing, all of which fundamentally rely on the EET ability of certain microbes.

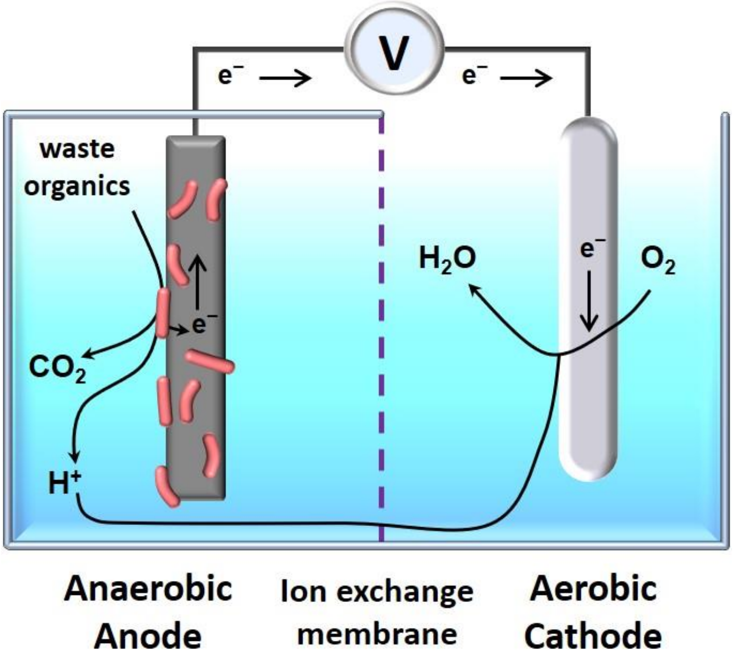

Figure 1.1 Cartoon of a basic Microbial Fuel Cell.

1.2 Electron Transfer across the Periplasm

S. oneidensis MR-1 is used as a model organism for biotechnological applications, especially those relating to bioelectronics, due to its ability to transfer electrons to a large array of terminal acceptors including insoluble minerals and electrodes. Here the term bioelectronics refers to electronic technologies and devices which incorporate biological mater and/or are inspired by biological processors and architecture (MFC and biosensors are examples of bioelectronic devices) [23]. Most of the biotechnological avenues pursued for *Shewanella,* utilise or manipulate the bacteria's ability to transfer electrons outside of the cell to insoluble electron acceptors such as metallic or carbon based electrodes. It is therefore imperative to understand the mechanism by which this occurs. For gram negative bacteria such as *Shewanella*, to reduce insoluble extracellular electron acceptors they must possess capabilities for transferring electrons from their cytoplasmic membrane quinone pool to terminal reductases in their outer membrane. Therefore they require a system for passing electrons across the 10 - 25 nm wide periplasmic space [24-26]. The mechanism by which this happens has been studied extensively in *S. oneidensis* MR-1, but as of yet, has not been fully elucidated [27-31].

During anaerobic respiration the cytoplasmic membrane cytochrome CymA links the oxidation of quinones from the cytoplasmic membrane to the reduction of several periplasmic terminal reductases (e.g. fumarate reductase cytochrome c) and electron transfer proteins (e.g. small tetrahaem cytochrome c and MtrA) [32]. However, during extracellular respiration it is unclear whether CymA directly reduces MtrA or indirectly by first reducing other periplasmic redox proteins or if both occur concurrently (**figure 1.2)**. MtrA forms a multiprotein complex with an outer membrane spanning barrel protein, MtrB, along with outer membrane terminal reductases MtrC and OmcA. This complex allows for electron transfer from MtrA to the outer membrane terminal reductases [30]. The outer membrane reductases can either directly or indirectly (via soluble electron shuttles, e.g. flavins) reduce insoluble electron acceptors such as metal oxides [11, 30].

Two of the most abundant periplasmic proteins found during anaerobic growth, small tetrahaem cytochrome c (STC/CctA) and the flavocytochrome, fumarate reductase cytochrome c (FccA), are both up regulated during extracellular respiration implying they may be involved in periplasmic electron transfer [29, 33, 34]. However, evidence from individual gene deletion mutants is ambiguous. Extracellular respiration is affected by knock-out mutants but neither mutant results in the total annihilation of extracellular respiration. It has therefore not been possible to confirm a distinct phenotype for extracellular reduction [35].

Fonseca *et al* [35] used NMR spectroscopy to study protein-protein interactions in an attempt to provide some insight on the shrouded mechanism by which MR-1 transfers electrons across the periplasm. The group carried out NMR docking studies of the most abundant periplasmic proteins including STC and FccA. Their results showed CymA to have weak interactions with both STC (K_d = 250 µM) and FccA (K_d = 398 µM), indicating the formation of weak transient complexes. This is suggestive of a high turnover rate between CymA and interacting proteins. MtrA, which is clearly implicated in extracellular metal reduction [36], was similarly found to interact with STC and FccA. Interestingly, although FccA and STC have overlapping redox potentials and interaction partners, no interaction was found between them implying two segregated electron transfer pathways. Bruno *et al* pointed out that both FccA and STC have very negative surfaces at regions relevant to electron transfer. Electrostatic repulsion could therefore explain for the lack of interaction between these proteins [35].

The evidence from Fonseca *et al* for interactions between FccA:CymA and FccA:MtrA supports the hypothesis by Schuetz *et al* [27] that FccA's main role under certain conditions is to act as an electron buffer. This could potentially enable MR-1 to temporarily continue utilising a carbon/electron source when no terminal electron acceptor is available. At times when the electron transfer to terminal electron acceptors is slow and becomes the rate limiting step in respiration, FccA could take up excess electrons from either CymA or MtrA. This would prevent stalling of the respiratory chain due to limiting terminal electron transfer reactions. This hypothesis would explain why wild type MR-1 grows better than *Δfcca* mutants even when ferric iron is the sole electron acceptor. It is plausible that STC could have a similar role and would explain why these two periplasmic proteins are excessively expressed in MR-1 during extracellular respiration. Currently, through deletion mutants, STC has been shown to have a modulatory role in DMSO, ferrous citrate and flavin reduction but is not vital for any of them [37]. As flavins are reduced by MtrC/OmcA and MtrA is responsible for transferring electrons to MtrC/OmcA, it is probable that STC acts as an electron shuttle between CymA and MtrA. It should be noted that CymA has been observed to directly interact with MtrA without the need for other periplasmic proteins such as STC [15, 27]. It is widely thought that direct electron transfer between CymA and MtrA is the primary pathway across the periplasm during extracellular respiration. Additionally, evidence suggests that MtrA, while complexed to MtrB, could protrude sufficiently into the periplasm to interact directly with CymA [38] (**figure 1.2)**.

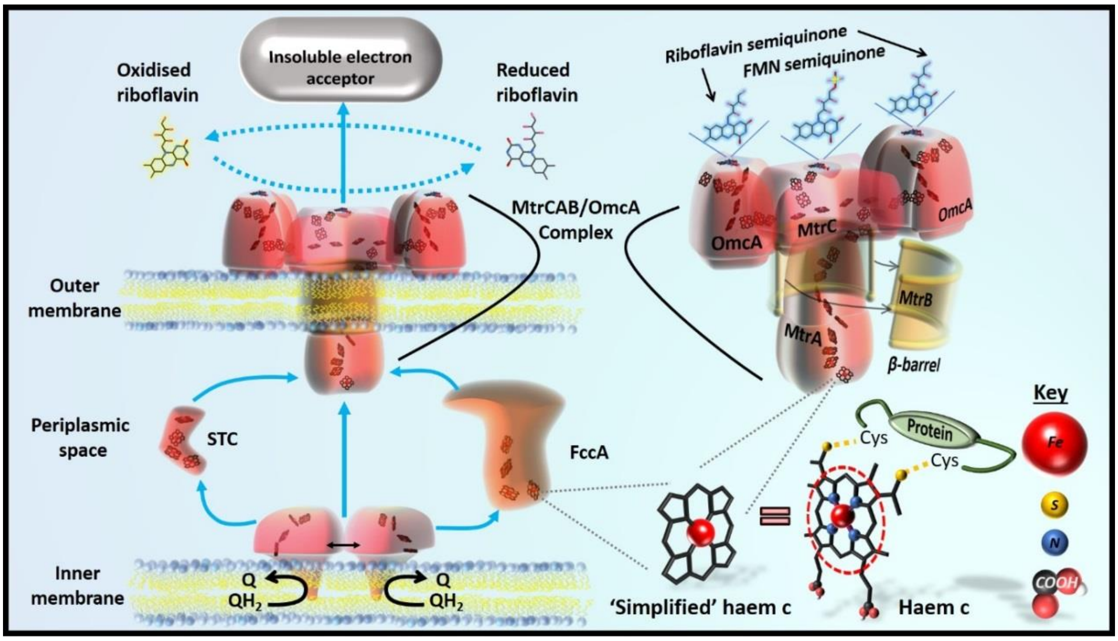

Figure 1.2 – Diagram depicting the flow of electrons across the MR-1 periplasmic space during extracellular respiration of an insoluble electron acceptor. Blue arrows indicate possible electron transfer pathways. C-type haems are highlighted within the relevant proteins (CymA, FccA, and STC are comprised of 4 haems each, while MtrA, MtrC, and OmcA have 10 haems each). MtrC and OmcA are thought to employ the semiquinone form of riboflavin and FMN respectively as cofactors (the semiquinone form of flavins is highlighted in blue). It is worth also noting that FccA also employs FAD as a co-factor (not shown). Two monomers of CymA are shown side by side with a double headed arrow to indicate a reversible dimer.

1.3 Extracellular Electron Transfer (EET) by MR-1

Once respiratory electrons reach the terminal reductases (MtrC/OmcA), they can be relayed on to insoluble electron acceptors (e.g. electrodes). Currently the are three different mechanisms proposed to achieve this; 1) direct electron transfer (DET) between outer membrane cytochromes and insoluble electron acceptors, [39, 40] 2) long ranged DET through conductive 'wires' formed by extrusions of the outer membrane and periplasm[41, 42]; electrons are thought to "hop" between cytochromes which decorate these membrane extrusions, and 3) mediated electron transfer (MET) achieved through self-secreted redox mediators, in particular riboflavin (RF) and flavin mononucleotide (FMN), which shuttle electrons between the outer membrane cytochromes and electrodes. [43]. Both MET and DET are thought to occur concurrently, although as to which is dominant in the natural MR-1 habitat or in a MES is debatable. It is widely accepted that flavins, specifically flavin mononucleotide (FMN) and riboflavin (RF) have a role in MET [43, 44]. But there is controversy as to the importance of MET and flavins in MR-1 EET. Some reports [13, 43, 45, 46] argue that flavins serve as primary electron acceptors for the MtrC/OmcA reduced haems and play an important role in MR-1 respiration, whilst others consider them to be just one of many terminal side routes linked to the Mtr pathway with DET as the dominant mode of EET. The main mechanism in which flavins enhance the Mtr pathway is also frequently under debate [44].

Prior to the discovery that MR-1 secretes flavins, Lies *et al* [47] demonstrated that MR-1 was capable of transferring electrons to insoluble acceptors >50 µm from its outer membrane surface. In their experiments MR-1 was able to reduce Fe(III) oxides precipitated within nano-porous glass beads, suggesting MR-1 is secreting either small redox active molecules acting as electron shuttles or chelators capable of returning Fe ions back to the cell. Experiments by Bond *et al* [43] corroborated the use of redox active electron shuttles by MR-1. Once MR-1 had been grown for ~72 hours in an electrochemical cell and a steady state current reached, the 'old' culturing media in the electrochemical cell was exchanged (without disturbing the biofilm) for fresh media. The change to fresh media caused a sharp decrease in current of around 70 %, which gradually recovers over the next 72 hours back to pre-exchange levels. The supernatant from samples of MR-1 grown in electrochemical cells was analysed by LC-MS, to find significant levels of flavins (in the 100 nM range). Further experiments by Bond *et al* led to the conclusion that MR-1 and other *shewanella* strains were capable of excreting riboflavin and FMN. Using electrochemistry Bond *et al* calculated that EET mediated by flavins accounted for >70% of the total current MR-1 was producing after 72-96 hours of growth.

In support of a prominent role for flavin MET, Alessandro *et al* [14] reported a dependency of the maximum current density on the baseline corrected oxidation peak height, from non-turnover CVs (1 mV/s) assigned to flavin MET, but did not find any such dependency on the oxidation peak assigned to DET. This dependency indicates the concentration of mediator and not the number of DET sites is acting as the limiting factor for current generation by MR-1. Alessandro *et al* also calculated the relative contributions of DET and MET to the total biolectrocatalytic activity of MR-1. Under their experimental conditions they estimated MET accounted for ~52%±27 while DET accounted for 47%±16 of current generated.

MET with flavin as a soluble redox shuttle is thought to occur via a two electron/proton reaction [43]. Okamoto *et al* [44] argues, that due to the redox potentials of FMN/$FMNH_2$ and OmcA-MtrCAB, this process would result in a strong endergonic ET reaction which conflicts with the observations that flavins accelerate EET via the Mtr pathway. As a result of a study by Okamoto *et al* into the mechanism by which flavins enhance EET, an alternative model for flavin enhanced EET was proposed. From the half width potentials of differential pulse voltammetry (DVP) signals, Okamoto *et al* calculated that, to the contrary of two electron reactions with FMN/RF, one electron Ox/Sq redox reactions were more probable. Also the redox potentials of FMN in the biofilm were shifted 115 mV more positive than that for free FMN indicating that the FMN redox properties were altered by interactions with the cells. In support of a one electron mechanism, kinetic estimations of EET with a continuous influx of electrons generated by metabolism, suggest the one electron reaction of $\text{flavin}_{(\text{quinone})}$/ $\text{flavin}_{(\text{semiquinone})}$ could serve as a more efficient ET process when compared with the two-electron reaction of $\text{flavin}_{(\text{quinone})}$/ $\text{flavin}_{(\text{hydroquinone})}$.

Contrary to the above mentioned reports, Roy *et al* [48, 49] concluded, that the majority of EET from MR-1 grown on either gold or carbon cloth electrodes poised at -0.3 V vs Ag/AgCl (i.e. -0.1 V vs SHE) occurred via DET through the MtrC/OmcA protein complex with a relatively small contribution to current generation by MET/flavins. One explanation for the discrepancies in results between the different reports is that MR-1 can adapt its metabolism/EET to a diverse set of environments and the various reports differ greatly in their experimental conditions. Chao Wu *et al* [50] demonstrated that the amount of and type of flavin secreted and therefore their importance in EET varies greatly depending on the type of electron acceptor available. It has also been suggested that secreted flavins by MR-1 have an additional role in mediated energy taxis, directing the bacteria to insoluble electron acceptors (including electrodes) and helping with the formation of conductive biofilms at the electrode surface [48].

The debate regarding MR-1 EET has not been settled, with logical arguments and experimental evidence for both MET and DET as the predominant EET pathway. One potential reason for the conflicting results between reports is the diversity in experimental conditions used for whole cell electrochemistry. A relatively simple whole cell electrochemical experiment involves a myriad of variables, including temperature, pre-growth conditions (i.e. prior to transferring to the electrochemical cell), media/electrolyte (electron acceptors, possible mediators, carbon sources and other nutrients) for growth/measurements, electrode material and surface characteristics (roughness, pores, functionalisation), dissolved oxygen concentration and agitation from stirring, purging or media exchanges. The are no standard conditions and little is known about the effects these variables have on MR-1 EET behaviour, which makes comparisons of results from separate reports challenging at best.

MR-1 and other *Shewanella* species secrete endogenous flavins (FMN and riboflavin) into their environment at significant concentrations (~200 nM) but their role as simple electron shuttles is controversial. The addition of exogenous riboflavin or FMN certainly enhances MR-1 EET towards electrodes through redox cycling between outer membrane cytochromes and the electrode in an electrochemical cell, but this does not automatically mean that their main function is a mediator for MET. Synthesis and excretion of flavins requires a certain amount of resources and energy that must be offset by some sort of advantage. One obvious advantage is increased respiration. However, to keep an adequate local concentration of flavins in their natural marine like environment may prove too costly if the flavin is continually lost through diffusion and convection, unlike an enclosed small volume electrochemical cell which allows the concentration to build up without significant loss. Alternatively, if their main role is as a co-factor for enhancing DET through MtrC/OmcA, there would be no requirement for a high local concentration. The other potential role suggested for flavins is as a soluble redox sensor for finding insoluble electron acceptors in a mediated energy taxis type method.

Herein, effects on MR-1 EET behaviour, arising from the use of differing experimental conditions, are examined with particular reference to electrode surface properties (**chapter 3**). The role of flavins relating to EET is examined in **chapter 3** whilst its potential role as an agent for helping MR-1 to locate insoluble electron acceptors is assessed in **chapter 4**.

2. Theory and Background

2.1 Chemotaxis

2.1.1 Background

The ability to move in response to external stimuli can give bacteria an enormous advantage over their sedentary counterparts. The most common mechanism utilised by bacteria (>80% of discovered bacteria) for traversing through liquids is to propel themselves using motorised tail like appendages, known as flagella [51]. Bacterial flagella can rotate at rates of 300 and 1300 Hz, using H^+ or Na^+ gradient powered stators [52], generating enough propulsion to carry them at 30 or 100 µm/s respectively. Thus allowing these bacteria to traverse aqueous environments and in some cases swarm over solid surfaces [53, 54]. Bacterial species without the traditional propeller like flagella are not necessarily non-motile. There are many other forms of prokaryote motility that do not require flagella. For example, *Spiroplasma* spp use their contractile cytoskeletons as linear motors for swimming [55], numerous bacterial species use type IV pili to 'Twitch' across surfaces [56]. Some bacterial species 'glide' across surfaces using dissimilar mechanisms. For example, *Flavobacterium* spp move adhesive molecules across their surface in a tank track like manner, whilst cyanobacteria are thought to secrete a polysaccharide 'slime' out one end to push the cell in the opposite direction [57, 58].

Survival in constantly changing, sediment environments, where most nutrients and electron acceptors are concentrated into small pockets that can be few and far between, necessitates capabilities to locate and move towards those rich pockets. MR-1 gets its aqueous motility from a single polar flagella predominantly driven using a Na+ gradient powered stator and to a lesser extent a H+ gradient powered stator, enabling MR-1 to maintain motility in low Na+ environments [59]. It is not uncommon for bacteria to use both H+ and Na+ stators but usually they are used for different types of flagella. For example, *Vibrio parahaemolyticus* and *Vibrio alginolyticus* use a Na+ stator system for their unipolar flagella and a H+ stator for their lateral flagella [60].

On its own, the ability to move is not particularly useful and, considering the considerable energy expenditure required for bacterial motility, purely random movement would be detrimental in the majority of cases. To justify movement there must be an overall gain in energy involved to repay the energy debt incurred from active movement. This is achieved in prokaryotes, predominantly by chemotaxis and energy taxis mechanisms, allowing the bacterium to move in the general direction towards or away from gradients of favourable (e.g. carbon sources and electron acceptors) or unfavourable (e.g. H_2O_2) compounds respectively (**figure 2.1.1**).

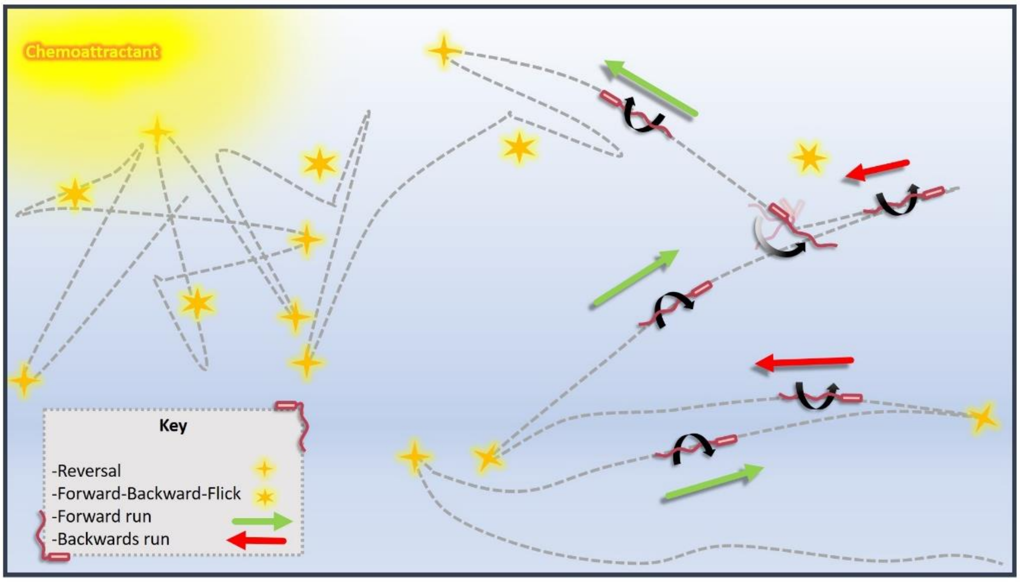

Figure 2.1.1 Cartoon of the unipolar mono flagellated 'drunken walk' towards a chemoattractant via chemotaxis or energy taxis. The grey dotted line represents a possible path a unipolar bacterium could take towards a chemoattractant source. Yellow stars indicate direction changes with 4-point stars representing reversals and 6-point stars representing forward backward flicks. The bacterium changes direction at semi random intervals. The probability for a direction change is lowered when traveling up an attractant gradient and increased when travelling down the attractant gradient. The steeper the gradient, the greater the skew towards a high or low frequency of direction changes.

2.1.2 Flagella based Chemotaxis mechanism

The general mechanisms for both chemotaxis and energy taxis in bacteria are similar and are thought to share parts of the same pathway. This is at least true for *E.coli*, where chemotaxis and energy taxis has been best studied. Considering how conserved some chemotaxis related genes are in the prokaryote kingdom, it would be reasonable to assume the sharing of pathways for chemotaxis and energy taxis is a common approach [61]. The divergence between the two mechanisms is at the sensing end of the pathways. Energy taxis employs a generic sensor for a metabolic indicator, for example the ΔpH or $\Delta\psi$ component of the proton motive force (pmf). Whereas chemotaxis uses sensors for specific molecules [62, 63]. One advantage of energy taxis, compared to chemotaxis, is that it does not suffer from the potential problem in which structurally similar molecules to the target chemoattractant could trigger unnecessary responses. Additionally, energy taxis does not require specific sensors for every molecule of interest unlike chemotaxis where each chemoattractant will usually require its own complementary sensor.

Although receptors for chemotaxis, the methyl accepting chemotaxis proteins (MCP) and those receptors used for energy taxis, differ considerably at the sensing end, they are functionally and structurally similar at the signal transduction end [64]. One of the most extensively studied energy taxis sensors is the methyl accepting chemotaxis like protein (MClP) Aer. Aer senses changes in the bacteria's redox state through its FAD associated PAS domain within the cytoplasm, while MCPs used for chemotaxis generally have their receptors in the periplasm and sense specific ligands (for example a particular amino acid or electron acceptor) [61]. Perhaps the most striking difference between MCPs used in chemotaxis and the Aer receptor is the lack of a signalling domain with methylation sites in Aer. Methylation and demethylation of MCP methylation sites serves as a regulatory mechanism for bacterial chemotaxis, the details of which are described later. Irrespective of the sensing method, both Aer and MCP's relay their signal through to the same response regulators.

MCPs and MClPs function as homodimers and are thought to be concentrated at the poles of bacteria in trimers of dimers (**figure 2.1.2**). Evidence from crosslinking studies suggest the trimers of dimers can include more than one type of MCP in which the different MCP/MClP work synergistically by augmenting each other's functions. For example if the aerotactic energy taxis Aer receptor is expressed in *E.coli* without other MCPs, the amount of expression required to produce a similar aerotactic response to *E.coli* expressing all of its MCPs was > 10 fold [65]. This explains why some MCPs lacking motifs/domains, thought to be crucial for MCP functioning, are still able to function. If one type of MCP lacks a certain motif/domain but is packed into a trimer of dimers, with MCPs that do possess the required motif/domain, then the MCP missing such motif/domain can still access the functionality of the motif/domain. For example *E.coli's* Trg and Tap MCPs lack the NWETF pentapeptide motif required for recruitment of the methyltransferase CheR, yet methylation at the methylation sites on Trg and Tap still occurs. Evidence suggests that, due to close packing, CheR recruited by MCPs with the NEWTF motif (Tsr and Tar in *E.coli*) are in close enough proximity to the NEWTF absent MCPs, to enable inter dimer methylation [52, 65]. Reversible methylation, by MCP specific methyltransferase (CheR) and methylesterase (CheB) of specific residues on MCPs, is critical to their proper functioning within the chemotaxis pathway. Methylation is used to moderate the signal output of MCPs allowing adaption to different ambient concentrations of chemoattractant/repellent. Thus insuring that only changes in ligand concentration affect signalling rather than just the presence of ligand [65].

After agonisation of the receptor end of MCP/MClPs a signal is translocated from the sensing end to the highly conserved signalling domain, via alterations in the interaction of the MCP/ MClP dimer helix bundles [64]. Apart from a relatively uncommon group of MCP's (MCP IVa and IVb), all MCP's /MClP's contain one or more Histidine kinase, adenylyl cyclase, methyl-accepting protein and phosphatase (HAMP) domains. The role of HAMP domains is to transmit signals, generated by the sensor domains, to the signalling domain [66]. One can think of HAMPs as biological 'USB' cables, capable of converting a broad spectrum of signals into downstream conformational changes in the signalling domain through helix coiled coil interactions [67].

Conformational changes in the signalling domain can switch the domains effect between activating/enhancing 'on' and inhibitory 'off'. Signals from the sensory domain, as a result of the bacteria moving in a non-favourable direction (e.g. up a repellent concentration gradient), switch the signalling domain into a state of activation whilst signals due to travel in a favourable direction are inhibitory. Here the activated/'on' state has the effect of increasing the rate of cheA trans-autophosphorylation whilst the inhibitory/'off' state supresses cheA trans-autophosphorylation activity. It should be noted that in some bacteria, for example *Bacillus subtilis* [68], the signals have the opposite effects whilst maintaining the same ultimate outcome in terms of increasing or decreasing the probability of a direction change. For example, the end response by both *E. coli* and *B. subtilis* to increasing concentrations of repellent is to increas the probability of direction changes and vice versa for attractants, the details of which are described further down.

Chemotaxis protein CheA represents the link between MCPs and their response regulator protein CheY as depicted in **figure 2.1.2**. CheA homodimers bind to the signalling subdomain of three MCP dimers arranged as a trimer of dimers, along with two receptor coupling protein CheW monomers, to form stable oligomeric complexes [52, 66]. CheA is a histidine kinase with a basal level of trans-autophosphorylation in the presence of ATP and Mg^{2+}. On association with MCPs and coupling protein CheW the trans-autophosphorylation level is enhanced. The MCP signalling domain, along with CheW, regulate CheA trans-auto-phosphorylation by adjusting the access to a phosphorylation site on one CheA monomer to the kinase site of the other CheA monomer. If the MCP is in an activating state 'on', then the rate of CheA trans-auto-phosphorylation is increased and vice versa for when the MCP is in an inhibitory state.

Phosphorylated CheA, in turn phosphorylates the response regulator CheY to CheY-P. CheY-P is able to bind to FliM in the switch complex of the flagella motor to bring about a change in rotation direction from counter clockwise to clockwise [52]. For multi flagellated bacteria, such as *E.coli*, clockwise rotation leads to the unbundling of flagella causing the bacteria to transition from a 'run' state (swimming forwards) into a 'tumble' state. Once the signal is terminated through de-phosphorylation of CheY-P the flagella resumes anti-clockwise rotation and the reoriented bacterium reengages forward swimming in a new direction. This type of motility is known as 'run and tumble' and is common to many species of bacteria. The situation is slightly different for uni-polar, mono flagellated bacteria such as MR-1, which are unable to tumble. The chemotaxis/energy-taxis signalling pathway is thought to be very similar in MR-1 as described for *E.coli*. The end result of the chemotaxis signalling cascade is also the same for MR-1 as *E.coli*. In both bacteria the CheY-P mediated signal results in a reversal of flagella rotation from counter clockwise to clockwise and a subsequent change in swimming direction. On switching from counter clockwise to clockwise rotation, instead of tumbling, MR-1 swim direction reverses in a similar way to *V.cholera* and other mono flagellated unipolar bacteria [69]. In addition to both being unipolar flagellates, MR-1 and *V.cholera* share a substantial amount of homology in chemotaxis related genes, both of which appear to have many more than *E.coli* indicating more complex chemotaxis/energy taxis pathways with possible redundancies [70].

The chemotaxis protein CheZ functions as an allosteric activator of CheY de-phosphorylation in gram negative γ-proteobacteria and regulates the duration of flagella clockwise rotation. In *E.coli* the CheZ enhanced CheY de-phosphorylation dramatically reduces the half-life of CheY-P from 20 s to 200 ms, thus shortening the chemotactic signal duration to a time scale compatible with temporal sensing [52] (**figure 2.1.2**). Deletion of CheZ in *E.coli* leads to a non-chemotactic tumbling phenotype due to increased levels of phosphorylated CheY. CheZ is also essential for chemotaxis in many other γ-proteobacteria, including *Pseudomonas aeruginosa* and *S. enterica serovar* Typhimurium [71]. MR-1 contains a homologue of CheZ which one would presume has the same role in MR-1 as in many other γ-proteobacteria, and should therefore be required for MR-1 chemotaxis and energy taxis [70]. However, one should be careful in making such assumptions. The same assumption was previously made about the only CheZ homologue found in *V.cholera* yet CheZ deletion did not appear to detrimentally effect chemotaxis [71]. This is particularly relevant to MR-1 because *V.cholera* shares substantial homology in regards to chemotaxis related genes with MR-1 and is the only organism known to share extensive regions of similar gene order, in addition to them both having unipolar systems, unlike the peritrichous *E.coli* (where CheZ is essential for chemotaxis) [69]. Therefore, without assessing MR-1 CheZ deletion mutants for chemotaxis, it would be naïve to speculate on the importance of CheZ for MR-1 chemotaxis.

CheZ enhanced dephosphorylation of CheY is not the only method used by bacteria to end the clockwise rotation of flagella. For example, the non-γ-proteobacterium Sinorhizobium meliloti, which does not have any CheZ homologues, instead expresses multiple homologues of CheY which act as phosphate sinks. Multiple homologues of CheY are frequently found in bacteria, even in those with CheZ. Thus, the CheY phosphate sink is thought to be a common mechanism in bacteria for terminating the signal for clockwise rotation. In this instance not all the CheY homologues are functional and do not bind to the flagella motor to bring about the switch in rotation from counter-clockwise to clockwise but do still accept phosphates. CheA is capable of transferring the phosphate groups from functional CheY proteins to the defunct CheY homologues, thus accelerating the rate of functional CheY-P dephosphorylation [72].

After each activation of the MCP's, resulting in a signalling cascade, adaption of their basal state to the new concentration of attractant/repellent is required for responding to further changes in attractant/repellent concentration. Without rapid adaption the bacterium would not achieve temporal sensing and thus, only sense the presence of an attractant/repellent above a threshold instead of actual gradients. Adaption of the bacterial chemotaxis pathway is achieved through methylation and de-methylation of conserved glutamate residues on MCPs, by CheR (methyltransferase) and CheB (methylesterase) respectively, as indicated in **figure 2.1.2**. The level of MCP methylation regulates both the receptor affinity to ligand and the capability of MCPs to augment CheA activity. Methylation of MCPs, by constitutively active CheR, increases the sensitivity of the system by increasing MCP enhancement of CheA activity through MCP-CheW-CheA oligomeric interactions, whilst de-methylation and concomitant methanol release by activated CheB results in an inhibitory effect on CheA activity through the MCP-CheW-CheA complex [73].

On an increase in binding of attractant to MCP receptor arrays and resulting decrease in CheA trans-autophosphorylation, the rate of CheY phosphorylation by CheA is lowered, thus levels of CheY-P decline along with the probability of flagella motor switching from counter-clockwise to clockwise. The ratio of constitutively active CheR to active CheB, increases thanks to a decrease in CheB phosphorylation by CheA. The equilibrium of MCP methylation and demethylation shifts in favour of methylation and in turn returns the sensitivity of the MCPs and CheA activity back to basal levels. On repellent binding or a decrease in attractant binding, CheA activity is increased, thus increasing the proportion of phosphorylated CheY leading to an increased likelihood of flagella reversal. In parallel, but at a slower rate, the increased CheA activity increases the proportion of phosphorylated CheB to CheR (**figure 2.1.2**). Thus, increasing MCP demethylation to cause an inhibitory effect on CheA autophosphorylation. The result is a re-adjustment of the system to new levels of attractants/repellents returning CheA activity to pre-stimulus levels. The rate of CheY phosphorylation by CheA is significantly higher than the rate of CheB phosphorylation, allowing for a CheY-P mediated chemotaxis response to take place prior to methylation/de-methylation adaption. The rate of methylation is also substantially slower then phosphorylation, which similarly helps to ensure the phosphorylation mediated chemotaxis response takes place prior to adaption [73] [52].

The above description of a bacterial chemotaxis mechanism is largely based on the model bacterium *E.coli* where all the steps are known. The overall chemotaxis pathway is considered to be relatively conserved across the prokaryotes and consequently the chemotaxis description above can be taken as a general approach used by bacteria. However, there is a lot of diversity in the implementation details between bacterial species and, as more bacterial species are studied, the *E.coli* model is beginning to look more like a simplified version compared to many other species which have far more putative chemotaxis genes. For example in *Bacillus subtilis,* although the end results of the chemotaxis signalling cascade is the same as for *E.coli*, certain key chemotaxis proteins work in reverse compared to their *E.coli* counterparts. On attractant binding to *Bacillus subtilis* MCPs, the phosphorylation rate of CheA increases, (in *E.coli* the rate is decreased), thus levels of CheY-P increase. But, unlike *E.coli*, binding of CheY-P to the flagella motor in *Bacillus subtilis* decreases the probability of a direction change, thus both species display the same flagella response to attractants and repellents. The effects of MCP methylation/de-methylation for *Bacillus subtilis,* in nutrient rich environments, are more subtle then with *E.coli*. Depending on the specific residues, methylation of MCPs can either increase or decrease CheA phosphorylation. *Bacillus subtilis* also expresses the CheW-CheY fusion protein CheV under certain conditions. Although CheV is not present in *E.coli*, it is found throughout the proteobacteria (including γ, β, and δ), sometimes alongside CheW but can also be present without. This suggests that in some species CheV carries out a similar role to

CheW. CheV is also implicated in chemotaxis regulation and adaption in species expressing both CheW and CheV [68, 74, 75]. As illustrated, mechanistic details within the chemotaxes pathway of different species can differ substantially. Yet there are also incredibly conserved regions. For example, a CheW homologue from the α-proteobacterium *R. sphaeroides* can be used to restore flagellar rotation switching in a γ-proteobacteria ΔCheW *E.coli* mutant [76].

MR-1 possess homologues, multiple in some cases, of all the key proteins identified in the *E.coli* chemotaxis pathway, although MR-1's chemotaxis pathway seems to incorporate a higher degree of redundancy when compared to *E.coli*. Investigations into the putative chemotaxis genes of MR-1 only found one gene that was essential for MR-1 chemotaxis. The essential chemotaxis gene encodes for CheA-3 (a CheA homologue). In frame deletion of the gene encoding CheA-3 results in mutants with a smooth swimming phenotype unable to change direction [70]. In addition, only one chemoreceptor (SO2240) has been identified as playing a significant role in electron acceptor chemotaxis in MR-1 along with 4 other receptors which have an effect when deleted alongside SO2240 [77]. In the case of electron acceptor chemotaxis, the Mtr pathway has been found to be more important than that of chemoreceptors.

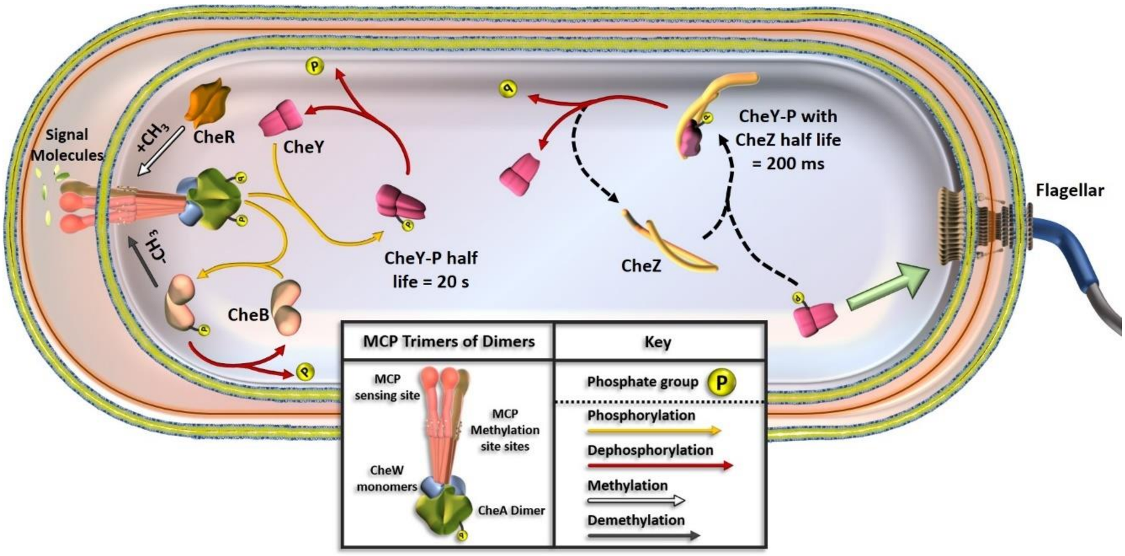

Figure 2.1.2 Overview of a possible chemotactic pathway for MR-1 based on chemotaxis related proteins found in MR-1 and which share substantial homology with proteins implicated in the *E. coli* chemotaxis model pathway. Yellow arrows indicate interactions resulting in phosphorylation whilst red arrows indicate Dephosphorylation. Methylation and demethylation of methylation sites on MCPs, by CheR and CheB, is indicated by white and black arrows respectively. The dashed black arrows represent interactions between CheZ and CheY-P which causes an increase in CheY-P de-phosphorylation and therefore decreases the length of time FliM from the flagellar motor complex is exposed to CheY-P. Here CheZ is acting as an allosteric activator of CheY de-phosphorylation.

2.1.3 Background on common Techniques used to study Chemotaxis

The chemical in capillary method, aka ‘quantitative Pfeffer method’ developed by Adler *et al* [78], was one of the first quantitative assays for measuring positive chemotaxis of bacteria towards attractants. In this instance a capillary, closed off at one end and containing a small volume of potential chemotactic chemical of known concentration, is placed open end first into a small reservoir containing a bacterial suspension. If desired the entrance of the capillary can be monitored microscopically. After a set duration the capillary is withdrawn from the reservoir, the sealed end broken off and contents flushed through into growth medium. Dilutions from the media, inoculated with the capillary contents, are plated followed by an incubation period so that colony forming units can be quantified. If the chemical in the capillary is a chemoattractant, one would expect to find a higher fraction of the cfu’s inside with respect to the reservoir and compared to a control capillary containing an inert solution. If the chemical of interest is a chemorepellent one would expect a reduction in cfu’s compared to the control capillary. The downside to the capillary technique is that it is relatively laborious and, although it has good sensitivity toward chemoattractants, it has relatively poor sensitivity to chemo repellents requiring a high concentration before any effect can be quantified.

In response to the poor sensitivity of the chemical in capillary and variants, (e.g. chemical in pond capillary method), Adler *et al* [79] developed a series of alternative assays more suited for negative chemotaxis and tested them with a range of chemicals. The chemical in plug aka ‘plug in pond’ assay proved to be the most sensitive out of the methods tested. An added benefit of the chemical in plug method is its simplicity. Its set-up consisting of a hard agar (~2% agar) plug equilibrated with a known concentration of the chemical of interest surrounded by soft agar (~0.3% agar) containing an even dispersion of bacteria at a high enough concentration of cells to give visible turbidity. If the hard agar plug contains a chemorepellent the bacteria in the surrounding soft agar, in which the repellent diffuses into, will ‘swarm’ away from the repellent, leaving a clear/less turbid area around the plug and a ring around the clearing containing a higher density of cells. The size/radius of the cleared area will be proportional to the concentration of the repellent in the plug. If, on the other hand, the plug contains an attractant then bacteria in the soft agar around the plug in which the attractant diffuses into and forms an attractant gradient, will migrate towards the plug, creating an area of high turbidity around the plug and a corresponding area of low turbidity from where the cells travelled from.

The chemical in well assay is a slight variation of the chemical in plug assay and has been used alternatively to the chemical in plug assay especially if quantitative results are desired [77, 80-82]. Instead of a hard agar plug containing the chemical of interest a well is formed in the bed of soft agar and filled with a solution containing the chemical of interest. At the end of the incubation period, as with the chemical in plug assay, qualitative observations of accumulation or clearing are made. If a quantitative result is required the solution in the well can be diluted and plated out for the quantification of colony forming units (cfu’s). For assessing many potential tactic agents quickly, a high throughput version of the chemical in well assay has also been developed called the chemical-in-µwell assay [80] which has been used to identify previously unknown chemotactic agents for MR-1, including L-malic acid and bromo succinic acid.

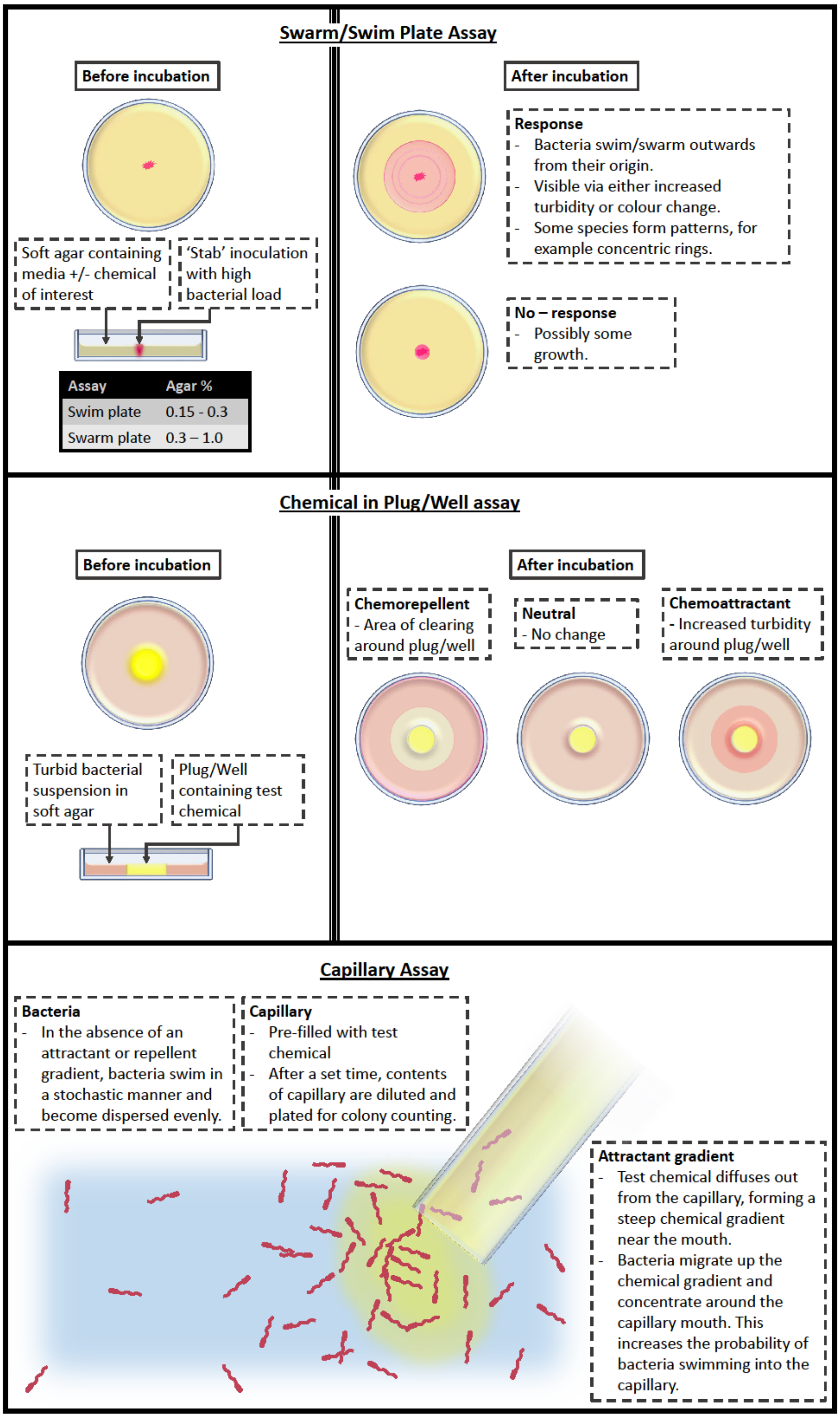

Assay	Agar %
Swim plate	0.15 - 0.3
Swarm plate	0.3 – 1.0

Figure 2.1.3. Illustrations of the three predominant techniques used for bacterial taxis studies. **Top**) swarm/swim plate assay; depending on the concentration of agar used. **Middle**) the qualitative version of the chemical in well assay and the almost identical chemical in plug assay. **Bottom**) the capillary assay.

The swim and swarm plate assays are another agar plate based method frequently used to study energy taxis and chemotaxis in bacteria, including in MR-1 [83, 84]. The set-up for swim and swarm plates is almost identical. Briefly, a small volume (<10 µl) of highly concentrated bacteria suspension is 'stabbed' into the centre of a soft agar, (<0.3% for swim plates or between 0.3 to 1% for swarm plates), plate containing a known concentration of the chemical of interest. The premise is that the bacteria introduced into the soft agar will metabolise the chemical of interest in its vicinity resulting in a concentration gradient which the bacteria can travel up by chemotaxis if the chemical is a chemo-attractant or by energy taxis. Depending on the specifics of individual experiments usually the swarming/swimming of the bacteria outward from their origin can be monitored as increases in turbidity, (sometimes seen as concentric circles). In other experiments, where the might not be a noticeable difference in turbidity, if the chemical of interest undergoes a colour change, (e.g. yellow to clear in the case of reduction of riboflavin by MR-1), then this can be used to indirectly monitor the bacteria swarm boundary.

In addition to the traditional capillary assay and agar plate techniques for studying bacterial chemotaxis a range of in house experimental set-ups and commercially available microfluidic based chemotactic chambers have been adopted. For example, Nealson *et al* [82] developed an in house spectrophotometric set up and used it to assess MR-1 tactic responses to a range of electron acceptors and carbon sources. The main body of the set-up is a plastic tube with a top end and a bottom end. The top end can be sealed off with a cap holding an agar plug (containing the chemical to be tested). Just beneath the top end is a small entrance in the wall of the tube for insertion of the dipping probe colorimeter which measures the optical density of suspension close to the agar plug. The bottom end is sealed off using a cap fitted with an O-ring. Once the tube has been filled with a bacterial suspension of defined OD_{600nm} and tube entrances sealed up, with agar plug and dipping probe in place, the OD_{600nm} of the suspension at the plug end can be monitored in real time. If the plug had been applied with attractant, one would expect the OD_{600nm} at the plug end to increase as the bacteria swim up the attractant gradient created from attractant diffusing out of the plug and into the suspension. Compared to most plate based assays, where frequently only a single end point measurement is taken, the set up by Nealson *et al* is suited for the collection of real time measurements throughout the whole experiment whilst keeping the technique simple and accessible [82].

Commercially available chemotaxis chambers are used quantitatively, either as a primary technique or as a secondary technique to validate results obtained from traditional or experimental techniques [77, 80]. The general layout for a basic chemotaxis slide mounted chamber has 2 reservoirs connected by a thin channel. Once both reservoirs have been filled with media, (excluding the chemical of interest), a gradient of the chemical of interest can be created in the connecting channel by adding a small volume of the chemical to one of the reservoirs before adding the bacterial sample into the opposite reservoir. The connecting channel can then be monitored for the transmigration of bacteria towards the chemical of interest, (in the case of chemoattractant), and compared against controls with no chemoattractant or repellent added.

Although the range of tools for monitoring bacterial taxis has grown and diversified since Alder's capillary and agar plate techniques, both agar plate techniques and capillary assays are still wildly used for taxis studies. Regarding MR-1 taxis studies they have been the predominant technique used [77, 80, 81, 83, 84]. The continual use of agar plate techniques is a testament to their simplicity and accessibility. As mentioned, the agar plate techniques also give quick results and have sensitivities to both attractants and repellents [79]. As with all techniques, the agar plate methods also have drawbacks. Over the last decade there have been numerous reports of discrepancies between agar plate based techniques and other techniques [77, 81, 85, 86], most notably the quantitative capillary assay developed by Alder *et al* [78] and described above. These discrepancies led Li *et al* [86] to assess the validity of the chemical in plug assay using non-chemotactic mutants of MR-1 and H. pylori and found the assay to give false positives for both species under certain conditions [86]. The unreliable nature of some agar plate techniques has encouraged researches to utilise secondary techniques, alongside agar plate techniques, such as the capillary assay [81], microfluidics chemotaxis chamber [77] or in house custom made devices [85], [81]. In addition to the mentioned issues with agar plate techniques, the extensively used capillary assay developed by Alder *et al* [78] was reported to give unreliable results. For example, Li *et al* [85] had to discard results obtained by the capillary assay, for calculating chemotaxis constants required by their model, because of dubious values given by the assay.

The techniques detailed in this section give a background on the principal techniques used in bacterial taxis studies, with a focus on MR-1. Most reports regarding MR-1 taxis, including towards electron acceptors and electrodes have been carried out using these techniques described here. The one technique not covered in this section is video microscopy, which is covered in **chapter 4**, where it was used in conjunction with electrochemistry for investigating the role of flavins in MR-1 taxis towards electrodes.

2.2 Electrochemistry

2.2.1 Background

Electrochemistry began in the 1700's with a desire to understand electrical phenomena. This led to a series of experiments employing large friction machines for generating electric 'sparks' which were passed through gasses and liquids to induce chemical reactions. Although many interesting phenomena were observed during these experiments, (for example the generation of ozone), scientific understanding of the processes causing these phenomena did not progress significantly until the turn of the century. The great Svante Arrhenius attributes the accelerated advancements in electrochemistry made during the 1800's, in part to Galvani and his infamous experimentation with frog legs. [87] In 1780 Galvani *et al* applied a spark to the exposed nerve from a pair of severed frog legs. Galvani noticed that the spark was immediately followed by a subsequent kicking of the legs, as if the frog were alive. From these observations, and a series of similar experiments, Galvani extrapolated the theory of "Animal electricity", which was largely accepted by the scientific community at the time but not by a young Volta who had his own theory as to how the electrodes caused the leg to kick. Disagreement between Volta and Galvani led to a long-standing rivalry, which has been attributed to the invention of the voltaic pile by Volta, (i.e. the invention of the first battery), and also to advances made by Galvani which laid the foundations for electrophysiology [88].

Electrochemistry is the study and application of phenomena that relate to the interaction between electrical and chemical effects. An electrical current can be both the cause of a chemical change or conversely the product of a chemical change. By applying a potential across an electrochemical system, one can initiate desirable chemical reactions like the splitting (electrolysis) of water into hydrogen and oxygen for energy storage. Electrochemical techniques are applied extensively in industry, for example electrolysis in aluminium production, electroplating surfaces for preventing abrasion or corrosion, and for signal transduction in bio-sensors [89]. Alternatively, and more relevant to this thesis, one can probe a system in a variety of ways by controlling the potential (voltammetry) or current across the system whilst monitoring one or more variables. For example, while keeping a fixed potential across two electrodes one can measure the subsequent current (amperometry) resulting from electrochemical reactions on the electrode surface. Because the current is directly related to the rate of a redox reaction, one can use a technique known as chronoamperometry (chronoamperometry is a type of amperometry which itself is a type of voltammetry) to obtain kinetic information on a chemical reaction of interest. Measurable variables are not just restricted to electrical parameters such as potential or current. It is common to couple electrochemical techniques to other analytical techniques such as spectrophotometry, in which case the measured variables may include absorption spectra collected whilst controlling the potential across a system of interest. Such coupling of techniques can be useful for studying reaction mechanisms [90].

Instead of monitoring current as it varies with time at a specified constant holding potential, one can scan through a range of potentials at a constant rate and measure the current as a function of potential, in a technique known as linear sweep voltammetry. By performing consecutive scans in opposite directions, with the second scan beginning where the first scan ends, one can obtain additional information about a system, for example if a certain electrochemical reaction is reversible or not. This technique is known as cyclic voltammetry and is not exclusive to just two scan procedures as any number of scans can be used. For example to determine the stability of an electrocatalyst it is not uncommon to apply hundreds of consecutive scans [91].

2.2.2 Cyclic Voltammetry Overview

Cyclic voltammetry (CV) is used widely for both qualitative and quantitative analysis of electrochemical systems [92]. Its strengths are in its simplicity, availability and rate at which results can be acquired. To interpret the resulting current-potential (**i-E**) curves from CV procedures one must first develop a basic understanding of the fundamental chemical and physical processes involved at the electrode surface. CV was used extensively throughout the projects covered by this thesis and during this chapter CV is employed as an example electrochemical technique for explaining fundamental aspects of electrochemistry. A qualitative overview of the processes taking place during a simple CV procedure is outlined below. Highlighted electrochemical processes from this description are subsequently evaluated in a more quantitative and rigorous manner including derivations of the equations used to model and explain electrochemical phenomena. For reference purposes some of the electrochemical terms used throughout this section are defined at the end of this chapter (**2.2.9 Electrochemical Definitions**).

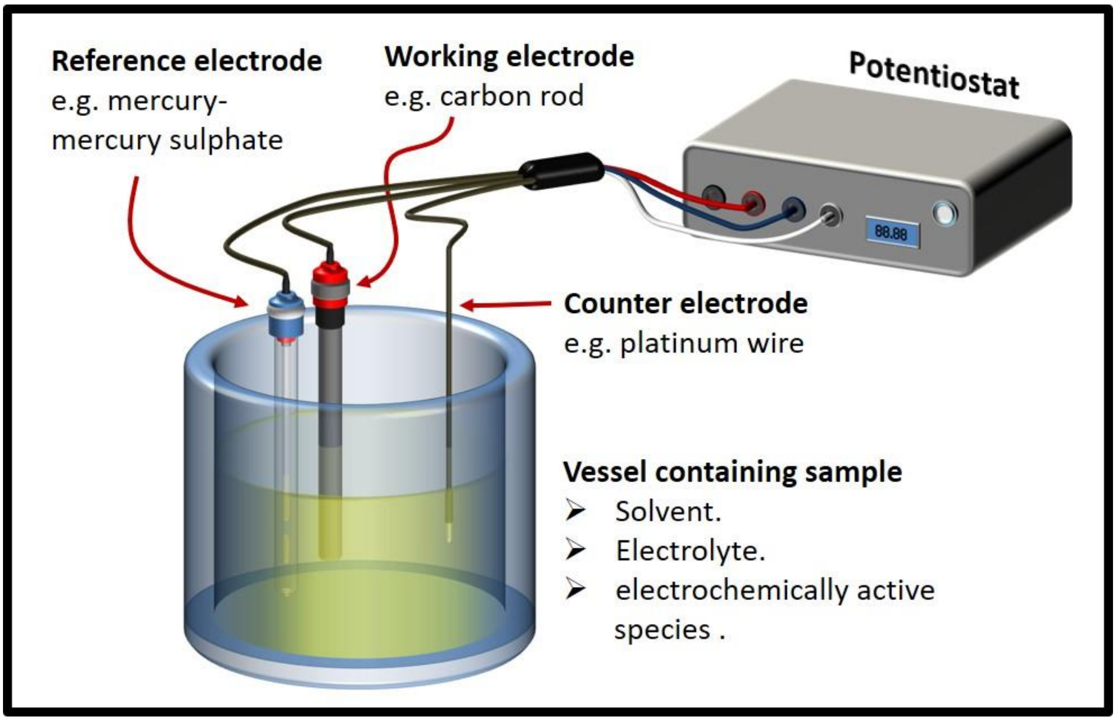

Figure 2.2.1 Cartoon of a simple three-electrode electrochemical set-up. An open beaker is acting as the electrochemical cell vessel. Alternatively, a specifically designed vessel can be used as the electrochemical cell which can allow for temperature control, stirring, purging and to have the sample sealed from the outside (e.g. to create an anaerobic environment). It is also common to place the electrochemical cell in a Faraday cage to reduce electromagnetic noise.

A standard electrochemical system (**figure 2.2.1**) consists of two or three electrodes, a solvent (e.g. water), electrolyte, (e.g. an inert salt), and one or more electrochemically active species. The hypothetical system used here for describing CV has one fully reversible ($\mathbf{S_{red} \rightleftarrows S_{ox} + e^-}$) electrochemically active species **S**, the entirety of which is in its reduced form $\mathbf{S_{red}}$, and is at a concentration far lower than the electrolyte. As mentioned above, a CV procedure consists of two or more potential scans with each subsequent scan beginning immediately after the previous scan and starting at the end potential of the previous scan. When scanning a potential in the positive direction, from $\mathbf{E_1}$ to $\mathbf{E_2}$, only background current is measured until reaching the vicinity of $\mathbf{E^0}$, (formal/midpoint potential of species **S**), at which point the current begins to rise above the background level. On moving further towards $\mathbf{E_2}$, the overpotential rises leading to an increase in the rate of $\mathbf{S_{red}}$ oxidation, and at some point, the rate is high enough to result in zero concentration of $\mathbf{S_{red}}$ at distance 0 ($\mathbf{x_0}$) from the electrode surface. At this point the rate of reaction, and therefore current, becomes limited by mass transport, which reaches a maximum rate prior to decreasing as the depletion effect starts to prevail and the diffusion layer widens. Because of an essentially ‘infinite’ reservoir of $\mathbf{S_{red}}$ in the bulk solution, there will always, (within standard experimental timescales), be a significant flux of $\mathbf{S_{red}}$ towards the interface and thus a current, albeit an exponentially decreasing one. This creates the characteristic peak seen in many CVs. On the reverse scan, initially, there is a sharp drop in oxidative current as the driving force for oxidation decreases. On approach to the formal potential (scanning towards negative potentials) almost all of species **S** at the interface is in the oxidised state $\mathbf{S_{ox}}$ (generated from the forward scan). The rate of $\mathbf{S_{ox}}$ reduction will therefore overtake the rate of $\mathbf{S_{red}}$ oxidation to produce a net negative current even while the rate constant for reduction is lower than that for oxidation. On reaching, and passing the formal potential the rate will continue to increase, prior to levelling off and decreasing as the $\mathbf{S_{ox}}$ is depleted at the interface. Unlike the forward scan, because the is no bulk concentration of $\mathbf{S_{ox}}$, the will be no continual influx. Thus, instead of an exponential decay to a point significantly above/below zero current, (determined by mass transport processes), the reverse scan will decay towards the background current.

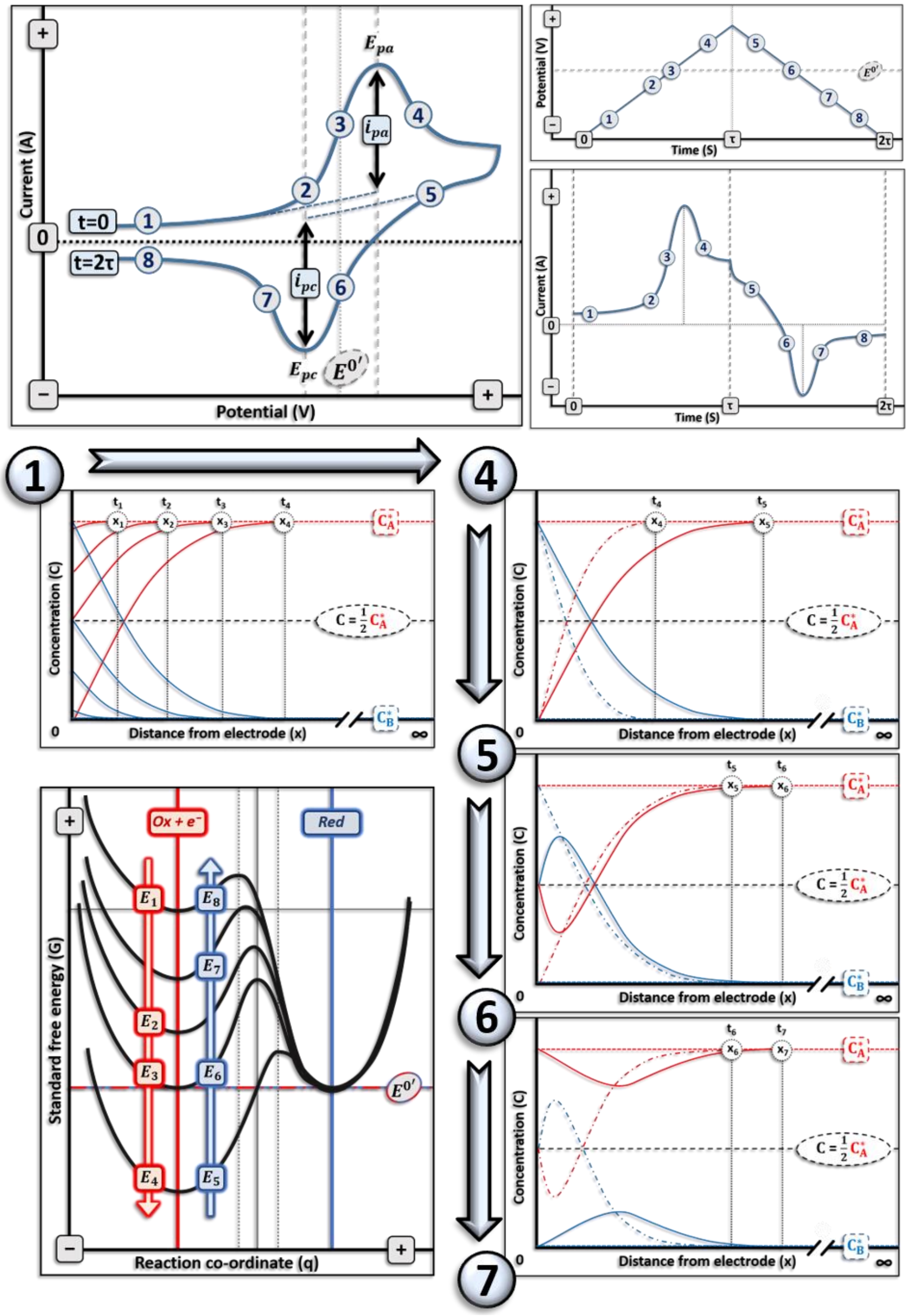

Figure 2.2.2 Idealised cyclic voltammogram (CV) for a fully reversible electrochemical species along with concentration profiles and potential energy curves. **Top left** is the standard current vs potential CV plot. **Top right** time domain plots for the applied potential and resultant current (below). **Left middle** depicts the concentration profiles of the reduced (**red**) and oxidised (**blue**) form of the redox active species during the forward/oxidising scan with reference to the numbered points on the CV (**1** to **4**). **Right middle** through to **right bottom** depicts the concentration profiles during the reverse/reducing scan (**4** to **7**). **Left bottom** depicts potential energy curves for the numbered points labelling the CV (**1** to **8**) during the forward and reverse for the reduced state and oxidised state with fermi level electron from the electrode.

2.2.3 The Charging Current

Not all the current measured in a CV procedure is from the electrochemical species of interest. Even in cases where the system contains just the electrochemically active species of interest there will be a degree of background current. Without significant concentrations of impurities, the dominant contributor to background current is the charging current. Applying a potential step from resting potential to a more negative or positive potential across two electrodes immersed in a reservoir of aqueous electrolyte, without any electrochemically active species present, will not cause any electrons to transfer between the electrode and the solution, (i.e. there is no faradaic current), yet a current will still flow. On applying the potential step ($\mathbf{E_0 \rightarrow E_1}$), the current will jump instantaneously from zero to a level determined by the applied potential and electrolyte composition. If the potential is then held indefinitely the current will decay exponentially towards zero. This ‘non-faradaic’ current described is known as the charging current and is present irrespective of faradaic processes. The charging current is the result of rearrangements in the electrical double layer at the interface between electrode and solution [93]. To set the electrode at a certain potential charge is moved into the electrode either as electrons (if $\mathbf{E_1 < E_0}$) or as holes (if $\mathbf{E_1 > E_0}$). In response, the electrical double layer at the interface, rearranges to allow more counter ions to move closer to the electrode surface, effectively shielding the charge on the electrode. To keep the potential at the set value, more charge must move into the electrode which manifests itself as the continued current observed (movement of charge = current). More counter-ions will again move towards the electrode and increase the local excess concentration further. The increasing excess concentration of counter ions and, therefore, order is countered by thermal effects (entropy) to increase disorder and homogenise the concentration of ions. The extra charge and, therefore, current required to keep a constant potential, decreases exponentially because of the increasing resistance provided by entropy to further shielding by counter ions. Eventually a steady state is reached once the energy required for further rearrangement of the double layer, (to increase the local counter ion excess concentration), reaches that of the electrostatic attraction from the charge on the electrode surface.

2.2.4 The Depletion Effect

The depletion effect is a mass transport phenomenon which gives the characteristic shape to iE-curves seen in CVs of reversible redox reactions. The depletion effect can also be observed during a simple potential step chronoamperometry procedure of a system containing electrochemically active species. Applying an oxidative over potential to a system containing one fully reversible electrochemically active species (**$S_{red} \rightleftarrows S_{ox} + e^-$**) in its reduced state **S_{red},** results in the oxidation of **S_{red}** into **S_{ox}** at the electrode surface. If the oxidation overpotential is high enough and the electron transfer rate is fast, then effectively all **S_{red}** at the electrode surface is immediately oxidised to **S_{ox}**, thus the concentration of **$[S_{red}]$** at the interface is effectively zero. Because the ET kinetics are much faster than the delivery (flux) rate of 'fresh' **S_{red} ,**(which is determined by mass transport), mass transport becomes the limiting factor for the reaction rate and therefore the measured current. Mass transport encompasses multiple phenomena and is described in more detail later. For simplicity, in this example system, the rate of mass transport is determined solely by diffusion. The rate of flux due to diffusion of a species from point **x_1** to **x_0** is therefore directly proportional to the concentration gradient of that species between **x_1** and **x_0** (i.e. Fick's first law **equation 2.2.3**). Consequently, the current is also dependent on the concentration gradient. If **S_{red}** continues to oxidise immediately upon arrival at the interface it Is inevitable that the distance between the electrode surface, where the concentration of **$[S_{red}] = 0$** and the bulk, where the concentration remains at its initial value, will increase (**figure 2.2.3**). This increasing zone between the two extreme concentrations is known as the depletion zone. One can see from **figure 2.2.3** that the wider the zone becomes with time, the lower the concentration gradient. It is this decrease in concentration gradient which is the cause of the depletion effect and, because the rate of diffusion is dependent on the concentration gradient, as described by **figure 2.2.5**, the flux along with the current will decrease with time.

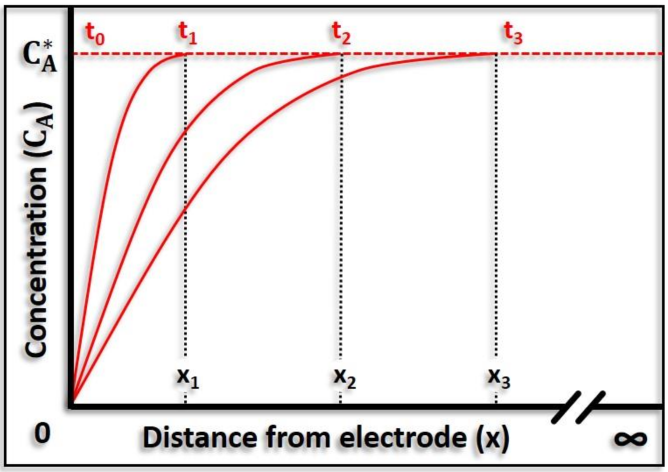

Figure 2.2.3. Concentration profiles for the oxidised state of a hypothetical reversible redox species shown at four different times. Starting system at time zero (**t_0**) with all species in the oxidised state. The next time point displayed **t_1**, represents the concentration profile after a short duration at a highly reductive potential **E_1**, relative to the species formal potential **$E^{0'}$**. At potential **E_1**, the rate constant for reduction **k_{red}**, far outweighs the rate constant for oxidation **k_{ox}**, such that the rate of oxidation is negligible, thus the concentration of the oxidised species is essentialy zero. Time points two **t_2** and three **t_3**, represent progressively longer durations at potential **E_1**. With increasing duration at **E_1**, there is a widening in the diffusion layer/ depletion zone along with a decrease in concentration gradient, resulting in a reduction in flux.

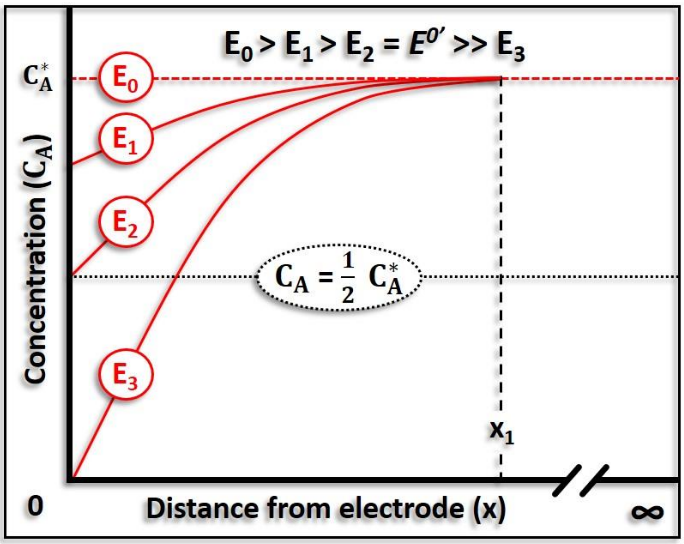

Figure 2.2.4. Concentration profiles for potentials ranging from reductive and oxidative extremes with respect to the formal potential of a hypothetical reversible redox active species in the reduced state **A**.

2.2.5 Mass Transport

Mass transfer encompasses effects due to diffusion, migration, and convection. The term migration refers to the movement of charged species in an electric field and is controlled by electrostatic effects due to charge differences, rather than concentration differences which control diffusion. Thus, neutral species are not affected by migration, whilst for charged species the extent of the effect is dependent on the rest of the system. Charge differences are generated at the electrode surface by redox reactions of the electrochemically active species moving electrons between solution and electrode. To compensate the charge difference counter ions must migrate towards the electrode. Counter ions include both electrochemically active species carrying an opposite charge and electrochemically inert ions (from the electrolyte). The ratio of a charged electrochemically active species to the electrochemically inert counter ions, which must migrate towards the electrode, is proportional to the concentration ratio of the different counter ion species. Thus, in the case where the electrochemically active species concentration is negligible relative to the electrolyte counter ion, the proportion of the total counterions migrating toward the electrode is also negligible, whilst the total number of counter ions required is dependent on the concentration of electrochemically active species involved in the redox reaction. This means, in cases with excess electrolyte, the overall effect of migration on electrochemically active species is insignificant, and almost all the mass transfer of electrochemically active species is caused by diffusion and convection. Convection refers to fluid flow caused by natural density gradients or forced flow from stirring, vibrating or bubbling. If the system is not stirred, kept still (free from vibrations), and the temperature of the whole system is maintained constant, effects from convection can be broadly ignored.

2.2.6 Fick's Laws & Diffusion

Mass transport dominates the characteristics of electrochemistry performed on conventional electrodes at high potential differences (relative to the equilibrium potential of the electrochemically active species). In many cases, the largest contributor to mass transport is diffusion.

Fick's first law of diffusion (**equations 2.2.3**) can be used to relate the flux $\boldsymbol{J_A(x,t)}$ (**mol·s^{-1}·cm^{-2}**), of species $\boldsymbol{A}$ at location $\boldsymbol{x}$ and time $\boldsymbol{t}$, with the concentration gradient, via the diffusion coefficient $\boldsymbol{D_A}$. The diffusion coefficient is a species (i.e. species size relative to solvent) and system, (i.e. temperature, pressure, viscosity etc…), dependent constant related to the average distance moved per direction change (step size), and average time between each direction change. The larger the diffusion coefficient is for a species, the more rapidly this species will diffuse. In an **n**-dimensional system the diffusion coefficient for a particle is related to the particles mean squared displacement $\langle \boldsymbol{R}^2 \rangle$ by **equation 2.2.1**, from Einstein's famous work on Brownian motion [94]. Either using Einstein's equation or from performing dimensional analysis on Fick's first law, one obtains the following units for the diffusion coefficient ($\boldsymbol{l}^2/\boldsymbol{t}$ i.e. **cm²·s⁻¹**). The diffusion coefficient $\boldsymbol{D_A}$ can also be related to temperature using the Stokes-Einstein equation [94].

Equation 2.2.1. $D_A = \frac{\langle R^2 \rangle}{2nt}$ → $D_A = \frac{\Delta x^2}{2\Delta t}$ (in relation to Fick's first law for 1D)

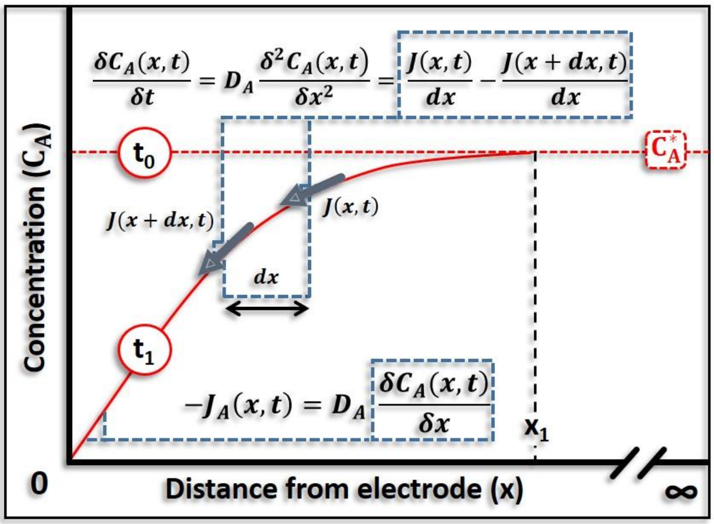

Figure 2.2.5. Depiction of how Fick's Laws relate to the concentration profile of an electrochemically active species in the oxidised state **A** close to an electrode set at a highly reductive potential **E$_1$**. At time zero (**t$_0$**), prior to the application of a reductive potential, the concentration of **A** at the interface is the same as the bulk concentration (**$C_A(t_0,x_0)$ = C_A***). The next time point displayed **t$_1$**, represents the concentration profile after a short duration at a highly reductive potential **E$_1$**, relative to the species formal potential **E$^{0'}$**. At potential **E$_1$**, the rate constant for reduction **k$_{red}$**, far outweighs the rate constant for oxidation **k$_{ox}$**, such that the rate of oxidation is negligible, thus the concentration of the oxidised species is essentialy zero at the interface.

The equation representing Fick's fist law can be derived by considering a plane of area $\mathbb{A}$, separating two sides. On the left, at position $\boldsymbol{x},$ there is $\boldsymbol{N_A(x)}$ number of $\boldsymbol{A}$ molecules, whilst on the right, at position $\boldsymbol{x + \Delta x},$ there is $\boldsymbol{N_A(x + \Delta x)}$ number of $\boldsymbol{A}$ molecules. If all molecules are continuously moving at a rate of $\boldsymbol{\Delta x/\Delta t}$, and can only move left or right, with a 50:50 probability of moving in either direction, after each $\boldsymbol{\Delta t}$ interval, the net flux through the plane of area $\mathbb{A}$ from left to right, using position $\boldsymbol{x}$ for perspective, is given by **equation 2.2.2.1**. One can then multiple both sides by $\frac{\boldsymbol{\Delta x^2}}{\boldsymbol{\Delta x^2}}$, and replace the amounts $\boldsymbol{N_A}$ with concentrations $\boldsymbol{C_A}$ by substitution with $\boldsymbol{N_A = C_A}\mathbb{A}\boldsymbol{\Delta x}$, to get **equation 2.2.2.2**. Rearrangement of **equation 2.2.2.2** results in **equation 2.2.2.3**, which can be simplified by applying the diffusion coefficient $\boldsymbol{D_A} = \frac{\boldsymbol{\Delta x^2}}{\boldsymbol{\Delta t}}$. Additionally, if $\boldsymbol{\Delta x}$ and $\boldsymbol{\Delta t}$ approach zero, then one is left with Fick's first law (**equation 2.2.3**).

Equation 2.2.2.1.

$$J_A(x,t) = \frac{1}{\mathbb{A}} \frac{\frac{N_A(x)}{2} - \frac{N_A(x+\Delta x)}{2}}{\Delta t}$$

Equation 2.2.2.2.

$$J_A(x,t) = \frac{\boldsymbol{\Delta x^2}}{\boldsymbol{\Delta x^2}\mathbb{A}} \frac{C_A(x)\mathbb{A}\Delta x - C_A(x+\Delta x)\mathbb{A}\Delta x}{2\Delta t}$$

Equation 2.2.2.3.

$$-J_A(x,t) = \frac{\Delta x^2}{2\Delta t} \frac{C_A(x+\Delta x) - C_A(x)}{\Delta x} = D_A \frac{C_A(x+\Delta x) - C_A(x)}{\Delta x}$$

Equation 2.2.3.

$$-J_A(x,t) = D_A \frac{\delta C_A(x,t)}{\delta x}$$

Fick's first law provides a method of calculating the flux of an electrochemically active species towards an electrode surface from a concentration gradient but does not describe how the concentration gradient changes over a distance between two points of known concentration or how the concentration at a location changes over time. To model the changing gradient over a distance or time one requires Fick's second law which itself can be derived from the first law. Using the same model as before but also giving a thickness $\boldsymbol{dx}$, to the plane separating left and right, one can calculate the difference between the flux entering the plane on its left side $\boldsymbol{J(x,t)}$, with the flux exiting from its right side $\boldsymbol{J(x + dx, t)}$. The change in flux over the distance $\boldsymbol{dx}$ gives the change in concentration per unit of time for between $\boldsymbol{x}$ and $\boldsymbol{x + dx}$ (**equation 2.2.4**). Application of Fick's first law (**equation 2.2.3**) to **equation 2.2.4** then results in Flicks second law (**equation 2.2.5.1**).

Equation 2.2.4.

$$\frac{\delta C_A(x,t)}{\delta t} = \frac{J(x,t) - J(x+dx,t)}{dx} = -\frac{\delta J(x,t)}{\delta x}$$

Equation 2.2.5.1.

$$\frac{\delta C_A(x,t)}{\delta t} = D_A \frac{\delta^2 C_A(x,t)}{\delta x^2}$$

The form of equation used to represent Fick's second law is dependent on the electrode geometry. Planar electrodes were mainly used in this thesis and **equation 2.2.5.1** has been derived for such electrodes where diffusion is linear. Wire electrodes were also used during the thesis for taxis studies here Fick's second law can be derived using a diffusion model based on a cylindrical surface to yield **equation 2.2.5.2**.

Equation 2.2.5.2.

$$\frac{\delta C_A(r,t)}{\delta t} = D_A \left(\frac{\delta^2 C_A(r,t)}{\delta r^2} + \frac{1}{r} \frac{\delta C_A(r,t)}{\delta r} \right)$$

In a situation where the mass transport of electroactive species **A**, occurs purely by diffusion (e.g. **A** is a neutral species, or the system contains excess electrolyte and there is no stirring), and the diffusion coefficient remains constant throughout any concentration changes (e.g. The bulk concentration of **A** is dilute), then a direct relationship between the flux and current is formed. The current is the rate of electron transfer, which is proportional to the rate of redox active species arriving to the electrode by the number **n** of electrons transferred per reaction, thus the relationship is given by **equation 2.2.6**.

Equation 2.2.6.

$$-J_A(0,t) = \frac{i}{nF\mathbb{A}} = D_A \left[\frac{\delta C_A(x,t)}{\delta x} \right]_{x=0}$$

2.2.7 Derivation of the Nernst equation

The Gibbs free energy is a measure of the thermodynamic potential of a system, and gives the maximum possible work that can be extracted from a system to its surroundings. Whether or not a system will change its state from state **A** (for example the oxidised form of a species) to state **B** (for example the reduced form of a species) spontaneously, is determine by the Gibbs free energy of **A** and **B**. If state **A** is of a higher energy level than state **B**, then the system may spontaneously move towards state **B** from **A** [95]. Systems move from higher energy states to lower energy states by discharging energy, either through releasing heat (decreasing enthalpy $\boldsymbol{H}$) or increasing the entropy $\boldsymbol{S}$ of the system. The relationship between a systems energy level (i.e. Gibbs free energy $\boldsymbol{G}$) with enthalpy $\boldsymbol{H}$ and entropy $\boldsymbol{S}$ is given by **equations 2.2.7**, for a system at any given moment $\boldsymbol{G}$ (**2.2.7.1**), changing state at a constant temperature $\Delta\boldsymbol{G}$ (**2.2.7.2**), and under standard state conditions $\Delta\boldsymbol{G}°$ (**2.2.7.3**).

Equation 2.2.7.1. $G = H - TS$

Equation 2.2.7.2. $\Delta G = \Delta H - T\Delta S$

Equation 2.2.7.3. $\Delta G° = \Delta H° - T\Delta S°$

The 'standard-state free energy of reaction' ($\boldsymbol{\Delta G^{o}}$) is the change in free energy for a system under standard state conditions. It gives a measure of how far away, and in which direction, from equilibrium a system under standard state conditions is. Standard state conditions are a set of conditions for which state related properties have been determined and can be used as a reference point for calculating the same state related properties at non-standard state conditions. The standard state conditions for an aqueous solution of reactant and product species requires all species at 1 M concentration and a pressure of 10^5 Pa. [96].

The ratio between the activity, (effective concentration), of a product and a reactant, or reduced state and oxidised state in the case of an electrochemical system, gives the reaction quotient ($\boldsymbol{Q}$). By comparing the reaction quotient with the equilibrium constant ($\boldsymbol{K^{o}}$) of a system one is able to predict if the system will move towards the reactants or the products or, in the case of electrochemistry, if a positive or negative net current will flow under specified conditions [97]. The term activity refers to a measure of 'effective concentration' and is used to substitute concentration where the properties of a species in a real solution diverge from that of an 'ideal' solution. The activity is given by multiplying the real concentration by an adjustment factor known as the activity coefficient $\boldsymbol{\gamma}$ to account for divergence from an 'ideal' system. In ideal solutions the molecules behave as if in an infinitely dilute solution, thus no interaction between molecules of a species occur. In a real solution the molecules of a dissolved species will not be spaced infinitely apart and thus a degree of interaction, (attractive and repulsive), will exist between molecules. In certain cases the concentration and activity are essentially equivalent, although there are many instances where the value for activity and concentration depart significantly. At high ionic concentrations a phenomenon known as ion pairing becomes relevant, here oppositely charged ions associate as loosely bound pairs, resulting in a decrease in free ionic species and therefore a lower effective concentration/activity. In general, the accuracy declines significantly with concentrations > 10^{-3} M, and calculating the reaction quotient, using only concentrations, is no longer a reliable method. In these cases the mentioned activity coefficients ($\boldsymbol{\gamma}$) must be applied to convert the concentrations into their respective activities [98]. The reaction quotient for the homogenous system $\boldsymbol{\alpha S1_{red} + \beta S2_{ox} \rightleftarrows \sigma S1_{ox} + \tau S2_{red}}$ (where **α**, **β**, **σ,** and **τ**, represent stoichiometric moles) is given in **equation 2.2.8.1**, whilst **equation 2.2.8.2** is for the heterogenous system $\boldsymbol{\beta S_{ox} + \tau e^{-} \rightleftarrows \alpha S_{red}}$, where the electrons $\boldsymbol{\tau(e^{-})}$ are fermi level electrons from the electrode surface and assumed to have an effective concentration of one. It is important to note that only components in the gaseous or aqueous state appear in the equation. Any component which is a pure liquid or a solid, (e.g. electrode), has an effective concentration of one and therefore omitted from the equation.

Equation 2.2.8.1.

$$Q = \frac{(\gamma_{S1_o} \cdot [S1_{ox}]^{\sigma}) \cdot (\gamma_{S2_r} \cdot [S2_{red}]^{\tau})}{(\gamma_{S1_r} \cdot [S1_{red}]^{\alpha}) \cdot (\gamma_{S2_o} \cdot [S2_{ox}]^{\beta})}$$

Equation 2.2.8.2.

$$Q = \frac{(\gamma_{S_o} \cdot [S_{ox}]^{\beta}) \cdot (\gamma_e \cdot [e^{-}]^{\tau})}{(\gamma_{S_r} \cdot [S_{red}]^{\alpha})} \rightarrow Q = \frac{(\gamma_{S_o} \cdot [S_{ox}]^{\beta}) \cdot (1)}{(\gamma_{S_r} \cdot [S_{red}]^{\alpha})} \rightarrow Q = \frac{(\gamma_{S_o} \cdot [S_{ox}]^{\beta})}{(\gamma_{S_r} \cdot [S_{red}]^{\alpha})}$$

The reaction quotient for a system that has reached thermodynamic equilibrium is equal to the equilibrium constant ($\boldsymbol{K^{o}}$). A systems equilibrium constant is directly related to the systems standard-state fee energy (**Equation 2.2.9.3** & **figure 2.2.6**), thus variables that can alter the free energy, like temperature and solvent choice, also determine the equilibrium constant [99]. The relationship between the Gibbs free energy ***ΔG*** and the standard-state Gibbs free energy is presented in **figure 2.2.6**. The equation for the relationship (the line equation) is given in **equation 2.2.9.1** [98], where ***R*** is the ideal gas constant (**$J \cdot mol^{-1} \cdot K^{-1}$**) and ***T*** is the temperature in kelvins (***K***).

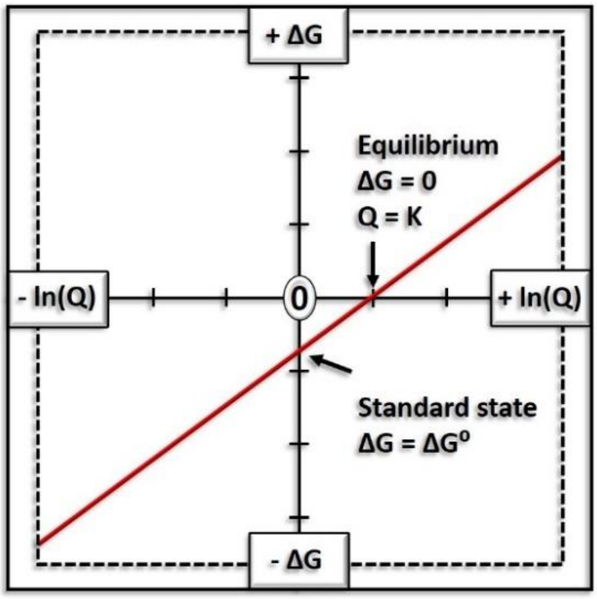

Figure 2.2.6. Relationship between Gibbs free energy and the reaction quotient for a thermodynamically reversible reaction. The Y intercept gives the value for Gibbs free energy under standard state conditions (i.e. activities/concentration of reactants and products is equal to 1). The x-axis intercept is the point at equilibrium, where the systems energy is minimised (***ΔG***=0) and the reaction quotient is equal to the equilibrium constant (***K***). Here the line crosses the x-axis where ln(***Q***) > 0 (i.e. ***Q*** > 1), indicating a state with more product than reactant is thermodynamically preferential to a state where the concentration of reactants is higher.

Equation 2.2.9.1. $\Delta G = \Delta G^{\circ} + RTlnQ$

At equilibrium $\Delta \boldsymbol{G} = \mathbf{0}$ and $\boldsymbol{Q} = \boldsymbol{K}$, resulting in **Equation 2.2.9.2** from **Equation 2.2.9.1**.

Equation 2.2.9.2. $0 = \Delta G^{\circ} + RTlnK$

Rearranging **Equation 2.2.9.2** for $\Delta \boldsymbol{G}^{\circ}$ gives **Equation 2.2.9.3**.

Equation 2.2.9.3. $\Delta G^{\circ} = -RTlnK$

The potential difference across two electrodes in an electrochemical system is correlated with the tendency for the electrochemical reaction to take place and indicates how far away the system is from equilibrium (the smaller the potential difference, the closer the system is to equilibrium). As mentioned, the change in Gibbs free energy for a process specifies the direction and extent a thermodynamic process will spontaneously move (to reach equilibrium). The electrical potential (***V***) of a thermodynamically reversible electrochemical system is directly related to the Gibbs free energy of reaction. More specifically the electrochemical cell potential is equal to the change in free energy per mole of electrons transferred. **Equation 2.2.10.1** & **2.2.10.2** give the relationship for any moment and under standard state conditions respectively. Here ***F*** stands for the Faraday constant and **n** for the stoichiometric number of electrons involved in the reaction.

Equation 2.2.10.1. $\Delta G = -nFE$

Equation 2.2.10.2. $\Delta G^{\circ} = -nFE^{\circ}$

Substituting for $\Delta \boldsymbol{G}^{\circ}$, in **Equation 2.2.9.3** with **Equation 2.2.10.2**, gives **Equation 2.2.11**.

Equation 2.2.11. $nFE^{\circ} = RTlnK$

Substituting for $\Delta \boldsymbol{G}^{\circ}$ and $\Delta \boldsymbol{G}$ in **Equation 2.2.9.1** with **Equation 2.2.10.2** and **Equation 2.2.10.1** respectively, gives **Equation 2.2.12.1**.

Equation 2.2.12.1. $-nFE = -nFE^{\circ} + RTlnQ \rightarrow nFE = nFE^{\circ} - RTlnQ$

Rearranging **Equation 2.2.12.1** for $\boldsymbol{E}$, leads to the famous Nernst equation (**Equation 2.2.12.2**), which describes the relationship between the potential at any moment with the standard state potential via the reaction quotient.

Equation 2.2.12.2. $E = E^{\circ} - \frac{RT}{nF} lnQ$

Equation 2.2.12.3. $E = E^{\circ} - \frac{2.303 \cdot RT}{nF} logQ$

at 25 ^{o}c $\rightarrow E = E^{\circ} - \frac{0.059}{n} logQ$

The Nernst equation is arguably one of the most useful equations in electrochemistry and has wide ranging applications [98]. For example, it can be used to relate equilibrium cell potentials to concentration gradients across biological membranes, or to assess whether a given reaction will go to completion under a given set of conditions, or to evaluate the extent of complexation for an electrochemically active ion. An important factor in determining the potential for many electrochemical systems, not mentioned thus far, is pH. From the Nernst equation it is easy to perceive the relationship between the electrode potential and pH for proton coupled reactions where the concentration of protons **$[H^+]$** will factor into the reactant quotient along with concentrations of other reactants and products. At potentials outside a variable window, determined by the system, water is broken down in a process that effectively generates protons at oxidative potentials and consumes protons at reductive potentials. Because applying a potential can affect the local pH and the pH in turn can affect the measured potential, in systems with proton coupled redox reactions, artefacts such as crossovers can be observed in CV with highly oxidative or reductive potential limits.

2.2.8 Kinetics

2.2.8.1 The Arrhenius Equation

The rate of reaction at the electrode (and therefore current) is controlled by both mass transport and the electron transfer kinetics. At low overpotentials the net rate of reaction in one direction is determined almost completely by electron transfer kinetics. In this potential region the relationship between rate and potential is explained adequately by models for electron transfer. At higher overpotentials the reaction rate becomes limited predominantly by mass transport and the rate of reaction does not represent the electron transfer rate. The potential window wherein electron transfer kinetics are visible can be broadened by stirring or employing micro electrodes to mitigate the effects of mass transfer (i.e. delay the potential at which mass transfer becomes limiting). However, the rate of reaction will always be restricted by mass transfer at high enough overpotentials.

To explain the differences in rates (kinetics) of reactions one requires a model which can predict experimentally observable phenomena. Several such models have been developed, including relatively simple models that can predict relationships within certain limits, along with more extensive models which are more accurate for a greater range of conditions, but are more complex. For example, the Butler-Volmer model provides a relatively simple yet useful way of predicting rates from electrode potentials. In comparison the more complex model developed by Marcus predicts some significant phenomena observed experimentally and importantly explains electron transfer in 'outer sphere' redox reactions. A model developed by Gerischer [100] has proven especially useful for explaining electron transfer in systems using semiconductor electrodes. Gerischer's model is based on the idea that electrons can transfer from any occupied energy state of a donor into an unoccupied overlapping energy state of an acceptor [98].

The kinetic models outlined in this chapter all incorporate the concept of a heightened energy state, (transition state), required by the reactants before a reaction can occur. For a reversible reaction, regardless of the difference in free energies between reactants and products, the ground states of both reactant and product are considered to have energies corresponding to local minima, separated by an energy barrier between the two states as in **figure 2.2.7**. The rate of reaction is then determined by the height of this energy barrier relative to that of the ground states (energy of activation $\boldsymbol{E_A}$ or Gibbs free energy of activation $\Delta\boldsymbol{G}^{\ddagger}$). The relationship between reaction rate constant $\boldsymbol{k}$ and activation energy $\boldsymbol{E_A}$ is an important one which any kinetic model must address. An historically relevant, empirical derived, approximation of this relationship is given by the Arrhenius equation (**equation 2.2.13.1**)[87]. Here $\boldsymbol{\mathcal{A}}$ (the Arrhenius constant) is a frequency factor, commonly thought to be representing the frequency of attempts a system makes to overcome the activation energy barrier.

Equation 2.2.13.1. $$k = \mathcal{A}e^{\frac{-E_A}{RT}}$$

Equation 2.2.13.2. $$k = \mathcal{A}'e^{\frac{-(\Delta H^{\ddagger} - T\Delta S^{\ddagger})}{RT}}$$

Equation 2.2.13.3. $$k = \mathcal{A}'e^{\frac{-\Delta G^{\ddagger}}{RT}}$$

Activation energy can be substituted by the change in enthalpy from ground state to activation/transition state and entropy factored in to give **equation 2.2.13.2** and thus **equation 2.2.13.3** **[98]**. Here $\Delta\boldsymbol{G}^{\ddagger}$ is the standard free energy of activation, $\Delta\boldsymbol{H}^{\ddagger}$ is the standard enthalpy of activation and $\Delta\boldsymbol{S}^{\ddagger}$ is the standard entropy of activation.

The relavance of the Arrhenius equation is not just isolated to reaction kinetics, it can also be used to model other thermally induced processes such as the temperature dependance of diffusion coeficients and biological processes in foods (for predicting shelf lifes) [101]. The Arrhenius equation has proven practicaly very useful and has provided the foundations for more detailed models in the form of Eerings equation and transition state theory. The Eering equation is very similar to the Arrhenius equation but addressess previously oversimplified factors. For example, the pre-exponential factor in the Arrhenius equation is a simple constant yet, in reality, the pre-exponential factor is not constant, althought the variations are difficult to observe experimentaly. In the Eering equation, the pre-exponential factor is broken down to reveal a temperature dependance in addition to the exponential temperature dependance. The Eering equation can be derived using transition state theory as detailed bellow.

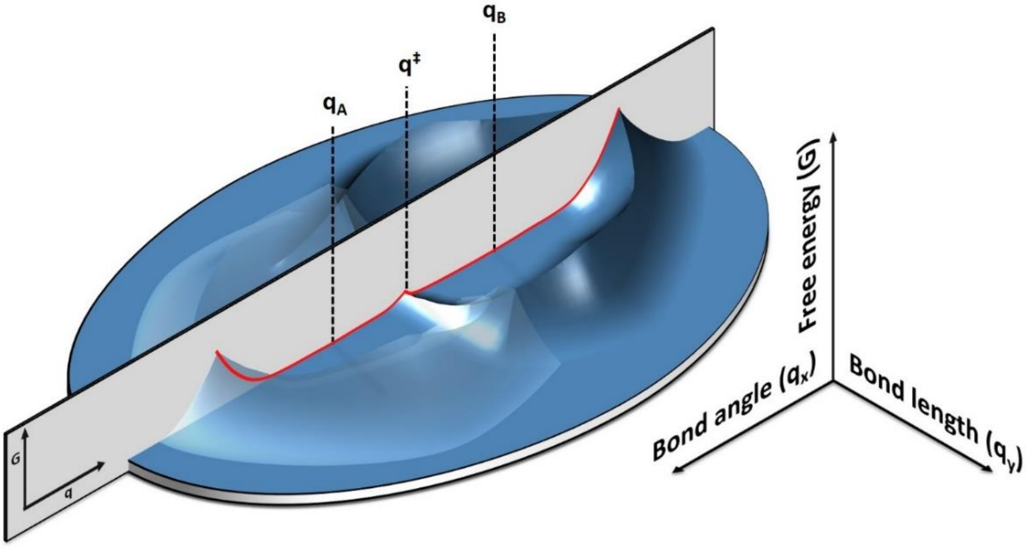

Figure 2.2.7 Cartoon depicting an idealised, multidimensional potential energy surface of a reaction system. Here, only three dimensions have been used but many more dimensions could be used, depending on the reaction system. Each dimension, in addition to free energy, represents a different parameter of the reactants/products and their local environment, such as vibrational energies, ligand bond lengths, solvent polarisation and orientation, bond angles within the reactant molecule, etc.. In this cartoon, a specific bond angle (**q_x**) is represented by the x-axis, and a specific bond length (**q_Y**) by the y-axis. A plane has been placed through the least expensive path between reactant ground state (**q_A**) and product ground state (**q_B**). The 2D plane representation of the potential energy surface has free energy as the y-axis and a reaction quotient for the x-axis (**q**). The reaction quotient is an abstract variable, representing the original multi-dimensional parameters, i.e. bond length and angle in the cartoon depicted here.

2.2.8.2 Transition state theory

Models used to explain variations in electron transfer kinetics between different reaction systems usually involve the concept of a transition state $\mathbb{T}$, representative of the previously mentioned heightened energy state required for conversion of one stable state **A,** (reactants), into another stable state **B** (products). The transition state $\mathbb{T}$ is considered a temporary state in between reactants **A** and products **B** that shares characteristics with both. For example, the redox system $[\boldsymbol{A}] + [\boldsymbol{e}^-] \rightleftharpoons [\boldsymbol{B}^-]$, including a transition state could be written as $[\boldsymbol{A}] + [\boldsymbol{e}^-] \rightleftharpoons [\mathbb{T}] + [\boldsymbol{e}^-] \rightleftharpoons [\mathbb{T}^-] \rightleftharpoons [\boldsymbol{B}^-]$ or simply as $[\boldsymbol{A}] \rightleftharpoons [\mathbb{T}] \rightleftharpoons [\boldsymbol{B}]$, where state **A** is inclusive of the fermi level electron from the electrode surface and the oxidised form of a redox active species and state **B** is the reduced form of the redox species. The forward rate of reaction $\boldsymbol{v_f}$ can be calculated, either using the concentration of ground state reactants **[A]** multiplied by a rate constant $\boldsymbol{k_f}$ (**equation 2.2.14**), or using the concentration of the reactant species in the transition state **[$\mathbb{T}$]** multiplied by a frequency factor $\boldsymbol{f_{\mathbb{T}b}}$ (**equation 2.2.15**). The frequency factor $\boldsymbol{f_{\mathbb{T}b}}$ determins the probability a molecule in the transition state will relax into the product ground state.

Equation 2.2.14. $$v_f = k_f[A]$$

Equation 2.2.15. $$v_f = f_{\mathbb{T}b}[\mathbb{T}]$$

Equation 2.2.16. $$K_C^{\ddagger} = \frac{[\mathbb{T}]}{[A]}$$

Whilst **A** is in equilibrium with **B**, **A** and **B** must also be in equilibrium with $\mathbb{T}$. The forward equilibrium constant $\boldsymbol{K_C^{\ddagger}}$ between **A** and $\mathbb{T}$ is given by **equation 2.2.16**. Rearranging **equation 2.2.16** for $[\mathbb{T}]$ and substituting into **equation 2.2.15**, leads to **equation 2.2.17.1**. **Equations 2.2.14** & **2.2.17.1** can then be combined to give **equation 2.2.17.2**.

Equation 2.2.17.1. $$v_f = f_{\mathbb{T}b}[A]\, K_C^{\ddagger}$$

Equation 2.2.17.2. $$k_f[A] = f_{\mathbb{T}b}[A]K_C^{\ddagger} \rightarrow k_f = f_{\mathbb{T}b}K_C^{\ddagger}$$

The frequency factor $\boldsymbol{f_{\mathbb{T}b}}$ can be aproximately treated as the molecular vibrational frequency, in which case $\boldsymbol{f_{\mathbb{T}b}}$ is given by **Equation 2.2.18.1**. Here $\boldsymbol{k_B}$ is the Boltzmann constant, $\boldsymbol{T}$**,** is the temperature in Kelvin and $\boldsymbol{h}$ is Plank's constant. Substituting for $\boldsymbol{f_{\mathbb{T}b}}$ in **Equation 2.2.17.2** with **Equation 2.2.18.1**, leads to **equation 2.2.18.2**.

Equation 2.2.18.1. $f_{\mathbb{T}b} = \frac{k_B T}{h}$

Equation 2.2.18.2. $k_f = \frac{k_B T}{h} K_C^{\ddagger}$

Because **A** is in equilibrium with $\mathbb{T}$, the thermodynamic **equations 2.2.7.3 + 2.2.9.3** become relevant and can be applied to the Gibbs free energy of activation $\Delta\boldsymbol{G}^{\ddagger}$ (**equations 2.2.19 + 2.2.20.1**). Combining **equations 2.2.19** & **2.2.20.1** leads to **equation 2.2.20.2**.

Equation 2.2.19. $\Delta G^{\ddagger} = \Delta H^{\ddagger} - T\Delta S^{\ddagger}$

Equation 2.2.20.1. $\Delta G^{\ddagger} = -RTlnK_C^{\ddagger} \rightarrow K_C^{\ddagger} = e^{-\frac{\Delta G^{\ddagger}}{RT}}$

Equation 2.2.20.2. $\Delta H^{\ddagger} - T\Delta S^{\ddagger} = -RTlnK_C^{\ddagger} \rightarrow lnK_C^{\ddagger} = \frac{\Delta S^{\ddagger}}{R} - \frac{\Delta H^{\ddagger}}{RT} \rightarrow K_C^{\ddagger} = e^{\frac{\Delta S^{\ddagger}}{R}} e^{-\frac{\Delta H^{\ddagger}}{RT}}$

Substitution for $K_C^{\ddagger}$ in **equation 2.2.18.2**, with **equation 2.2.20.1** or **equation 2.2.20.2**, results in the Eyring Equation (**equations 2.2.21.1**). The general form of the Eyring Equation is **Equation 2.2.21.2**, which one can see is of a similar format to the Arrhenius equation (**equation 2.2.13.1-c**). The Eyring Equation is frequently used for describing the variance of temperture and was fundamental for development of transition state theory [102]. The pre-exponential factor of the Eyring Equation can include a transmission factor $\boldsymbol{\kappa}$ which takes the value between zero and one. The transmision coeficient $\boldsymbol{\kappa}$ represents the faction of transition states, arising from **A** → $\mathbb{T}$ which convert into **B** as aposed to relaxing back into **A**. The transmission efficiency is frequently assumed to be 100%, thus avoiding the requirment of the extra pre-exponential factor.

Equation 2.2.21.1. $k_f = \frac{k_B T}{h} e^{\frac{\Delta S^\ddagger}{R}} e^{-\frac{\Delta H^\ddagger}{RT}}$

Equation 2.2.21.2. $k_f = \frac{k_B T}{h} e^{-\frac{\Delta G^\ddagger}{RT}}$

For the reversible reaction between state **A** and **B** (**A + e$^-$ ⇄ B$^-$**), the forward rate of reaction ***v$_f$***, is related to the concentration $\boldsymbol{C_A(0,t)}$ of reactants **A** at the electrode surface $\boldsymbol{x = 0}$ at time $\boldsymbol{t}$, by a rate constant ***k$_f$***, by **equation 2.2.22.1**. As noted previously the rate is directly related to the current. Here $\boldsymbol{i_a}$ represents the anodic current for the oxidation process. The net reaction rate ***v$_{net}$*** from state **A** to **B**, by taking into consideration the rate of reaction in the reverse direction ***v$_r$***, is therefore given by **equation 2.2.22.2**. Rearrangement of **equation 2.2.22.2** for $\boldsymbol{i}$, results in **equation 2.2.22.3**.

Equation 2.2.22.1. $v_f = k_f C_A(0,t) = \frac{i_a}{nF\mathbb{A}}$

Equation 2.2.22.2. $v_{net} = v_f - v_r = k_f C_A(0,t) - k_r C_B(0,t) = \frac{i_a}{nF\mathbb{A}} - \frac{i_c}{nF\mathbb{A}} = \frac{i}{nF\mathbb{A}}$

Equation 2.2.22.3. $i = i_a - i_c = nF\mathbb{A}[k_f C_A(0,t) - k_r C_B(0,t)]$

If the electrode potential is at the systems formal potential $\boldsymbol{E = E^{o\prime}}$, and the system can equilibrate, then $\boldsymbol{C_A(\infty,t) = C_A(0,t) = C_B(0,t) = C_B(\infty,t)}$ and $\boldsymbol{\Delta G^\ddagger_{0A} = \Delta G^\ddagger_{0B}}$ (**figure 2.2.9**). Increasing the electrode potential $\boldsymbol{E}$ by $\boldsymbol{\Delta E}$, causes a concurrent increase in the relative potential energy of electrons at the surface of the electrode. The shift in electron potential energy is proportional to the change in electrode potential by **equation 2.2.23**, where $\boldsymbol{F}$ is the Faraday constant.

Equation 2.2.23. $-F\Delta E = -F(E - E^{0\prime})$

A change in electrode potential is also related to the free energy of activation, by **equation 2.2.24.1**, for the reactant side (state **A**) and **equation 2.2.24.2** for the product side (state **B**). Idealised reaction co-ordinates of the discussed system ($\mathbf{A + e^- \rightleftarrows B^-}$) are illustrated in **figure 2.2.8**, here the relationship between applied potential and free energy of activation (and thus reaction rate) can be visualised. The transfer coefficient $\boldsymbol{\alpha}$ is dependent on the shape of the systems potential energy surface at the transition state. It is easy to see from **figure 2.2.9**, that the value of $\boldsymbol{\alpha}$ is always between 0 and 1 as it is a ratio which attributes the effect of changing potential between the activation energy of the reactants and products.

Equation 2.2.24.1. $$\Delta G_A^{\ddagger} = \Delta G_{0A}^{\ddagger} - \alpha F(E - E^{0\prime})$$

Equation 2.2.24.2. $$\Delta G_B^{\ddagger} = \Delta G_{0B}^{\ddagger} + (1 - \alpha)F(E - E^{0\prime})$$

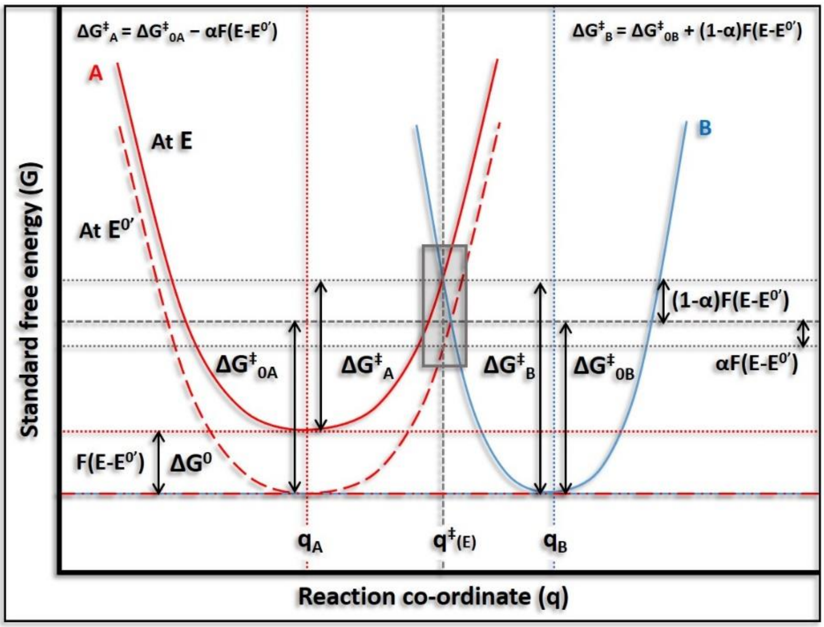

Figure 2.2.8. Potential energy curves representing the example electrochemical system ($\mathbf{A + e^- \rightleftarrows B^-}$), depicting how the transition state models relate changes in applied potential with the free energies of activation $\Delta G^{\ddagger}$ and the free energy of reaction $\Delta \boldsymbol{G}^{\mathbf{0}}$. The **red** curve labelled **A** represents the summation of energies for species A and the electrode electron at the fermi level corresponding to the applied potential **E**. The dashed red line represents **A** and the electron at the fermi level corresponding to the systems formal potential (**E$^{0\prime}$**). The **blue** line is the energy curve for the product **B**. The area around the crossover point between A and B, covered by the grey box is enlarged in **figure 2.2.9**.

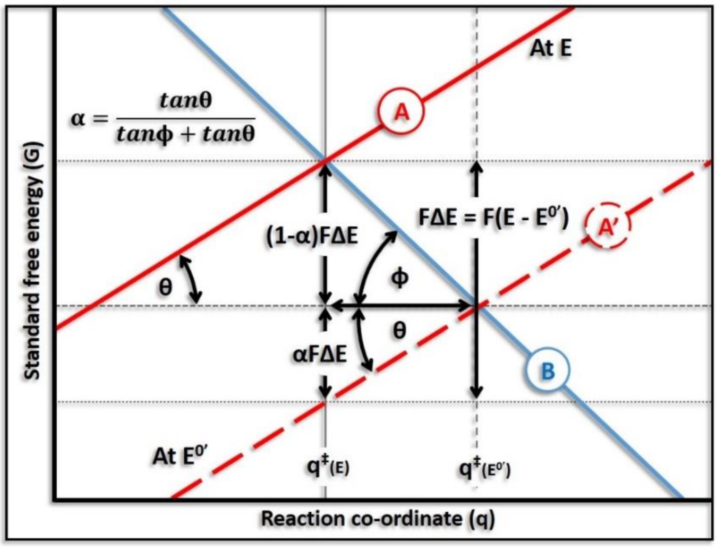

Figure 2.2.9. Enlargement of the area surrounding the crossover point, covered by the grey box, in **figure 2.2.8** to give a visual interpretation of what the transfer coefficient $\boldsymbol{\alpha}$ represents in the transition state model. Here **θ** and **ϕ** are the angles of intercept for the **A** and **B** energy curves respectively. If **θ = ϕ**, the intersection is symmetrical and from the equation in the top left corner one can see that α will equal 0.5. **q‡(E)** and **q‡(E$^{0'}$)** are the crossover (transition state) reaction co-ordinates for potential **E** and the formal potential (**E$^{0'}$**) respectively.

As discussed previously, when the relationship between a reactions rate constant and the free energy of activation is derived, either empirically or using transition state theory (Eyring's equation), one ends up with an Arrhenius type equation, (**equation 2.2.25**), where $\boldsymbol{\mathcal{A}'}$ is the pre-exponential factor. The free energy of activation $\Delta\boldsymbol{G}^{\ddagger}$ can be substituted with the standard state free energy of activation $\Delta\boldsymbol{G}_{\boldsymbol{0}}^{\ddagger}$, using **equations 2.2.24.1** and **2.2.24.2**, for the forward and reverse reactions resulting in **equations 2.2.26.1** and **2.2.26.2** respectively. Contributions to the resulting activation energy at potential $\boldsymbol{E}$ ($\Delta\boldsymbol{E}$ from the formal potential $\boldsymbol{E}^{\boldsymbol{0}\prime}$) can be separated into those inherent to the system and independent of changing potentials, represented by the standard rate constant, and the part determined by the potential. Thus, **equations 2.2.26.1** and **2.2.26.2** can be re-written as **equations 2.2.26.3** and **2.2.27**, where the potential independent portion of **equations 2.2.26.1** and **2.2.26.2** is simplified into the standard rate constant $\boldsymbol{k}^{\boldsymbol{0}}$. Further substitution of both **2.2.26.3** and **2.2.27** into **equation 2.2.22.3**, yields **equation 2.2.28** otherwise known as the Buttler-Volmer equation which describes the current potential relationship.

Equation 2.2.25. $k = \mathcal{A}'e^{\frac{-\Delta G^{\ddagger}}{RT}}$

Equations 2.2.26.1. $k_f = \mathcal{A}'_f e^{\frac{-\Delta G^{\ddagger}_{0A} - \alpha F(E-E^{0\prime})}{RT}} \xrightarrow{f=\frac{F}{RT}} k_f = \mathcal{A}'_f e^{\frac{-\Delta G^{\ddagger}_{0A}}{RT}} e^{-\alpha f(E-E^{0\prime})}$

Equations 2.2.26.2. $k_r = \mathcal{A}'_r e^{\frac{-\Delta G^{\ddagger}_{0B} + (1-\alpha)F(E-E^{0\prime})}{RT}} \xrightarrow{f=\frac{F}{RT}} k_r = \mathcal{A}'_r e^{\frac{-\Delta G^{\ddagger}_{0B}}{RT}} e^{(1-\alpha)f(E-E^{0\prime})}$

Equation 2.2.26.3. $k_f = k^0 e^{-\alpha f(E-E^{0\prime})}$

Equation 2.2.27. $k_r = k^0 e^{(1-\alpha)f(E-E^{0\prime})}$

Equation 2.2.28. $i = nF\mathbb{A}k^0[C_A(0,t)e^{-\alpha f(E-E^{0\prime})} - C_B(0,t)e^{(1-\alpha)f(E-E^{0\prime})}]$

The Buttler-Volmer equation is used extensively for solving problems related to heterogeneous electron transfer. The standard rate constant $\boldsymbol{k^0}$ of an electrochemical system is a measure of the electron transfer rate at the working electrode. Large $\boldsymbol{k^0}$ values indicate the rate of electron transfer is fast thus, on changing the electrode potential, equilibrium will be reached rapidly and the system may be referred to as fully reversible. Systems with low $\boldsymbol{k^0}$ values have high activation energies which slow down the rate of electron transfer and result in irreversible electrochemical behaviour. Electrochemical systems with alpha $\boldsymbol{\alpha}$ values close to 0.5 have symmetrical rate changes on varying the potential, either side of the formal potential, for the forward and reverse reactions. If the transfer coefficient $\boldsymbol{\alpha}$ value diverges significantly from 0.5, either towards 0 or towards 1, the forward and reverse kinetics take on a lopsided character. For an electrochemical system (**A + e**$^-$ **⇄ B**$^-$) with a high $\boldsymbol{k^0}$ value but a transfer coefficient $\boldsymbol{\alpha}$ value of ~0.8 one can see from the Buttler-Volmer equation, (**equation 2.2.28**), that only small overpotentials are required to reach large reduction currents, (assuming no mass transport limits), whilst much greater overpotentials in the opposite direction would be required to reach equivalent oxidative currents. The cause of this effect can be visualised in **figure 2.2.9** where the relationship between the transfer coefficient $\boldsymbol{\alpha}$ and the distribution of energy, from changes in applied potential, to the activation energies of the forward and reverse reaction, is determined by the relative steepness in potential energy surfaces of the reactant and product states.

2.2.8.3 Inner and Outer Sphere Electron Transfer

Thus far, no detail has been given to the mechanisms of electron transfer between electrodes and redox active species. Developing accurate mechanistic models for electron transfer reactions provides an advantage for understanding why certain reactions are faster than others. Without addressing the mechanistic aspect of reaction kinetics, one cannot expect to derive a realistic kinetic model for predicting electrochemical phenomena. There are two distinct mechanisms by which electron transfer between reaction centres is achieved, inner sphere and outer sphere electron transfer. Both can occur simultaneously in the same reaction system although one will usually dominate. If the example reaction above (i.e. $\mathbf{A + e^- \rightleftarrows B^-}$) follows an inners sphere electron transfer mechanism one would expect to find a strong interaction between the species and the electrode. This strong interaction can be facilitated by sharing of a ligand between the redox species and the electrode to create a ligand bridge. For example inner sphere electron transfer during $Cr(H_2O)_5^{2+}$ oxidation on a mercury electrode a Cl^- ligand of $Cr(H_2O)_5^{2+}$ can absorb strongly to the mercury and act as bridge for electron transfer [98]. Orbital symmetries between reaction centres and the bridging ligand provides a pathway for electron transfer. A key feature of inner sphere electron transfer, and what differentiates it from outer sphere, is the making and braking of bonds requiring a strong interaction between donor and acceptor. In the case of outer sphere electron transfer there are no strong interactions between reaction centres or a convenient ‘bridge’ to facilitate electron transfer. Instead polarisation of ‘free’ outer sphere solvent molecules play a central role in forming a transition state. Energy must be supplied to the reactants, (e.g. through the transfer of thermal energy from solvent molecules), to reach the higher energy transition state **T**. Increased energy allows for reorganisation of free solvent molecules in the outer shell in addition to small changes in the bond lengths of **A** or **B**. The energy required to reach the transition state from the reactant’s ground state is determined by a crossover point where characteristics such as bond lengths and solvent orientation are in a feasible, but unstable, state for both reactants and products. At this point, once donor and acceptor orbital energies are equal and overlapping, electron transfer may proceed via tunnelling [98].

2.2.8.4 Marcus Theory

Central to Marcus theory is the Frank-Cordon principle. According to the Frank-Cordon principle, Electron transfer between the electrode and redox active species, (in the aqueous phase), occurs instantaneously, relative to the timescales involve in nuclear motion, and without absorption or emission of radiation. Thus, energy levels for the transferring electron on the donor and acceptor must overlap and the reacting species cannot undergo any structural changes, (e.g. ligand bond length shortening or lengthening or rearrangement of associated solvent molecules), during the electron transfer process. Consequently, at the point of electron transfer the reacting species must exist in a state that is viable with and without the transferring electron.[98]

From the model proposed by Marcus, as with previous models, an Arrhenius style equation, (**equation 2.2.29**), can be derived to relate the kinetics (rate constant) with the free energy of activation. Here the pre-exponential factor is broken into three parts as opposed to just a frequency factor as in the Eyring equation. Included is a precursor equilibrium constant $\boldsymbol{K_{P,A}}$, (**equation 2.2.30**), referring to the concentration ratio of species in the 'reactive position' at the electrode surface $\boldsymbol{C_{A,surf}}$ (in the case of heterogenous reactions) to the bulk concentration $\boldsymbol{C_A^*}$. A nuclear frequency factor $\boldsymbol{v_n}$ related to attempts at overcoming the energy barrier and determined in part by bond vibrations and the kinetic energy of associated solvent molecules. The electronic transmission coefficient $\boldsymbol{\kappa_{el}}$, which gives the probability of electron tunnelling events which is primarily determined by the distance of the species from the electrode surface [98].

Equation 2.2.29. $$k_f = K_{P,A} v_n \kappa_{el} e^{\frac{-\Delta G_f^{\ddagger}}{RT}}$$

Equation 2.2.30. $$K_{P,A} = \frac{C_{A,surf}}{C_A^*}$$

As with previous models, Marcus theory depicts the reaction occurring on a Hamiltonian surface (i.e. potential energy surface). Collapsing the dimensions of the Hamiltonian surface along the plane representing the 'easiest' (lowest energy) path between state **A** (reactant) and state **B** (product), allows one to map the reaction progress in terms of reaction co-ordinate $\boldsymbol{q}$. For a system involving outer sphere electron transfer, assuming the electrochemically active species in state **A** is at a fixed position from the electrode, the reaction co-ordinate is varied by fluctuations in vibrational and rotational motion of the species and alterations in the position and orientation of solvent molecules. The standard free energy for **A** ($\boldsymbol{G_A^0}$) and **B** ($\boldsymbol{G_B^0}$) is assumed to depend quadratically with the reaction co-ordinate $\boldsymbol{q}$ as shown in **equations 2.2.31.1** and **2.2.32.1** for state **A** and **B** respectively with $\boldsymbol{G_A^0(q_A)}$ set as a reference point (i.e. $\boldsymbol{G_A^0(q_A) = 0}$), so that the activation energy for the forward reaction ($\Delta\boldsymbol{G_f^\ddagger}$) is equivalent to the standard free energy for **A** ($\boldsymbol{G_A^0}$) at the transition state coordinate $\left(\boldsymbol{q^\ddagger}\right)$ (i.e. $\Delta\boldsymbol{G_f^\ddagger} = \boldsymbol{G_A^0(q^\ddagger)}$) [98]. In **equations 2.2.31.1** and **2.2.32.1** $\boldsymbol{k}$ is a force constant relating to changes in bond length whilst $\boldsymbol{q_A}$ and $\boldsymbol{q_B}$ are the equilibrium atomic configurations for state **A** and **B** respectively.

Equation 2.2.31.1. $$G_A^0(q) = \left(\frac{k}{2}\right)(q - q_A)^2$$

$\xrightarrow{for\ q=q^\ddagger}$ **2.2.31.2**. $$G_A^0(q^\ddagger) = \left(\frac{k}{2}\right)\left(q^\ddagger - q_A\right)^2$$

Equation 2.2.32.1. $$G_B^0(q) = \left(\frac{k}{2}\right)(q - q_B)^2 + \Delta G^0$$

$\xrightarrow{for\ q=q^\ddagger}$ **2.2.32.2**. $$G_B^0\left(q^\ddagger\right) = \left(\frac{k}{2}\right)\left(q^\ddagger - q_B\right)^2 + \Delta G^0$$

Equation 2.2.33. $$\lambda = \left(\frac{k}{2}\right)(q_B - q_A)^2$$

Equation 2.2.34. $$\lambda = \lambda_i + \lambda_o$$

In the case of the electrochemical example system, (**A + $\mathbf{e^-}$ ⇄ $\mathbf{B^-}$**), the potential energy surface curve representing the reactants is the sum of the energies for oxidant **A** and the electron, at the fermi level corresponding to the applied potential **E**, from the electrode. Thus, the curve representing the products (state **B**), in this example, is just the energy curve of the reduced species. The electron transfer between the electrode and accepting species

A occurs at the transition state, denoted by the crossover of energy curves at the reaction co-ordinate $\boldsymbol{q}^{\ddagger}$ (**figure 2.2.8**). At the transition state $\boldsymbol{G_A^0}(\boldsymbol{q}^{\ddagger}) = \boldsymbol{G_B^0}(\boldsymbol{q}^{\ddagger})$, one can solve $\boldsymbol{q}^{\ddagger}$ in **equations 2.2.35** from **equations 2.2.31.2 + 2.2.32.2**. Keeping the same reference as stated above ($\boldsymbol{G_A^0}(\boldsymbol{q_A}) = \boldsymbol{0}$), so that $\Delta\boldsymbol{G_f^{\ddagger}} = \boldsymbol{G_A^0}(\boldsymbol{q}^{\ddagger})$, one can then derive **equation 2.2.36**, with the re-substation of **equation 2.2.35** for $\boldsymbol{q}^{\ddagger}$, into **equation 2.2.31.2**. Applying the reorganisation energy $\boldsymbol{\lambda}$ (**Equation 2.2.33**) to **equation 2.2.36** yields **equation 2.2.37.1**, and substituting $\boldsymbol{F}(\boldsymbol{E} - \boldsymbol{E^0})$ for $\Delta\boldsymbol{G^0}$ into **equation 2.2.37.1** gives **2.2.37.2**.

The reorganisation energy ($\boldsymbol{\lambda}$) is the energy required to make the changes in molecular configuration from the ground state reaction co-ordinate ($\boldsymbol{q_A}$) of reactant **A** to the product **B** ground state co-ordinate ($\boldsymbol{q_B}$). The energy attributed to reactant species (**A**) configuration alterations is termed the 'inner reorganisation energy $\boldsymbol{\lambda_i}$, whilst the energy for solvent re-arrangement and polarisation is the outer reorganisation energy $\boldsymbol{\lambda_o}$.

Like all models reality has been simplified and for a real system the free energy of activation is affected by more than just bond vibrations and solvent orientation. Free energy is also involved in getting the species to the correct location, for example in overcoming electrostatic effects. To take into consideration extra contributions to the free energy of activation additional work terms, $\boldsymbol{w_A}$ and $\boldsymbol{w_B}$ for **A** and **B** respectively**,** can be included into **equation 2.2.37.2** to yield **equation 2.2.37.3**.

Equation 2.2.35.
$$q^{\ddagger} = \left(\frac{q_A+q_B}{2}\right) + \frac{\Delta G^0}{k(q_B-q_A)}$$

Equation 2.2.36.
$$\Delta G_f^{\ddagger} = \left(\frac{k(q_B-q_A)^2}{8}\right)\left(1 + \frac{2\Delta G^0}{k(q_B-q_A)^2}\right)^2$$

Equation 2.2.37.1.
$$\Delta G_f^{\ddagger} = \left(\frac{\lambda}{4}\right)\left(1 + \frac{\Delta G^0}{\lambda}\right)^2$$

Equation 2.2.37.2.
$$\Delta G_f^{\ddagger} = \left(\frac{\lambda}{4}\right)\left(1 + \frac{F(E-E^0)}{\lambda}\right)^2$$

Equation 2.2.37.3.
$$\Delta G_f^{\ddagger} = \left(\frac{\lambda}{4}\right)\left(1 + \frac{F(E-E^0)+w_B-w_A}{\lambda}\right)^2$$

Marcus theory can be used to estimate the transfer coefficient **α** and predict how the transfer coefficient depends on the potential. In comparison the earlier Butler Volmer model was only able to incorporate the transfer coefficient as a factor dependent on potential but has no basis for predicting the way in which the coefficient is related. From **figure 2.2.9** one can see that the free energy of activation for the forward reaction ($\Delta G_f^{\ddagger}$) is related to the transfer coefficient **α** by **equation 2.2.38**. Rearrangement of **equation 2.2.38** and application of **equation 2.2.37.2** leads to **equation 2.2.39** which can be used to estimate values for the transfer coefficient **α**. Another notable prediction derived from the Marcus model of electron transfer is the existence of an inverted region which is reached for certain systems involving very high driving forces between states. As the free energy of reaction increases, (High energy state for **A** relative to **B**), the free energy of activation decreases, thus the reaction rate increases up until the minimum point (crossover point) where the free energy of activation becomes effectively zero. After this point, on increasing the driving force further, the activation energy begins increasing for certain reaction systems resulting in a reduction of the kinetics. However, once the crossover point has been reached in an electrochemical system the kinetics will plateau. Unlike a redox reaction between two individual molecules with discrete electronic energy states, bulk electrodes effectively have a continuum of energy states. Consequently, even past the crossover point, energy states where the energy of activation is zero still exist and maximum kinetics can be maintained.

Equation 2.2.38 $$\Delta G_f^{\ddagger} = \alpha F(E - E^0) \quad \rightarrow \quad \alpha = \frac{1}{F}\frac{\Delta G_f^{\ddagger}}{(E-E^0)}$$

Equation 2.2.39 $$\alpha = \frac{1}{2} + \frac{F(E-E^0)}{2\lambda}$$

2.2.9 Electrochemical Definitions

The following are definitions of some fundamental electrochemistry terms in addition to an explanation of a small set of symbols and nomenclature used frequently during this chapter.

Electrochemically active species: Any species that can be oxidised (lose electrons) or reduced (gain electrons) by an electrode, which has been poised at the appropriate potential.

Standard electrode potential (E°): The potential of a redox system at standard state. Standard state refers to solutes, (both oxidised and reduced forms of a species if applicable), at 1 M effective concentration so that their activities are at unity, and gases at a pressure of ~1 atm or 10^5 Pa. The standard temperature is usually 25 °C.

Formal Potential ($E^{0'}$): The potential of a redox couple with the oxidised and reduced forms at 1 M concentrations under standard/specified conditions. The formal potential is similar to the standard potential except it is defined with concentrations instead of activities thus making it a more practical measure.

Equilibrium potential (E_{eq}): The potential at which the forward and backward reaction rates are equal. At open circuit, if a redox couple exists with an exchange rate > 0, electrons are transferred in both directions between electrode and solution. In such a circumstance the electrode potential at equilibrium is determined by the ratio of concentrations for the oxidised and reduced forms of the redox active species. The following is a qualitative explanation for how the equilibrium potential is determined by relative concentrations. If, at the electrode surface, a difference exists between the initial electrode potential and the potential required for the starting ratio between oxidised and reduced species to exist at equilibrium, then the rates of the redox reactions at the electrode surface will be unbalanced resulting in a net charge transfer between electrode and redox active species. Although the is a net conversion of species occurring at the electrode surface, the amounts are unlikely to be sufficient to significantly change the ratio of concentrations in the bulk. If the circuit is open, charge will build up on the electrode surface, this change in surface charge leads to a change in electrode potential. Alterations in electrode potential also adjusts the relative rates of reaction for oxidation and reduction. Once the rates for oxidation and reduction are equivalent the potential will also become stable and the equilibrium potential is reached. The equilibrium potential is thus determined by the relative concentrations of reduced and oxidised species. The formal and standard potentials are equilibrium potentials under specified conditions.

Chemical reversibility: In relation to electrochemical systems this refers to reversible redox reactions where both the oxidised and reduced form of a species are stable to homogenous chemical reactions in solution. In this context the term ‘stable’ is relative to the time scale of the experiment. It is therefore possible for an electrochemical reaction to appear reversible in one experiment, whilst irreversible with a slight variation to the experimental procedure. For example, in a system containing an electrochemically active species **S**, starting in a stable reduced form $\mathbf{S_{red}}$. On oxidation of $\mathbf{S_{red}}$, a chemically un-stable radical may be generated $\mathbf{S_{ox}}^{\cdot -}$. If $\mathbf{S_{ox}}^{\cdot -}$ degrades in solution via a homogenous reaction with a half-life much greater than the time taken to complete a scan at rate **X**, (i.e. **X** >> 1/ $\boldsymbol{\tau_{deg}}$), then the ***X*** V/s CV will appear reversible. Alternatively, if a much slower scan rate **Y** is applied which takes a duration to complete a scan that is comparable to the degradation half-life $\boldsymbol{\tau_{deg}}$ or much greater (i.e. **Y** << 1/ $\boldsymbol{\tau_{deg}}$), then the ***X*** V/s CV will appear irreversible. At rate (***Y*** V/s) the majority of unstable $\mathbf{S_{ox}}^{\cdot -}$ generated at the electrode from the forward scan would have degraded through a non-electrochemical reaction in solution, before the reverse electrochemical reaction (reduction) during the return scan can take place. Thus little to no faradaic current will be observable in the reverse scan. At the much faster scan rate (***X*** V/s), the reverse scan takes place before any significant fraction of the unstable oxidised form can take place, thus the current peak on the reverse scan will be comparable in size to the oxidation peak on the forward scan. Chemically reversible systems have the possibility of also being thermodynamically reversible but do not have to be, while chemically irreversible systems cannot be thermodynamically reversible.

Thermodynamic reversibility: A process is thermodynamically reversible if it can be reversed by an infinitesimally small change in the driving force. If a system at state **A** can be driven forward to state **B** by increasing some parameter **X** in the systems surroundings from $\mathbf{X_0}$ to $\mathbf{X_1}$, and, if after reversing the driving force the systems state is returned to **A** along with returning **X** back to $\mathbf{X_0}$, without altering anything else in the surrounding, then the system can be classified as thermodynamically reversible. Regarding a potential scan and thinking about the changing potential as a series of small steps rather than a continuum, for a system to appear thermodynamically reversible, after each potential step, the system must reach equilibrium before the next step. Thus, at one scan rate a process may be thermodynamically reversible but at a much faster scan rate it may be thermodynamically irreversible.

Electrochemical reversibility: If the rate of electron transfer between the electrochemically active species in solution and electrode during the redox reaction is fast (i.e. the thermodynamic barrier is low) then the reaction is classed as electrochemically reversible. Electron transfer reactions that are in between fast and slow, relative to the experiment time scale, can be classed as quasi-reversible. Regarding CV procedures, a quasi-reversible reaction may appear reversible at slow scan rates but give an irreversible characteristic at high scan rates.

Examples & Nomenclature/Symbols: Throughout this chapter various example systems are used to illustrate certain aspects of electrochemistry. The most frequent of which uses a standard three electrode set-up, consisting of a planar working electrode, a counter and reference electrode with a hypothetical, reversible, electrochemically active species in an aqueous system. The only other species the system contains is an electrochemically inert electrolyte at a concentration 1000-fold that of the electrochemically active species. The electrochemically active species is given the symbol **S** and has two possible redox states, oxidised $\mathbf{S_{ox}}$, designated state **A**, and reduced $\mathbf{S_{red}}$, designated state **B** (sometimes written as $\mathbf{B^-}$). The reversible redox reaction with the electrode occurs with the transfer of one electron ($\mathbf{S_{ox} + e^- \rightleftarrows S_{red}} \equiv \mathbf{A + e^- \rightleftarrows B^-}$). In potential energy diagrams, state **A** refers to the combined free energy of the species in state **A** (i.e. the oxidised species $\mathbf{S_{ox}}$) and to the fermi level electron $\mathbf{e^-}$ from the electrode, whilst state **B** refers just to the species in state **B** (i.e. the reduced species $\mathbf{S_{red}}$).

3. Effect of Surfaces on MR-1 EET Mechanisms and soluble Iron as a mediator

3.1 Introduction

Microbial electrochemical systems (MES) interface exoelectrogenic microbes to electrodes, and exploit them for useful applications, such as biosensing, bioremediation, chemical synthesis and energy production.[1, 3, 8, 18, 103] Unfortunately, as mentioned in **chapter 1**, the performance of MES, especially for energy production, is relatively low.[3] The general approach to increasing the performance of MES is to engineer the microbe and/or the electrode surface to increase electron transfer (ET) efficiency. This requires a detailed fundamental understanding of EET and species from the *Geobacter* and *Shewanella* genus have been studied extensively for this purpose.[13-15]

As described in **chapter 1** and summarised in **figure 3.1**, MR-1 has multiple mechanisms for transferring electrons to extracellular insoluble electron acceptors which include direct electron transfer (DET) and mediated electron transfer (DET). Whole cell, (*in vivo*), electrochemical studies of MR-1 have been performed on a variety of electrodes ranging from gold and ITO to carbon based electrodes[14, 49, 104], and a range of potentials have been reported for MET via flavins (between -0.25 and -0.13 V vs SHE)[14, 43] and DET via MtrC/OmcA (between 0 and +0.4 V vs SHE).[14, 40, 48, 104] Potentials assigned to MtrC/OmcA DET *in vivo* are unexpectedly high/positive when compared to the *in vitro* potential ranges of MtrC/OmcA (between -0.4 to 0 V vs SHE) obtained using protein film voltammetry on multiple surfaces (including graphite, SAM modified gold and ITO).[105, 106] The increased potential assigned to MtrC/OmcA DET *in vivo* has been attributed to differences in the micro environment at the microbe/electrode interface.[14]

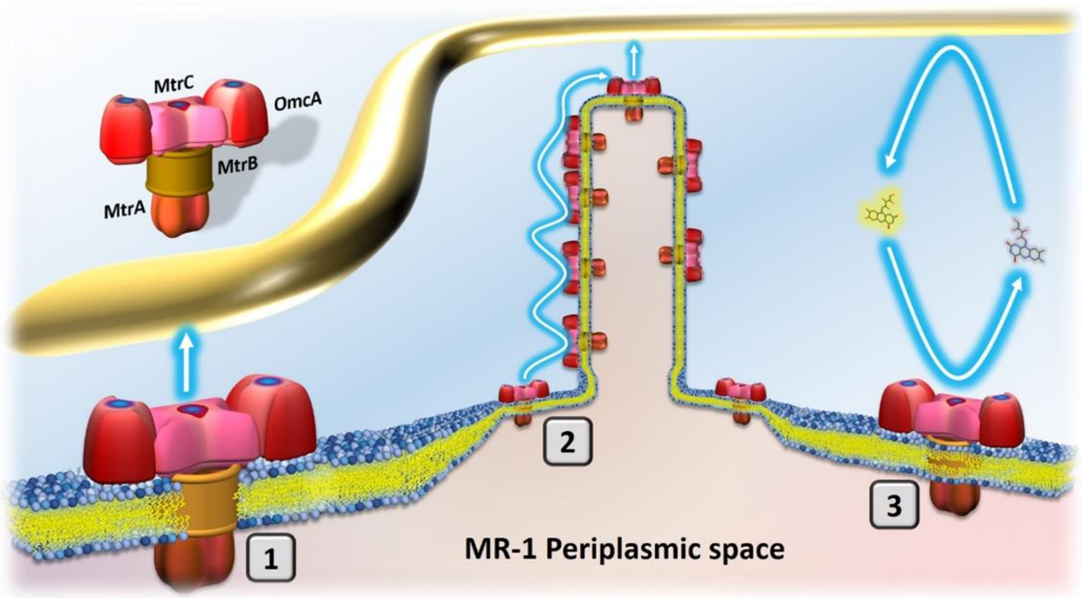

Figure 3.1. Overview of the three proposed mechanisms for MR-1 ET to electrodes. Electrons are passed on to the outer-membrane spanning MtrCAB/OmcA complex. From the MtrCAB/OmcA complex, ET to electrodes can occur directly with or without bound flavins as cofactors (1), by long ranged DET involving 'wires' formed by extrusions of the outer membrane and periplasm (2), or MET by flavins (3).

The relevance of the different EET pathways in MES is under debate with strong arguments for both MET and DET as the dominant pathway.[14, 49, 107] There is also significant variation in the reported redox potentials assigned to DET through MtrC/OmcA as summarised in **Table 3.1**. This variation might be due to the different electrode materials used but little is known about their surface properties and influence on MR-1's interaction with them. Recently, Artyushkova *et al.*[108], modified gold electrodes with different self-assembled monolayers (SAMs) and found that changing the electrode surface properties leads to significant differences in the morphology and current output of the bacterial biofilm. The EET mechanism to the different modified surfaces was not investigated by Artyushkova *et al*. Here, we adapted the approach of Artyushkova *et al* to investigate the effect of surface properties on MR-1 EET mechanisms. Ultra-smooth gold electrodes were modified with SAMs terminated in different functional groups to alter the electrode surface charge. MR-1 was then grown on the SAM modified gold electrodes along with pyrolytic carbon and indium tin oxide (ITO) electrodes and the EET mechanisms were studied with voltammetry.

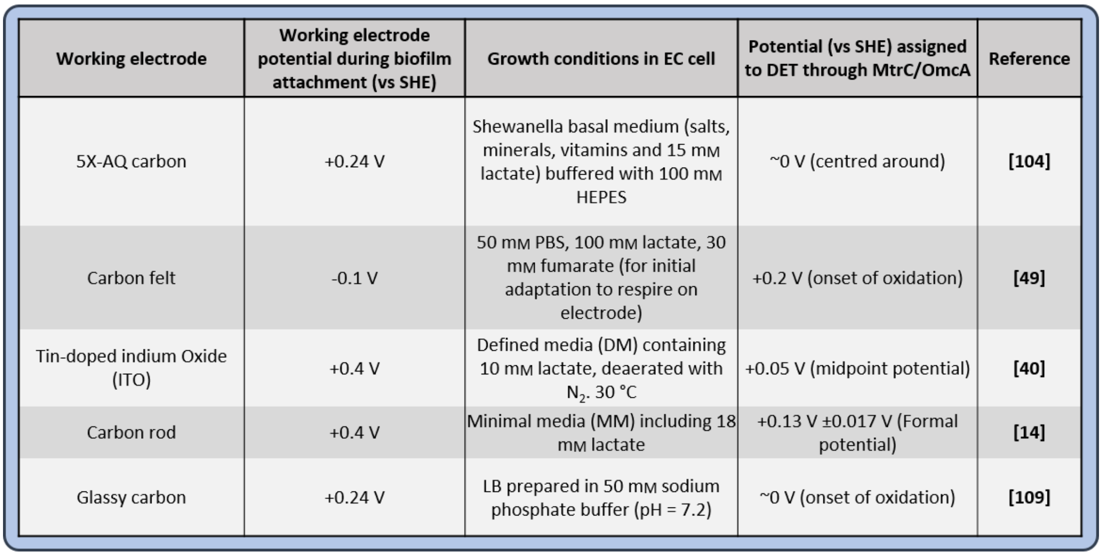

Working electrode	Working electrode potential during biofilm attachment (vs SHE)	Growth conditions in EC cell	Potential (vs SHE) assigned to DET through MtrC/OmcA	Reference
5X-AQ carbon	+0.24 V	Shewanella basal medium (salts, minerals, vitamins and 15 mM lactate) buffered with 100 mM HEPES	~0 V (centred around)	**[104]**
Carbon felt	-0.1 V	50 mM PBS, 100 mM lactate, 30 mM fumarate (for initial adaptation to respire on electrode)	+0.2 V (onset of oxidation)	**[49]**
Tin-doped indium Oxide (ITO)	+0.4 V	Defined media (DM) containing 10 mM lactate, deaerated with N_2. 30 °C	+0.05 V (midpoint potential)	**[40]**
Carbon rod	+0.4 V	Minimal media (MM) including 18 mM lactate	+0.13 V ±0.017 V (Formal potential)	**[14]**
Glassy carbon	+0.24 V	LB prepared in 50 mM sodium phosphate buffer (pH = 7.2)	~0 V (onset of oxidation)	**[109]**

Table 3.1: A sample of the different experimental conditions used in MR-1 EET studies and the corresponding potentials ascribed to MR-1 DET.

3.2 Materials and methods

Cultures and media

All chemicals and materials were obtained from Sigma-Aldrich unless otherwise stated. *S. oneidensis* MR-1 cultures were grown aerobically in LB (30 ^{o}C, 200 rpm, 16 hours) to an $OD_{600nm} > 1$. 1 ml of this culture was used to inoculate 50 ml of LB supplemented with 50 mM lactate and 25 mM fumarate in a 50 ml falcon tube. The tube top was fastened shut and the culture grown overnight (0 rpm, 30 ^{o}C). The bacteria reached a maximum OD_{600nm} of ~0.7 and pH of 6.25-6.30 before growth ceased. The cells were pelleted via centrifugation (3220 g, 15 min) and washed twice with 10 ml MOPS buffer (20 mM MOPS, 30 mM Na_2SO_4, pH 7.4) before re-suspension in 5 ml of MOPS buffer. The washed MR-1 was stored at 4 ^{o}C and used as soon as possible (within 1-2 h) for electrochemical experiments.

Defined media (DM) contained the following ingredients (per litre): 1.5 g of NH_4Cl (Melford), 0.1 g of KCl (BDH laboratory supplies), 0.625 g of Na_2HPO_4 (Melford), 0.213 g of Na_2SO_4, 0.103 g of $CaCl_2$•$2H_2O$ (Fisher Scientific), 0.095 g of $MgCl_2$ (ACROS organics), 1.51 g of PIPES, 2 ml of trace minerals solution and 10 ml of vitamin solution. In addition to this, lactate was added to a concentration of 10 mM. The pH of DM was ~7.4. DM was sterilised by filter sterilisation (0.22 µm).

The trace mineral solution contained (per liter) 1 g of $FeCl_2$•$4H_2O$, 0.5 g of $MnCl_2$•$4H_2O$, 0.3 g of $CoCl_2$•$6H_2O$, 0.2 g of $ZnCl_2$, 0.05 g of Na_2MoO_4•$2H_2O$ (ACROS organics), 0.02 g of H_3BO_3, 0.1 g of $NiSO_4 \bullet 6H_2O$, 0.002 g of $CuCl_2 \bullet 2H_2O$ (ACROS organics), 0.006 g of $Na_2SeO_3 \bullet 5H_2O$, 0.008 g of $Na_2WO_4 \bullet 2H_2O$ (ACROS organics). The vitamin solution contained (per litre) 0.002 g of biotin, 0.002 g of folic acid, 0.001 g of B6 (pyridoxine) HCl, 0.005 g of B1 (thiamine) HCl, 0.005 g of B2 (riboflavin), 0.005 g of nicotinic acid, 0.005 g of pantothenic acid (Santa Cruz Biotechnology), 0.005 g of *p*-aminobenzoic acid, 0.005 g of lipoic acid, 0.2 g choline chloride, and 0.001 g of B12 (cobalamin) crystalline.

Self-assembled monolayer (SAM) modified electrodes

Template-stripped gold (TSG) electrodes were prepared as described previously.[110] To form SAMs, TSG glass slides were incubated in 1 ml H_2O with 1 mM of thiol, either 8-mercapto-1-octanol (8-OH) or a 57:43 mixture of 8-OH and 8-mercaptooctanoic acid (8-COOH). Slides were incubated in the thiol solution at 4 °C for at least 16 h. Prior to use, electrodes were washed with isopropanol before drying under a stream of N_2.

Electrochemistry

In general, for electrochemical experiments, a bespoke glass, single chamber electrochemical cell, housed in a Faraday cage, was used with a standard three-electrode set-up (**figure 3.2**). As the working electrode, TSG (modified with a SAM) or ITO was embedded in a polytetrafluoroethylene (PTFE) holder with a rubber O-ring seal (exposing an electrode area of 0.24 cm^2). The working electrode was placed in the electrochemical cell along with a platinum wire counter electrode and a saturated mercury/mercury sulphate (Hg/Hg_2SO_4) reference electrode (Radiometer analytical, France). All potentials given were converted with respect to a standard hydrogen electrode (SHE), using +651 mV vs SHE for the Hg/Hg_2SO_4 reference electrode. MOPS buffer (20 mM MOPS, 30 mM Na_2SO_4, pH 7.4), continuously purged with Argon, was used as the basal electrolyte solution for all experiments unless stated otherwise.

Prior to experiments the SAM condition was qualitatively assessed using electrochemical impedance spectroscopy (EIS). EIS is an exceptionally sensitive technique capable of detecting the presence of pin hole defects in thin films and as such is used extensively for determining the quality of SAMs [111, 112]. Briefly, the packing density and presence of defects, such as pin hole defects, contribute to the overall impedance of a SAM via effecting the permeability of ions through the SAM (i.e. how leaky the SAM is). In a Bode phase plot, increases in permeability present as significant decreases in the phase angle from 90° during relatively low frequencies (< ~50 Hz). If the phase angle drops markedly below 85°, then the

SAM is determined to be of poor quality and not used in the experiment. Two or three electrodes were made for each experiment, thus if the initial electrode's SAM is of poor quality then it can be swapped for another and the testing repeated.

For a typical experiment, washed MR-1 was added to the electrochemical cell to an OD_{600nm} = 0.45. Sodium lactate was then added from a 200 mM stock solution to a final concentration of 10 mM (acting as the sole electron/carbon source for bacterial respiration). To promote EET to the working electrode, the electrode was poised at +0.25 V (vs SHE). At various time points the interaction of bacteria on the SAM modified electrodes was probed via cyclic voltammetry. Small variations to this general method are detailed, where relevant, in the results section. In some experiments a defined media (DM) was used instead of MOPS buffer as the basal electrolyte solution.

Electrochemical experiments using pyrolytic graphite edge (PGE) electrodes followed the same experimental method as described for TSG electrodes but required a different experimental set-up. A bespoke, two chamber, glass electrochemical cell, housed in a Faraday cage was used with a standard three-electrode set-up. The PGE working electrode (geometrical area ~0.24 cm^2) was inserted, along with a platinum wire counter electrode, into the main chamber and a saturated mercury/mercury sulphate (Hg/Hg_2SO_4) reference electrode was inserted into the side chamber. The two chambers were inter-connected via a narrow glass tube, allowing for the diffusion of electrolytes between the two chambers.

Electrochemical measurements were obtained using an Autolab electrochemical analyzer (Ecochemie, Utrecht, Netherlands) equipped with a PGSTAT 128N potentiostat, SCANGEN and ADC750 modules, and FRA2 frequency analyzer (Ecochemie). CV measurements were routinely carried out by holding the potential at 0 V for 5 s before cycling between +0.4 V to −0.4 V (vs SHE) at a scan rate of 10 or 100 mV/s. All electrochemical experiments reported here were performed at 20 °C.

Supernatant analysis

MR-1 with an OD_{600nm} = 0.25 was incubated for ~22 hours in 2 ml MOPS buffer with 10 mM sodium lactate on a 8OH:8COOH (57:43) mixed SAM modified TSG electrode poised at +0.25 V (SHE). To separate cells from supernatant, contents from the EC cell were centrifuged at 4500 g and filtered through a 0.22 µm polyethersulfone (PES) filter. The filtered supernatant was analysed by voltammetry, using fresh TSG electrodes that were prepared as described above.

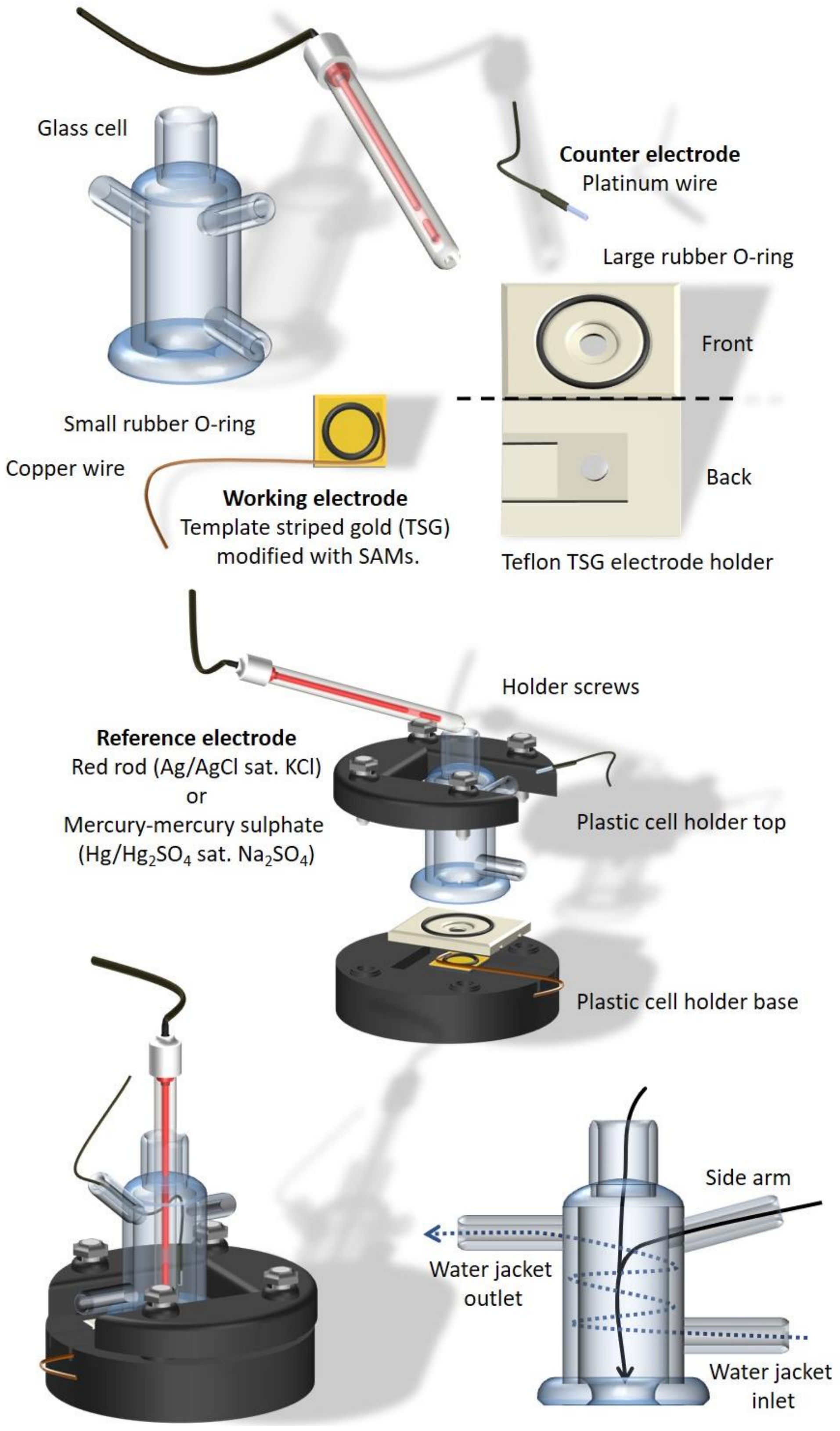

Figure 3.2. Diagram of the bespoke electrochemical cell set up that was employed in the majority of electrochemical experiments for this chapter.

3.3 Results

Rough, predominantly carbon-based, electrodes are generally desired for MES as they exhibit large electrochemical surface areas for microbes to interface with enabling higher currents and thus performance. In contrast, here we have employed ultra-smooth gold electrodes to enable the assembly of well-formed, uniform SAMs with reproducible surface characteristics that result in low capacitances, enabling sensitive voltammetric studies of the EET mechanism. Furthermore, to prevent complications in the analysis due to trace elements and other redox active small molecules, a minimal electrolyte of 20 mM MOPS, 30 mM Na_2SO_4 and 10 mM sodium lactate was used in the majority of experiments.

MR-1 was first grown overnight, anaerobically in LB supplemented with lactate and fumarate. The bacteria from the overnight culture were subsequently washed to remove growth medium and added to the electrochemical cells fitted with gold electrodes modified with SAMs of either pure 8-mecaptooctanol or a mixture of 8-mercaptooctanol and 8-mercapto-octanic acid. Both electrodes have hydrophilic surfaces but the latter's surface also has a negative surface charge. From here on, these electrodes will be designated as neutral and negative electrodes respectively.

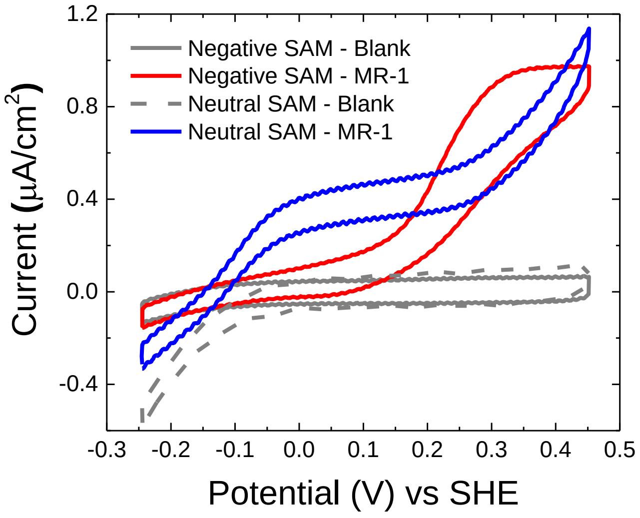

Figure 3.3. Cyclic voltammograms (CV) of MR-1 grown on TSG modified with SAMs of either pure 8-OH (neutral surface, **blue line**) or mixed 8-OH:8-COOH (negative surface, **red line**), after incubation with MR-1 (OD_{600nm} ~ 0.3) in 10 mM lactate, 20 mM MOPS, 30 mM Na_2SO_4, pH 7.4 at +0.25 V for ~ 22 h. Baselines measured before incubation with MR-1 for TSG electrodes modified with SAMs of 8-OH:8-COOH **(grey line)** and 8-OH **(dashed grey line)**. All scans start at the immersion potential E = 0 V with an initial scan direction towards negative potentials. For clarity the initial negative partial scan is not plotted. Scan rate = 0.01 V/s.

To encourage respiration with the electrodes lactate was used as the sole carbon/electron source and the electrodes were poised at +0.25 V. After ~3 hours catalytic waves were observable with onsets that differed significantly between the two electrode surface types (at -0.2 V and +0.1 V for the neutral and negative electrodes, respectively; **Figure 3.3**), confirming that the surface chemistry has a profound effect on the mechanism by which MR-1 transfers electrons to electrodes. When pyrolytic carbon electrodes were used catalytic currents were much lower. However, two oxidative signals were observed with onsets at -0.2 and +0.1 V **(Figure 3.4)**, suggesting each onset is due to a different EET mechanism and that the pyrolytic carbon electrodes can support both. Catalytic currents observed at an onset of about -0.2 V are commonly accepted to originate from an EET mechanism via flavins either as freely diffusing electron mediators or bound as co-factors to outer membrane cytochromes.[14, 43, 49, 113] As expected, when either RF or FMN was added, the catalytic wave retained the same onset potential, but the current increased.

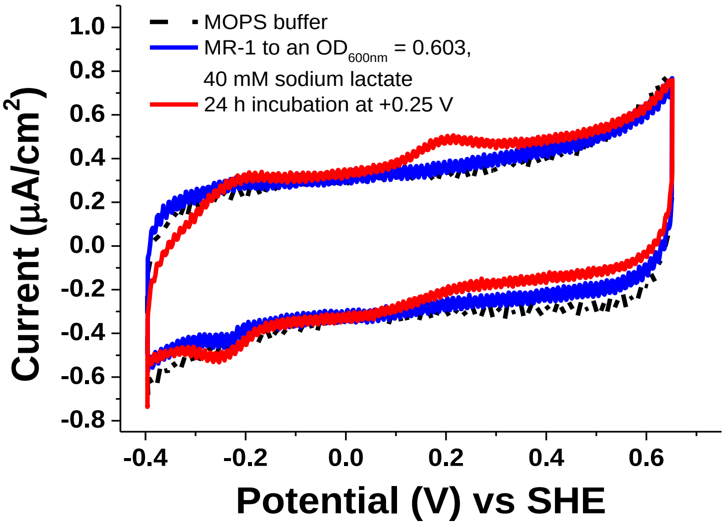

Figure 3.4. Cyclic voltammograms (CV) of a pyrolytic carbon electrode purged with Ar. Baseline of MOPS buffer **(dashed black line)**. Addition of MR-1 to an OD$_{600nm}$ = 0.6 and lactate to a concentration of 40 mM (**blue**). After 24 hour incubation at +0.25 V (SHE) (**red**). All scans start at the immersion potential E = 0 V with an initial scan direction towards negative potentials. For clarity the initial negative partial scan is not plotted. Scan rate = 0.01 V/s.

To determine why different onset potentials were observed with neutral and negative electrodes the electrochemical behaviour of flavin was determined with both electrodes. The reaction of riboflavin on neutral electrodes is reversible, indicating rapid ET, **(Figure 3.5)**, whereas the electron exchange between riboflavin and negative electrodes **(Figure 3.5)** is indicative of a quasi- or irreversible ET reaction. The absence of an efficient ET reaction between flavin and negatively-charged surface electrodes limits a flavin-mediated EET pathway and likely gives rise to the observed prevalence of an alternative EET pathway at higher potentials.

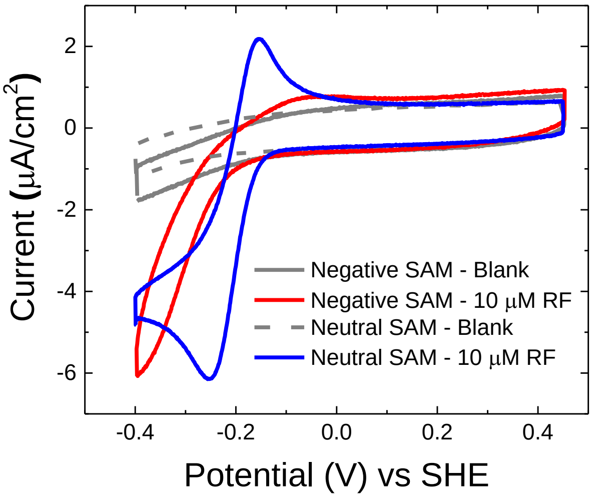

Figure 3.5. Cyclic voltammograms (CV) of 10 µM riboflavin (RF), 20 mM MOPS, 30 mM Na_2SO_4 at pH 7.4 on TSG electrodes modified with SAMs of either pure 8-OH (neutral surface, **blue line**) or mixed 8-OH:8-COOH (negative surface, **red line**). Baselines measured before incubation with riboflavin for TSG electrodes modified with SAMs of 8-OH:8-COOH (**grey line**) and 8-OH (**dashed grey line**). All scans start at the immersion potential E = 0 V with an initial scan direction towards negative potentials. For clarity the initial negative partial scan is not plotted. Scan rate = 0.1 V/s.

Similar, higher potential, onsets have been previously reported in the literature on carbon and ITO electrodes and the EET pathway is proposed to be DET through MtrC/OmcA.[14, 48, 104] However, as discussed above, the redox potentials of MtrC and OmcA do not overlap with the onset potential of the 'high-potential' EET pathway. Therefore further investigation into this alternative EET pathway was carried out. First, it was tested whether the higher potential redox wave can be attributed to a redox compound released by MR-1 into the electrolyte. After growing on a negative electrode for about 23 hours the contents of the electrochemical cell were extracted and the electrolyte separated from bacteria using centrifugation and 0.22 µm filtration. The filtered electrolyte was then analysed using a fresh electrode **(Figure 3.6)**. Notably, the cyclic voltammogram shows redox signals at the same potential as the 'high-potential' EET pathway suggesting that this EET pathway involves a mediator.

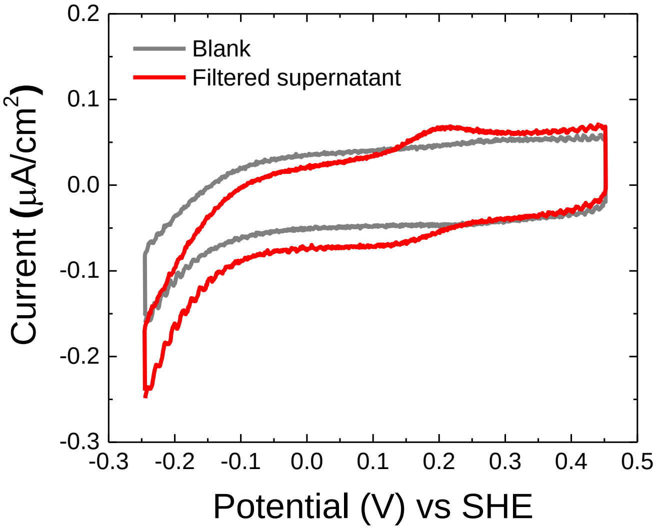

Figure 3.6. Cyclic voltammograms (CV) of the growth medium used to grow MR-1 for ~23 hours in a MES set-up after removing MR-1 by centrifugation and filtration (0.22 μm) using a TSG electrode modified with a mixed SAM of 8-OH:8-COOH (negative surface, **red line**). Baselines measured before incubation with the growth medium (**grey line**). All scans start at the immersion potential E = 0 V with an initial scan direction towards negative potentials. For clarity the initial negative partial scan is not plotted. Scan rate = 0.01 V/s.

In an effort to identify the redox active compound, the filtrate was analysed with LC-MS without success. To test if the redox active compound was a cytochrome the electrolyte was filtered through a 3 kDa cut-off filter. However, the redox active compound passed through the filter suggesting a molecular weight below 3 kDa. By elimination we speculated the redox-active compound was an inorganic compound, most likely iron. Cyclic voltammograms of iron at negative electrodes **(Figure 3.7)** show a reversible ET reaction at the same onset potential as the 'high potential' EET pathway, whilst with neutral surface electrodes **(Figure 3.8)** almost no redox signal is obtained. Importantly, lactate causes a large change in the Fe reduction signal leading to a more reversible CV **(Figure 3.7)**. It should be noted that the reduction potential and voltammetry characteristics of Fe-lactate are remarkably similar to the non-turnover '*in vivo*' signals described in the literature as DET through MtrC/OmcA.[40, 104]

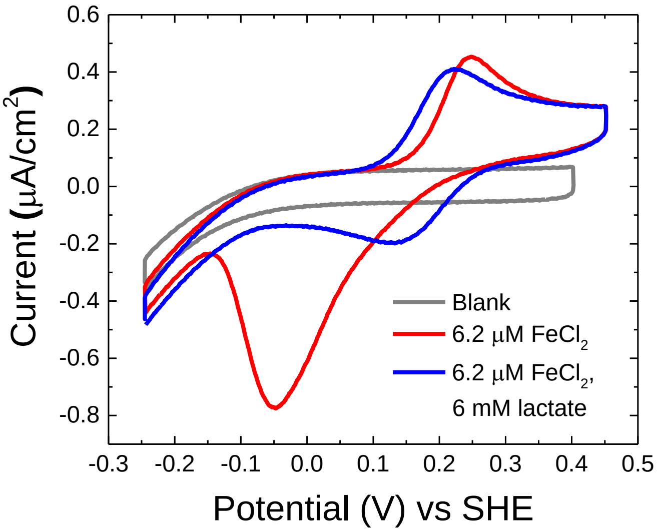

Figure 3.7. Cyclic voltammograms (CV) of 6.2 μM $FeCl_2$ in 20 mM MOPS, 30 mM Na_2SO_4, pH 7.4 on a TSG electrode modified with a mixed SAM of 8-OH:8-COOH (negative surface) before (**red line**) and after addition of 6 mM lactate (**blue line**). Baselines measured before addition of $FeCl_2$ (**grey line**). All scans start at the immersion potential E = 0 V with an initial scan direction towards negative potentials. For clarity the initial negative partial scan is not plotted. Scan rate = 0.01 V/s.

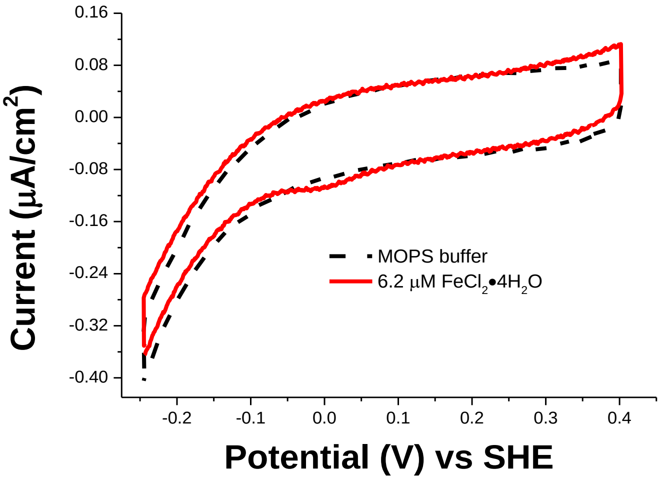

Figure 3.8. Cyclic voltammograms (CV) of a 8-OH (neutral surface) pure SAM modified TSG electrode. Baseline of MOPS buffer **(dashed black line)**. Addition of $FeCl_2$•4H2O to a concentration of 6.2 μM **(red lines)**. All scans start at the immersion potential E = 0 V with an initial scan direction towards negative potentials. For clarity the initial negative partial scan is not plotted. Scan rate = 0.01 V/s.

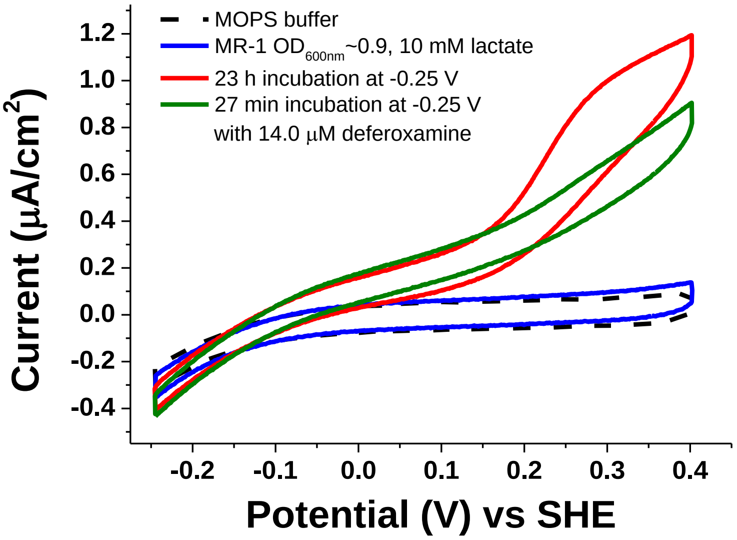

Figure 3.9. Cyclic voltammograms (CV) of MR-1 (OD_{600nm} = 0.55) in 10 mM lactate, 20 mM MOPS, 30 mM Na_2SO_4, pH 7.4, measured directly after addition of MR-1 (**blue line**), after a ~23 hour incubation at +0.25 V (SHE, **red line**) and after addition of 14 μM deferoxamine and a further 30 min at 0.25 V (**green line**) using a TSG electrode modified with a mixed SAM of 8-OH:8-COOH (negative surface). Baselines measured before addition of MR-1 (**dashed line**). All scans start at the immersion potential E = 0 V. Scan rate = 0.01 V/s.

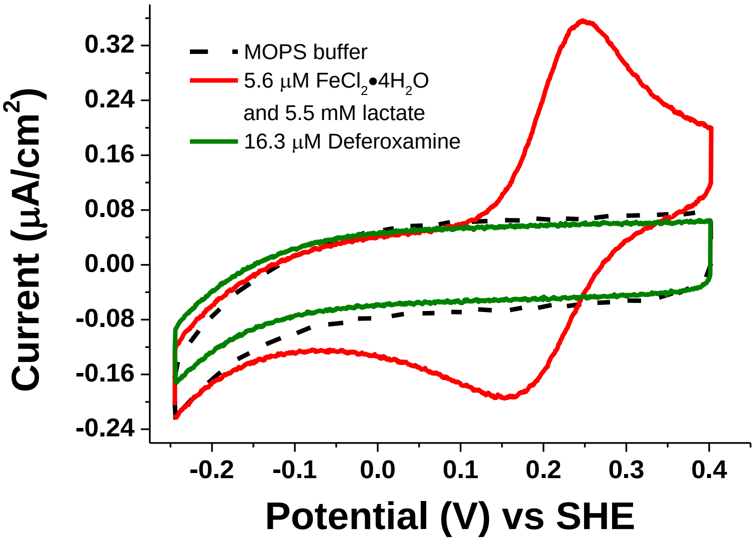

Figure 3.10. Cyclic voltammograms (CV) of a 8-OH:8-COOH (negative surface) mixed SAM modified TSG electrode. Baseline of MOPS buffer (**dashed black line**). Addition of $FeCl_2$•4H2O to a concentration of 5.6 μM and lactate to a concentration of 5.5 mM (**red**). After addition of deferoxamine to a concentration of 16.3 μM (**green**). All scans start at the immersion potential E = 0 V with an initial scan direction towards negative potentials. For clarity the initial negative partial scan is not plotted. Scan rate = 0.01 V/s.

To further confirm whether the high-potential EET pathway observed on negative electrodes originates from iron-based MET, deferoxamine was added. Deferoxamine is a siderophore that strongly chelates free iron but is unable to dissociate iron from cytochromes, such as MtrC and OmcA. Indeed, the addition of deferoxamine almost obliterates the high-potential EET pathway, whilst leaving the smaller catalytic wave caused by flavin MET unaffected **(Figure 3.9)**. A control CV of the Fe-deferoxamine complex confirms that this complex does not give reversible voltammetry signals on negatively-charged electrodes **(Figure 3.10)**. It is important to note that deferoxamine only complexes Fe(III) but under aerobic or microaerobic conditions facilitates 'auto-oxidation' of Fe(II) to Fe(III) as it influences the Fe(II)/Fe(III) redox equilibrium.[114] The results reported here were recorded under micro-aerobic conditions. Under strict anaerobic conditions, (O_2 < 0.1 ppm using a glove box), it was observed that deferoxamine did not significantly affect the high-potential EET pathway which we attribute to the reducing conditions, decreasing the ability of deferoxamine to complex iron. Importantly, under these strict anaerobic conditions, addition of 90 µM EDTA was still able to obliterate the high potential high-potential EET pathway.

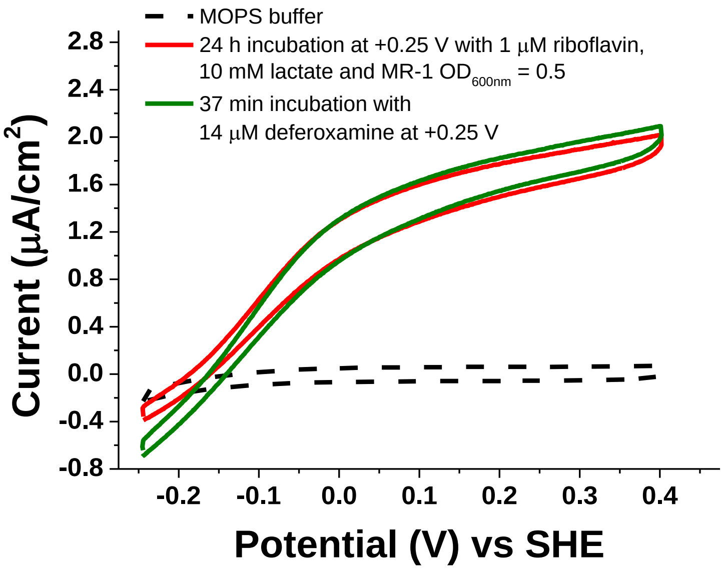

Figure 3.11. Cyclic voltammograms (CV) of an 8-OH (neutral surface) pure SAM modified TSG electrode. Baseline of MOPS buffer **(dashed black line)**. After 24 hours incubation at +0.25 V (SHE) with 1 µM RF, 10 mM lactate and MR-1 at an OD_{600nm} = 0.45 **(red)**. After addition of deferoxamine to a concentration of 16 µM and a further 30 min incubation at +0.25 V (SHE) **(dark green)**. All scans start at the immersion potential E = 0 V with an initial scan direction towards negative potentials. For clarity the initial negative partial scan is not plotted. Scan rate = 0.01 V/s.

To rule out the possibility that deferoxamine is toxic to MR-1 an experiment was performed in which deferoxamine was added to MR-1 grown on a neutral SAM with exogenous RF **(figure 3.11)**. No effect was observed upon deferoxamine addition nor was an effect observed upon prolonged incubation (> 30 min), confirming that deferoxamine, at the concentrations used here, has no detrimental effect on MR-1.

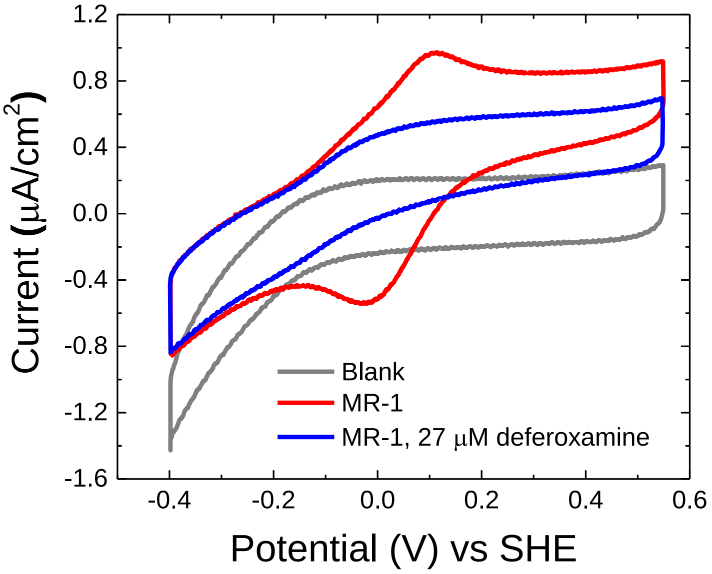

Figure 3.12. Cyclic voltammograms (CV) with an ITO electrode after incubation with MR-1 at +0.4 V (SHE) for 21 hours in DM medium before (**red line**) and after (**blue line**) addition of 27 μM deferoxamine and a further 30 min incubation at +0.4 V (vs SHE). Baselines measured before addition of MR-1 (**grey line**). All scans start at the immersion potential E = 0 V with an initial scan direction towards negative potentials. For clarity the initial negative partial scan is not plotted. Scan rate = 0.01 V/s.

SAM modified gold electrodes are not typically used in MES nor are supplemented MOPS buffers as growth medium. For this reason, experiments were repeated using the more typical electrode materials, pyrolytic carbon and indium-tin oxide (ITO), along with DM as growth medium. During incubation with MR-1 cyclic voltammetry was performed to examine the bacterial EET. On ITO electrodes, a high-potential signal was observed with an apparent midpoint potential of ~+50 mV alongside a catalytic wave corresponding to flavin MET. This high-potential signal was again confirmed to originate from soluble iron by the addition of deferoxamine **(Figure 3.12)**. For a better comparison between ITO and SAM modified gold electrodes experiments were also performed with MOPS buffer supplemented with lactate and a holding potential of +0.25 V **(Figure 3.13)**. Under these conditions the apparent midpoint potential of soluble iron on ITO was ~+130 mV. Interestingly, the redox potential of high potential peaks/signals on ITO electrodes **(Figure 3.12)** is shifted in the negative direction with respect to negative gold electrodes **(Figure 3.9 and 3.10)** and pyrolytic carbon electrodes **(Figure 3.4)**. Redox potentials of soluble iron are expected to depend on the electrolyte composition as many anions have the propensity to coordinate to iron. Most media used for MR-1 contains lactate which will coordinate to iron but additional factors, such as pH, will also influence the reduction potential. Furthermore, the surface properties of the electrode material will influence the interfacial ET kinetics, which can alter the onset of a catalytic wave.

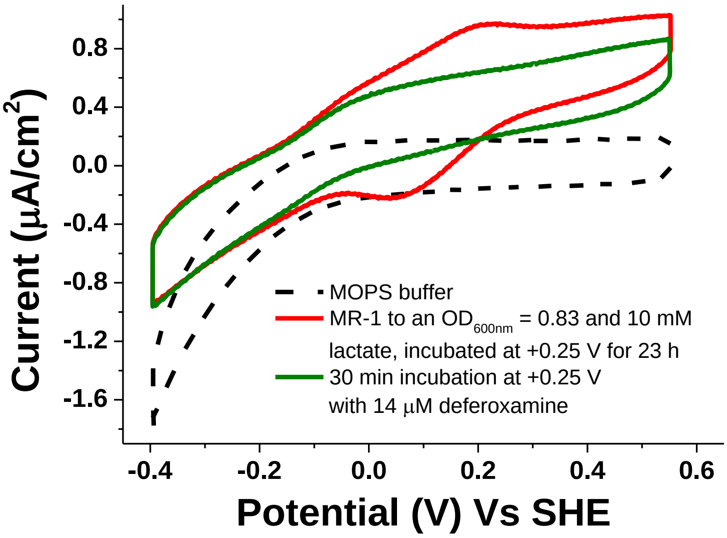

Figure 3.13. Cyclic voltammograms (CV) of an ITO electrode. Baseline of MOPS buffer **(dashed black line)**. After 23 h incubation at +0.25 V (SHE) with MR-1 and 10 mM lactate **(red)**. After addition of deferoxamine to a concentration of 14 μM and 30 min further incubation at +0.25 V (SHE) **(dark green)**. All scans start at the immersion potential E = 0 V with an initial scan direction towards negative potentials. For clarity the initial negative partial scan is not plotted. Scan rate = 0.01 V/s.

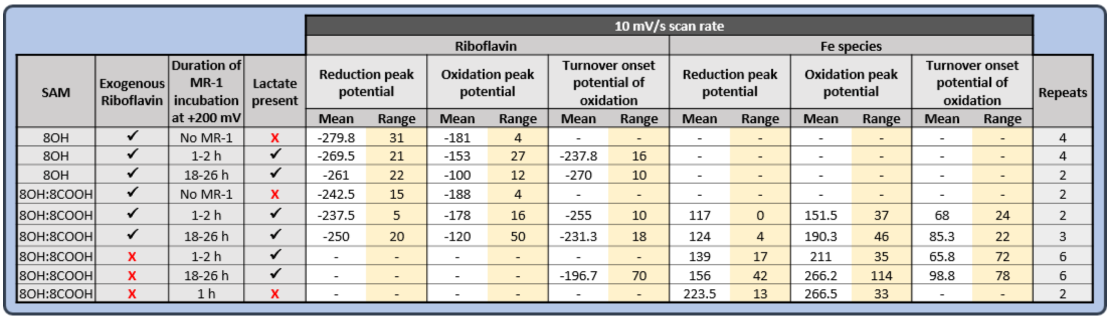

				10 mV/s scan rate												
				Riboflavin						Fe species						
SAM	Exogenous Riboflavin	Duration of MR-1 incubation at +200 mV	Lactate present	Reduction peak potential		Oxidation peak potential		Turnover onset potential of oxidation		Reduction peak potential		Oxidation peak potential		Turnover onset potential of oxidation		Repeats
				Mean	Range	Mean	Range	Mean	Range	Mean	Range	Mean	Range	Mean	Range	
8OH	✓	No MR-1	✗	-279.8	31	-181	4	-	-	-	-	-	-	-	-	4
8OH	✓	1-2 h	✓	-269.5	21	-153	27	-237.8	16	-	-	-	-	-	-	4
8OH	✓	18-26 h	✓	-261	22	-100	12	-270	10	-	-	-	-	-	-	2
8OH:8COOH	✓	No MR-1	✗	-242.5	15	-188	4	-	-	-	-	-	-	-	-	2
8OH:8COOH	✓	1-2 h	✓	-237.5	5	-178	16	-255	10	117	0	151.5	37	68	24	2
8OH:8COOH	✓	18-26 h	✓	-250	20	-120	50	-231.3	18	124	4	190.3	46	85.3	22	3
8OH:8COOH	✗	1-2 h	✓	-	-	-	-	-	-	139	17	211	35	65.8	72	6
8OH:8COOH	✗	18-26 h	✓	-	-	-	-	-196.7	70	156	42	266.2	114	98.8	78	6
8OH:8COOH	✗	1 h	✗	-	-	-	-	-	-	223.5	13	266.5	33	-	-	2

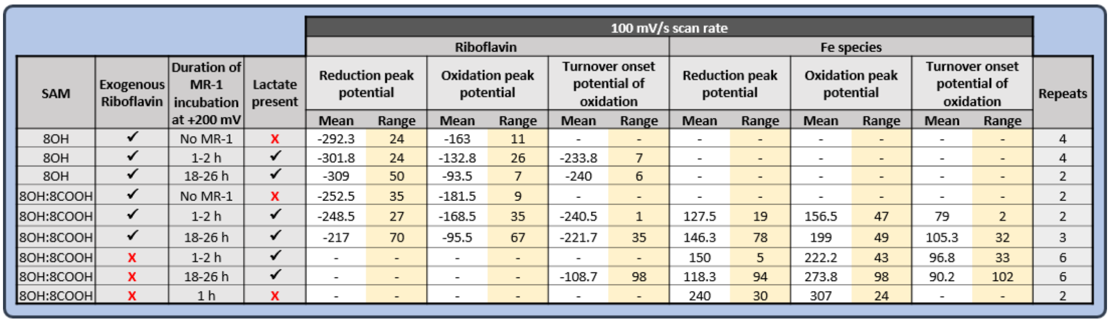

				100 mV/s scan rate												
				Riboflavin						Fe species						
SAM	Exogenous Riboflavin	Duration of MR-1 incubation at +200 mV	Lactate present	Reduction peak potential		Oxidation peak potential		Turnover onset potential of oxidation		Reduction peak potential		Oxidation peak potential		Turnover onset potential of oxidation		Repeats
				Mean	Range	Mean	Range	Mean	Range	Mean	Range	Mean	Range	Mean	Range	
8OH	✓	No MR-1	✗	-292.3	24	-163	11	-	-	-	-	-	-	-	-	4
8OH	✓	1-2 h	✓	-301.8	24	-132.8	26	-233.8	7	-	-	-	-	-	-	4
8OH	✓	18-26 h	✓	-309	50	-93.5	7	-240	6	-	-	-	-	-	-	2
8OH:8COOH	✓	No MR-1	✗	-252.5	35	-181.5	9	-	-	-	-	-	-	-	-	2
8OH:8COOH	✓	1-2 h	✓	-248.5	27	-168.5	35	-240.5	1	127.5	19	156.5	47	79	2	2
8OH:8COOH	✓	18-26 h	✓	-217	70	-95.5	67	-221.7	35	146.3	78	199	49	105.3	32	3
8OH:8COOH	✗	1-2 h	✓	-	-	-	-	-	-	150	5	222.2	43	96.8	33	6
8OH:8COOH	✗	18-26 h	✓	-	-	-	-	-108.7	98	118.3	94	273.8	98	90.2	102	6
8OH:8COOH	✗	1 h	✗	-	-	-	-	-	-	240	30	307	24	-	-	2

Tables 3.2. Tables comparing redox peak potentials (vs SHE) associated with redox signals assigned to iron (Fe) species and riboflavin (RF) from 10 mV/s (**TOP**) and 100 mV/s (**BOTTOM**) cyclic voltammograms. In addition to peak potentials catalytic wave onset potentials are also displayed where applicable. Displayed alongside the mean potentials are the maximum variations between repeats given as a range. Included experiments are limited to those carried out using SAM modified TSG working electrodes with SAMs formed using either 1 mM 100% 8-mercapto-1-octanol (8OH) or a 1 mM 57:43 mix of 8-mercapto-1-octanol: 8-mercapto-1-octanoic acid (8OH:8COOH). The number of repeats used to calculate the means for each type of experiment are displayed at the end of each table. In the case of columns labelled "exogenous riboflavin" and "lactate present" black ticks indicating the addition/presence of riboflavin/lactate whilst red crosses indicating their absence.

3.4 Discussion

Artyushkova *et al* previously performed a detailed study in which the influence of the surface chemistry of SAM-modified gold electrodes on the biofilm formation by MR-1 was investigated with electrochemistry, confocal and electron microscopy.[108] Positively charged, (amine-terminated SAMs), and hydrophilic surfaces (hydroxy-terminated SAMs) were found to present the most uniform biofilms. Importantly, as observed here, also negatively charged surfaces (carboxylic-acid terminated SAMs) were found to support biofilm formation, although the films were more heterogeneous. In contrast to the work of Artyushkova *et al.*, who used SAMs of pure mercaptoundecanoic acid to create negatively charged surfaces, here a mixture of 8-mercapto-1-octanol and 8-mercaptooctanoic acid (57:43 ratio) was used.

EET of MR-1 on hydroxy-terminated SAMs (neutral surface electrodes) is dominated by MET with a reversible ET reaction between electrode and flavin. In contrast, on carboxylic acid terminated SAMs (negatively charged surface electrodes) ET from flavin to electrodes becomes “sluggish” with a quasi irreversible ET behaviour. On these electrodes a second alternative EET pathway becomes apparent at higher potential. Here, we have shown that this high-potential pathway is mediated by iron in solution. It is well known that MR-1 can use iron as a terminal electron acceptor[115] and that iron (e.g. ferricyanide) can mediate ET from bacteria to electrode.[116] Importantly, however, catalytic waves and redox signals similar to the ones reported here have previously been ascribed to DET through MtrC/OmcA,[14, 48, 104] but this assignment needs to be re-evaluated in light of the data presented here.

One principle reason for assigning the redox signals between 0 and 0.2 V to outer membrane cytochromes originates from NO-ligation experiments.[40] When NO was introduced to a biofilm of MR-1 grown on an ITO electrode the signal at +50 mV disappeared and a new signal at +650 mV was observed. It was inferred that NO ligates with the haems of outer membrane cytochromes, causing a shift in their redox potential. However, this same result would also be consistent with the fact that NO will ligate ‘free’ iron in solution, raising the redox potential of the iron complexes.

The question remains what the source is of the extracellular iron. The medium in the electrochemical experiments contained only buffer and lactate and therefore can be excluded as a source. It is also unlikely that significant concentrations of soluble iron were transferred when adding MR-1 to the electrochemical cells since the MR-1 was washed twice in buffer prior to transfer. Furthermore, if iron was transferred with MR-1, it would have been immediately observable in the CV. Typically, the catalytic wave or non-turn-over redox signals were not observed until at least one hour’s incubation with MR-1. We therefore propose that iron is released from MR-1, either via active release (as is thought to be the case for flavins) or as a result of cell lysis. We propose that it is unlikely that MR-1 actively releases soluble iron since iron is an essential trace nutrient for MR-1. The most likely cause of soluble iron accumulation is therefore cell lysis where iron could get released from, for instance, iron storage proteins[117] into the electrolyte.

Although we cannot exclude DET as an EET pathway for MR-1 we propose that the “alternative” high-potential signals are due to iron mediated ET between MR-1 and the electrode. We thus recommend that iron chelators, such as deferoxamine, should be used to confirm or disprove DET mechanisms in future characterisations of MES.

The absence of clearly distinguishable redox signals that can be ascribed to DET might raise the question as to whether the extensive use of MR-1 as a model organism for EET in MES is appropriate. However, it has been shown that MR-1 is capable of significant DET to certain surfaces in its natural habitat such as haematite.[118, 119] There has recently been substantial effort directed towards novel electrode materials[120, 121] and surface modifications of established electrode materials.[122, 123] New materials could result in more suitable surfaces for DET with MR-1. DET is generally more desirable than MET in MES even if the microbe produces its own redox mediators like flavins as, in certain applications, the electrolyte in MES is frequently or continuously replaced. This would lead to the constant loss of mediator impairing the electrochemical interaction between electrode and microbes.

4. Flavin Mediated Energy taxis towards Electrodes

4.1 Background

4.1.1 MR-1 Taxis and its Significance

As mentioned in **chapter 1**, the poor performance of MFCs has prevented their adoption as an alternative renewable energy producer. Much of the research into MR-1 has been focused on understanding and enhancing the EET processes for the development of improved MES. The EET is essential for MESs but it is not the only factor to determine the performance of MES. MES using bacteria capable of forming thick and stable biofilms on the surface of electrodes are more likely to be driven by DET than bacteria that exist predominantly in a planktonic state and do not form biofilms or form thin and sparsely distributed biofilms where MET is more prevalent. As discussed previously, DET is generally preferred over MET for more efficient EET.

Geobacter sp, are capable of forming thick and stable biofilms on electrodes (typically with full electrode coverage, 20-45 µm thick) [124-126] and achieve relatively high maximum current densities compared to other EET organisms. The dominant mechanism used by these bacteria is DET. In contrast to Geobacter sp, MR-1 forms relatively insubstantial, loosely bound biofilms (typically with only partial heterogeneous electrode coverage, 1-16 µm thick) [126-129]. It is therefore not surprising that Geobacter sp generally perform better within MFC compared to MR-1. The increased current density achieved by Geobacter sp can be related back to having well-formed biofilms on electrodes that help to increase EET through DET.

If MR-1 could form more substantial biofilms at the electrode interface, it would likely lead to an increase in contribution from DET towards overall EET resulting in increased currents and thus enhance performance in MFC. There have been some encouraging results from recent efforts to improve MR-1 biofilm quality either through engineering electrode materials to increase biocompatibility with enhanced electrode-cytochrome connectivity and denser cell coverage [130] or engineering the microbes themselves to enhance their biofilm forming capabilities [126]. For example, Liu *et al* [126] over expressed YdeH, a diguanylate cyclase, which catalyses the biosynthesis of bis-(30'-50')-cyclic dimeric guanosine monophosphate (c-di-GMP) from guanosine triphosphate. High levels of c-di-GMP promotes the expression of adhesive matrix components which in turn enhance bacterial biofilm formation. Compared to WT MR-1, the strain in which c-di-GMP was over expressed, formed better biofilms with a significantly increased biomass and ~2.8 fold increase in maximum power density [126].

Prior to the formation of biofilms on electrodes bacteria must first locate, migrate towards and then colonise the electrode surface. Understanding the steps involved in MR-1 migration towards insoluble electron acceptors would undoubtedly be beneficial for designing improved MES with better efficiency by providing an environment conducive to MR-1 migration towards and colonisation of the electrode. Since the discovery of MR-1 from Lake Oneida in 1988, relatively little has been reported specifically on the topic of MR-1 taxis towards electrode surfaces although there has been numerous reports focussing on MR-1's interaction with insoluble metal oxides and the role of MR-1 in cycling transition metals within the environment [131]. It is evident, MR-1 did not evolve the ability to locate man-made electrodes and subsequently utilise them for respiration. The electrode respiring phenotype is a consequence of developing the apparatus for non-specific respiration of insoluble metal oxides.

Details of mechanisms employed by MR-1 for taxis towards metal oxides will therefore have relevance for electrode taxis and vice versa. As highlighted below, taxis towards soluble electron acceptors may also share mechanistic aspects with taxis to insoluble electron acceptors. It is therefore useful to understand the details of MR-1 electron acceptor taxis in general. With regards to the literature concerning MR-1 EA taxis, a series of reports over the past two decades [77, 81-84, 132, 133] has provided some interesting findings with compelling evidence regarding different taxis mechanisms, towards electron acceptors.

4.1.2 MR-1 Electron Acceptor Taxis

In general, bacteria achieve migration towards points of interest via chemotaxis and energy taxis. Energy taxis and chemotaxis differ predominantly in their respective sensory mechanisms, as discussed in **chapter 2**. Briefly, energy taxis employs a generic sensor for a metabolic indicator, for example the ΔpH or $\Delta\psi$ component of the proton motive force (pmf), whereas chemotaxis uses sensors for specific molecule e.g. a carbon source or electron acceptor [62, 63]. Both chemotaxis and energy taxis are generally studied using equipment, that apart from a few exceptions has not changed significantly in almost 50 years since Alder *et al* developed the agar plate and capillary techniques that are still widely used today.

In aquatic systems MR-1 is found concentrated in and around pockets containing high concentrations of electron acceptors, such as found in sediments [81, 84], in an otherwise electron acceptor limited environment. Steep redox gradients exist at the interface of these pockets which MR-1 can migrate up either directly or indirectly to stay near to locations with abundant electron acceptors. Energy taxis is an appealing strategy for MR-1 taxis towards pockets of electron acceptors, due to the wide array of electron acceptors MR-1 is capable of respiring on, some of which are reduced non-specifically via the outer membrane cytochromes. An alternative option is that MR-1 may sense changes in redox conditions directly, possibly with a sensor, comparable to the Aerotaxis receptor (Aer) of *E*.coli, with a Flavin adenine dinucleotide (FAD) associated, 'velcro like' Per-Arnt-Sim (PAS) domain, for detecting redox status [77]. Importantly, in the case of insoluble electron acceptors (including electrodes in MES), there is not necessarily any gradient of soluble molecules to allow either chemotaxis or energy taxis. Therefore MR-1 must possess other means for locating these electron acceptors.

A large proportion of studies into MR-1 taxis towards electron acceptors have used agar plate assays, namely chemical in plug/well and swarm plate, as their main technique [77, 80, 81, 83, 84]. Recently, as described in **Chapter 2**, issues have been encountered with the traditional techniques, including the capillary assay and agar plate based techniques. The previously identified issues with the standard tools for probing chemotaxis has encouraged researchers to turn to other more direct techniques like video microscopy with cell tracking [132-134]. This technique can monitor both population responses and single cell behaviours in a quantitative manner making it a versatile technique. Once bacterial positions have been located in the image stack making up the video bacterial traces are obtained either manually, which is inherently tedious and time consuming, or by computational methods, usually in the form of purpose built in-house programs assembled in MATLAB or similar environments. Manual tracking is typically more accurate but not practical for large numbers of frames and/or bacteria. The computational method, although fast and convenient can suffer from artefacts, especially if the average path length of the bacteria between frames is close to or longer than the average distance between individual bacterial cells (I.e. when the cells are closely pact +/or moving rapidly).

The use of electrodes to couple electrochemistry with video microscopy allows for more control over tracking experiments and can provide valuable insight into MR-1 taxis. With this type of set up, MR-1 attachment or swimming behaviour can be correlated with the electron transfer rate to insoluble electron acceptors in real time. If a soluble redox mediator was to be investigated, the redox state of the mediator can be rapidly altered close to the electrode allowing for a clear distinction between MR-1 responses to the oxidised and reduced forms of a chemical, or even form well defined redox gradients with the right set-up [135]. Harris et al [132, 133] noticed that MR-1 demonstrated a relaxation between switching potentials. This effect would have been difficult to pick up without having the ability to control and rapidly alter the redox state of a surface.

Inspired by the work of Harris *et al,* an experimental platform was developed and a series of experiments carried out in order to specifically look at the effects riboflavin has on MR-1 behaviour around electrodes relative to the applied potentials. The set-up was designed with the aim to obtain high quality electrochemical measurements and microscopy videos. By extracting bacterial trajectories from the videos, individual and population level behaviours of MR-1 can be analysed.

4.2 Experimental platform design

4.2.1 Capillary electrochemical cell

The electrochemical capillary cell used for MR-1 taxis experiments was originally developed, based on the custom capillary cell constructed by Neilson *et al* [132, 133]. The final capillary cell, used in all the reported taxis experiments here, was produced after numerous design cycles. Trial experiments using each successive capillary cell iteration informed the re-designing of the following iteration. A summary of the different capillary cells constructed and trialled is displayed in **figure 4.1**. In summary, **iteration 1** only used two electrodes with no dedicated reference electrode and prevented one from poising the working electrode at a known or reproducible potential. Additional issues related to leaking from sealed openings and unreliable electrical connections with the fragile wires. **Iterations 2** and **3** largely solved the aforementioned issues, including the lack of reference electrode, with the addition of a reservoir allowing inclusion of a conventional red rod or saturated mercury sulphate reference electrode. **Iteration 3** is a variation of **2** which uses a custom base to enable the use of short distance/high NA objectives including oil emersion. Oxygen diffusion into the capillary cell through the reservoir was the main issue with both **2** and **3**. In the presence of oxygen, MR-1 will preferentially travel up the oxygen gradient opposed to any other electron acceptor [81], and thus its presence is intolerable when studying the potential effect of riboflavin as a mediator for electron acceptor taxis. **Iteration 4** was designed around a commercial microfluidic chamber and incorporated templated gold working electrodes, in replacement of the gold wire. The small compartment for inserting counter electrode and standard reference electrode was sealed using a modified cap and silicon O-ring. From the analysis of trial microscopy videos, using **iteration 4**, in addition to responding to applied potentials at the working electrode MR-1 had a strong tactic response towards the edges of the device. Therefore either a small amount of oxygen was diffusing in from the edges, through the adhesive between glass coverslip and plastic top piece, or the adhesive contains substance(s) that act as chemoattractant for MR-1. In either case this would complicate the interpretation of any results from the set-up. **Iteration 5** resembles **Iteration 1** except for the addition of a separate reference wire, inserted along the side of the counter wire, separated by a small inner capillary (for details of the full set-up, refer to materials and methods). **Iteration 5** performed satisfactorily and produced reproducible results, although variations in overall bacterial motility was high between experiments. The downside to **Iteration 5** is manifested as an awkward and fiddly set-up, particularly regarding the capillary end in which must contain 2 wires and an inner capillary tube.

Leaking of sample suspension from the capillary, through the openings at either end, was a major cause of the high failure rate in setting up a workable capillary cell. The leaking originates from the wettability of the glass slides, to which the capillaries are fixed. The un-treated glass slides wet easily and, once the area around the capillary mouth becomes wet, capillary forces exerted by the narrow gap existing underneath the capillary accelerates the loss of liquid from the main capillary tube. Once flow of liquid out of the capillary was established and the glass surface around the opening wetted, any attempt to seal the openings with silicone grease becomes futile. By pre-treating the glass slides with a hydrophobic coating (Sigmacote) before use wetting was greatly reduced, and leaking issues became practically non-existent.

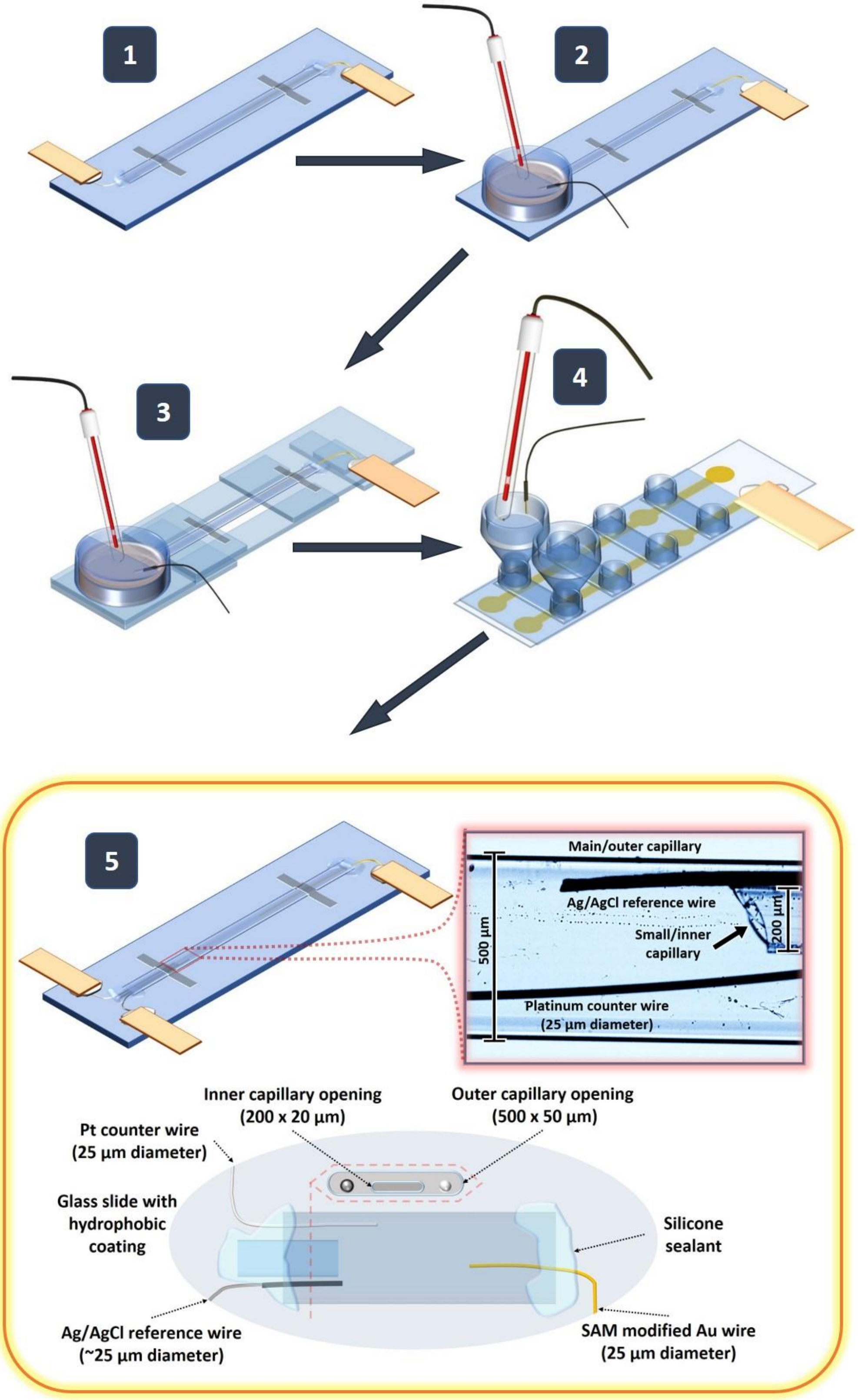

Figure 4.1. Cartoon schematics of the final electrochemical capillary cell used for video microscopy cell tracking experiments, along with cartoons of the previous capillary cell iterations used in trial experiments during the development stage. Capillary cell versions/iterations are numbered one to five in chronological order.

4.2.2 Sample preparation

Preparation of bacteria prior to use in capillary cell experiments originally involved a series of washes using centrifugation (3220 g, 15 min) to separate bacteria from culture media. After washing the final pellet was either re-suspended in lactate supplemented MOPS buffer with or without riboflavin or minimal media. Once the capillary cell was set up with the washed bacteria loaded initial observations (30 min after sealing the capillary) showed little motility of the bacteria, throughout the capillary. Over the following 5 hours of periodic videos, using the applied potential regimes described in materials and methods, only diminutive change was observed. Consequently for most experiments too few motile bacteria were present to obtain any meaningful results from video processing. During trials in which bacterial samples were diluted 5-fold directly from culture with the same buffers as mentioned, without any centrifugation and washing, a significantly higher proportion of motile MR-1 in the capillary cell was observed consistently and at a level suitable for video processing.

The possibility for a detrimental effect on motility incurred through the washing procedure was briefly explored. It is well documented in the literature [136-138] that centrifugation can both damage bacterial structures, particularly those on the outer surface, and reduce cell viability. Damage to the bacteria is not just determined by the centrifugal force applied although it is an important factor. Container geometry and bacterial properties (determined by species/strain and growth phase) [136], together with the centrifugal force determines the damage caused by centrifugation.

To assess whether centrifugation was having a significant effect on bacterial motility three different centrifugation centrifugal forces were compared (1,000, 5,000, 10,000 g) along with a non-centrifuged control. The experiment was performed twice, each with MR-1 initially grown from different starting colonies.

From the three centrifuged samples almost no motile cells were observed in the main body of the drop whilst at the border of the drops (liquid air interface) a high proportion of highly motile cells was observed. No significant difference or trend was seen between the different centrifugation speeds. The un-centrifuged control (still in original culture medium) gave a similar result to the three centrifuged samples at the interfacial region (high oxygen) with highly motile cells. A notable difference was observed within the main body of the control drop where there was a higher proportion of motile cells compared to the centrifuged samples although, in absolute terms, the motility was much lower relative to the edges where most of the cells had migrated. This experiment was repeated with no significant difference in results.

As there was no observable difference between 1000 g and 10 000 g, with a high proportion of motile cells at the air interface in both samples, it would suggest that centrifugation at 3220 g is unlikely to be the cause of low motility in the capillary observed after the washing steps. The fact that the un-centrifuged sample had motile cells in the middle of the drop (lower O_2 concentration) could be due to the buffer/media that the cells were suspended in. To assess the impact on MR-1 motility from re-suspension in different media/buffers MR-1 was centrifuged at low speed and re-suspended in different buffers/media (as described in materials and methods), before evaluating motility by the same method as described for above. MR-1 resuspended in either minimal media or MOPS buffer supplemented with lactate and riboflavin displayed motility confined only to areas close to the liquid air interface. In contrast, samples re-suspended in LB or MOPS buffer, supplemented with lactate and fumarate, had a contingent of swimmers throughout with a higher proportion of swimmers in the supplemented LB relative to the supplemented MOPS buffer. Results from inquiries into both centrifuge induced damage or media exchange as the cause for the observed decreased mobility are summarised qualitatively in **figure 4.2**.

The one consistent factor relating the samples observed with higher motility in the anaerobic capillaries to the samples in the table of **figure 4.2,** with motility in the low oxygen region, is the presence of an anaerobic electron acceptor (fumerate). In the case of samples diluted directly from overnight microaerobic culture it is expected only a relatively low level of fumerate is present, assuming the majority is consumed in the overnight incubation, which is subsequently diluted 5-fold before addition into the capillary tube. Any remaining fumarate could act as a respiratory bridge between O_2 exhaustion and any adaptions required to respire either directly or indirectly with the electrode.

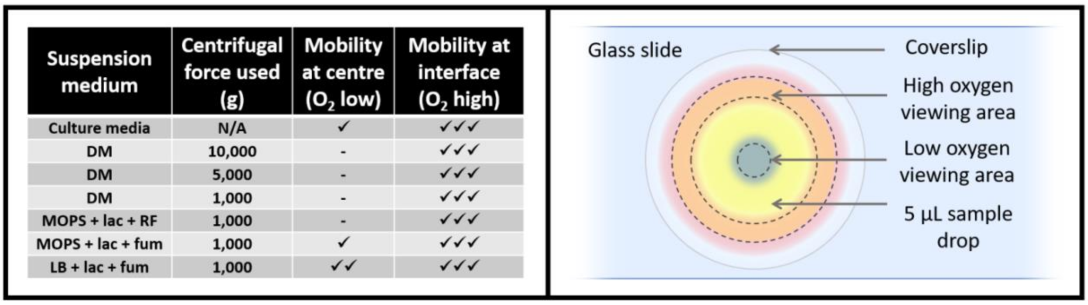

Suspension medium	Centrifugal force used (g)	Mobility at centre (O_2 low)	Mobility at interface (O_2 high)
Culture media	N/A	✓	✓✓✓
DM	10,000	-	✓✓✓
DM	5,000	-	✓✓✓
DM	1,000	-	✓✓✓
MOPS + lac + RF	1,000	-	✓✓✓
MOPS + lac + fum	1,000	✓	✓✓✓
LB + lac + fum	1,000	✓✓	✓✓✓

Figure 4.2. **Left** is a comparison of different centrifugal forces and re-suspension medium on MR-1 motility within a 5 µL drop on a glass microscope slide and covered with a glass circular cover slip. **[RF]** = 2 µL riboflavin, **[MOPS]** = 20 mM MOPS, 30 mM Na_2SO_4 pH 7.4, **[lac]** = 50 mM lactate, **[fum]** = 25 mM fumarate, **[DM]** = Defined minimal media, [Culture media] = original micro aerobic MR-1 culture (LB, lactate and fumarate) after overnight incubation, **[-]** = no/negligible motility, **[✓]** = low/moderate motility, **[✓✓]** = high motility, **[✓✓✓]** = very high motility. **Right** is a diagram illustrating the simple experiment set up, highlighting the two areas used for high and low O_2 concentrations.

To be certain that centrifugation was not having any effect on motility and that the low motility observed, in the capillary cells was caused by the absence of fumarate or any other utilisable soluble electron acceptor, a more vigorous investigation would be required. Because it was possible to obtain reliable results with the current dilution procedure and the time limited nature of the project further investigation to obtain definitive answer was not practical.

4.2.3 SAM choice

In **chapter 3** it was demonstrated that thiols terminated with differing functional groups could be used to modify the electrochemical characteristics of a gold electrode to give selectivity to certain redox active molecules. For the investigation of the effects of riboflavin on the taxis of MR-1 towards electrodes poised at oxidative potentials it is necessary for the electrode to effectively re-oxidise the reduced riboflavin on the surface to create the oxidised riboflavin gradient hypothesised to enhance MR-1 taxis towards insoluble electron acceptors. Whilst working with the ultra-flat and clean template striped gold electrodes we reported that pure 8-mercapto-1-octanol SAMs gave better selectivity towards riboflavin as opposed to Fe^{2+}/Fe^{3+} and its complexes, whilst a mixed 8-mercapto-1-octanol: 8-mercapto-1-octanoic acid SAM was more selective for the Fe^{2+}/Fe^{3+} and its complexes with a more sluggish electron transfer with flavins (**figures 3.5** & **3.7**).

When comparing the mixed and pure SAMs on the Au wire no significant difference between pure and mixed SAMs, in both the riboflavin electrochemistry and the response of MR-1 to applied potentials above and below the riboflavin midpoint potential, was recorded. The only difference between the two SAMS was in the case of the Fe^{3+}/Fe^{2+} redox reaction. The gold wire with the pure 8-mercapto-1-octanol SAM displayed a good electron transfer couple with riboflavin but not with Fe species, similar to observations made with the clean ultra-flat gold. Conversely, the mixed 8-mercapto-1-octanol: 8-mercapto-1-octanoic acid SAM modified gold wire displayed relatively facile electron transfer with both riboflavin and Fe species (**figures 4.6** & **4.7**). As there was no significant difference between pure and mixed SAMs in riboflavin electrochemistry the mixed thiol (8-mercapto-1-octanol: 8-mercapto-1-octanoic acid) SAM was used in most experiments to enable observations of Fe effects on the MR-1 taxis response alongside riboflavin.

SAM formation is very sensitive towards surface properties, including topography and surface fouling [139-141]. When compared to TSG the surface of gold wires are expected to have higher surface roughness. TSG electrodes experience only very limited (< 1 minute) exposure to unfiltered lab air prior to SAM formation, thus the opportunity for surface fouling is kept to a minimum. In contrast, the gold wire was subject to prolonged (weeks to months) exposure to the lab environment and its storage conditions prior to delivery are unknown, thus the wire almost certainly has a relatively high degree of surface fouling compared to TSG. SAMs formed on the gold wire are expected to be less compact/ordered and contain more defects compared with those formed on TSG [139]. Electron transfer between SAM modified gold electrode and electrochemically active species is highly sensitive to the SAM quality (for example the amount of pinhole defects), thus differences in electrochemical behaviour between the SAM modified TSG and the SAM modified Au wire (25 µm diameter) could be a consequence of differing surface properties. The surface fouling could be reduce using a cleaning procedure but due to the fragility of the gold wires (25 µm diameter) cleaning regimes using harsh conditions were avoided.

4.2.4 Video microscopy

For cell tracking with video microscopy, the optical microscope technique employed, must provide sufficient contrast between the objects of interest (e.g. bacteria) and the background. Fluorescent microscopy is therefore often the technique of choice, although bright field and phase contrast are also used if sufficient contrast can be obtained. Both fluorescence and bright field microscopy have been reported in the literature for cell tracking experiments involving MR-1 [133, 134]. For cell tracking experiments in this project bright field microscopy was employed to avoid the requirement of a fluorescent probe.

The microscope objective magnification should be selected with two primary considerations. Firstly, the magnification must be great enough to clearly distinguish the bacteria from the background with a size considerably larger than a pixel so not to be effected by pixel noise (much more relevant for bright field mode than fluorescence). The resolution should also be high enough to not act as the limiting factor for the smallest identifiable feature in an image. Secondly, the objective should permit the observation of a sufficient area. In the case of the capillary cell experiments ‘sufficient’ means an area size large enough to observe both an area close to the electrode and one sufficiently far away, to establish a relationship between bacterial movement and distance from the electrode. If the required area cannot be viewed within one frame an alternative method is to sequentially video the required areas, although this would be far from ideal for these experiments. If the fluorescent mode is used the numerical aperture (NA) also becomes very important, especially with low fluorescence.

Both a 40 x in air objective with a long working distance but low NA and a 60 x oil immersion objective with high NA (1.4) were used during pilot experiments. Although Identification of bacteria was enhanced with the 1.4 NA objective and the frame area size was acceptable, the issues caused by the very short working distance and emersion oil on the capillary outweighed any benefit. Using the standard base for the capillary tube required flipping the cell to obtain contact between lens oil and capillary. The capillary face is not-flat making it difficult to keep stable after connecting to the potentiostat cables. The emersion oil also ends up flowing from the capillary centre to both ends and mixing with the silicone grease sealant. Unfortunately, problems still occur with a capillary cell base specifically designed for the 60x objective (cell design iteration **3** of **figure 4.1**). A special opening in the base underneath the capillary for the lens to contact the capillary also leaves a section of the capillary with no support. This section sticks to the oil and deforms when moving the stage. The 40 x objective was sufficient to allow bacteria identification in images, allows for a good size viewing area, and has a large working distance in air making it simpler to work with. Consequently, instead of continuing efforts to make the capillary cell set-up compatible for use with the 60 x, the 40 x objective was used for all subsequent experiments. It is worth noting, prior to adapting the original Matlab interpretation of the Crocker algorithm, in relation to the position locating function, it was problematic to locate a sufficient proportion of the bacteria accurately without false positives from 40 x bright field videos. To provide the bacteria more contrast and make their identification easier, a long-distance phase contrast 60 x objective was trialled. Unfortunately, in addition to substantial drawbacks, the bacteria were not made “easier” to identify over an acceptable depth.

Higher frame rates and resolution enable more accurate tracking of bacterial trajectories in the resultant videos. With the hardware available it was not possible to achieve high frame rates at acceptable resolutions and the majority of video microscopy experiments were limited to 10 FPS with 2x binning (final resolution 1280 x 1080). At higher frame rates the capture rate becomes inconsistent, with the actual average frame rate of the saved videos far lower than the input frame rate. In addition to inconsistent frame rates, huge sections of frames for up to 5 seconds were missing. This made analysis more complex and unreliable. Large frame stacks of un-binned images (2560 x 2160) resulted in excessively long saving times > 1 hour. While videos were saving no measurements could be taken preventing the observation of any changes taking place in the hours following loading the bacteria into the capillary set-up.

Capillary cell experiments originally lasted ~5 hours after initial set up. During experiments it was frequently observed that after the initial 30-60 minutes from adding the bacterial suspension to the capillary cell activity was very low regardless of applied potential. Over the proceeding 5 hours activity would gradually increase with no signs of stopping/slowing. It was therefore decided to extend the monitoring time. The experimental set-up was not designed for long experimental times over multiple days and it was not known how long the set-up could last for without leaking or drying out. To ‘preserve’ the capillary cell set-up It was stored in the fridge (4 °C), between observation periods (overnight). Advantages of the low temperature for storage include a longer doubling time thus supressing overgrowth which can cause numerous issues. A slower metabolism preserves remaining nutrients and keeps the bacteria alive for longer. Using the fridge for overnight storage capillary cells were typically monitored with periodic videos for 1 – 3 days after initial set-up although in some cases this was extended to 5 or even 8 days. It is important to note that the length of time MR-1 would stay active for varied greatly between experiments.

4.2.5 Cell tracking

From videos stacks of images (frames) are extracted and bacterial locations identified, either by hand or using algorithms. An example of a simple locator algorithm uses image filters to enhance the objects of interest, while supressing noise, prior to finding peak intensities. Alternatively, more sophisticated algorithms, which identify individual bacteria by their shape along with their neighbours have been used in cases of high bacterial crowding where the bacteria are moving slowly over flat surfaces either by growth or swarming [142, 143]. Once the bacterial positions have been located in the image stack bacterial traces are obtained either manually or with the help of tracking algorithms [144].

The algorithm develop by Crocker *et al* [145], for sub-micron particle tracking, has been used and built upon extensively within diverse fields ranging from colloidal sciences for tracking colloidal particles undergoing Brownian motion to microbiology for tracking self-propelled chemotactic bacteria [146] [144]. Since the tracking algorithm was published in 1995, it has received over 1700 citations (as of 01/12/17 on “Web of Science”), a large proportion of which implement a version of the method outlined by Crocker. The attention the paper has enjoyed is a tribute to the simplicity and versatility of the algorithm and resulted in its validation in a range of varied systems. It is important to note that a modified Matlab implementation was used successfully to generate traces to an acceptable degree of accuracy with MR-1 as the test organism by Harris *et al* [133].

The Crocker algorithm is tolerant to noise and capable of distinguishing between particles by size. This is useful when working with biological samples where debris may be of concern or particles/bacteria in the plain of interest are obscured by out of focus particles/bacteria. Fluorescent labelling of the particles of interest is not required with the Crocker algorithm and it works well with bright field images undeterred by sub optimal contrast. Particles moving in and out of focus can be an issue for tracking, for example, the algorithm may identify each reappearance of the same particle in the plane of focus as a new particle resulting in what should be one track becoming multiple broken up tracks. Crocker’s algorithm saves the location of the last known position of particles from traces which disappear and can identify the reappearing particle as the same particle so long as spatial and temporal translations are within a specified limit. Indeed, the Crocker algorithm works to reduce the creation of new tracks by applying a penalty to combinations in which new tracks are formed. This is an essential feature when working with highly motile bacteria such as MR-1 which are free to move in all 3 dimensions. For these reasons, and because there is an up to date Matlab version of the algorithm freely available, the Crocker algorithm was chosen as the base code for extracting quantitative results from the video data generated by capillary cell experiments.

The actual Matlab code was downloaded as four functions (bpass.m, pkfnd.m, cntrd.m, and track.m), from a repository, maintained by Daniel Blair and Eric Dufresne. ‘bpass.m’ is an image filter, which uses multiple calls to the matlab convolution function ‘conv2’, to produce the desired band pass, for suppressing both pixel noise and long wavelength features (above an input length value), whilst retaining features of a specified size range. ‘pkfnd.m’ is a peak finding function for locating the origins of the enhanced features, retained by the band pass, to pixel level accuracy. If required an additional function ‘cntrd.m’ can be used to obtain sub pixel accuracy. Finally, 'track.m’ is a function for finding the ‘most’ probable trajectories from the locations identified in a stack of images.

Sub-pixel accuracy was not necessary for the purposes of tracking bacteria from the videos obtained in this project. Image resolution, feature contrast and the irregular shape of bacteria would have made it difficult to obtain legitimate sub-pixel accurate particle locations using the ‘cntrd.m’ function. Thus ‘cntrd.m’ was not used in the video processing script. Originally the script was built around the three functions ‘bpass.m’, ‘pkfnd.m’, and ‘track.m’. Prior to processing video sections bpass parameters were calibrated, using a representative image from the video, to find the best parameters for locating bacteria. Then sections from videos, (as image stacks), along with a table containing frame times, was processed using the mentioned script to obtain sorted position lists, grouped into probable traces and ordered chronologically. From the lists traces were plotted and examined alongside the original video to check how well the resultant traces correlate with the actual video of swimming bacteria. Unfortunately, the script using the unadulterated image filter and tracking function was only capable of forming acceptable traces in a small subset of videos. Those videos where acceptable traces were formed generally had relatively sharp contrast with large separations between bacteria. Even under these conditions many obvious bacterial trajectories observed in the video were missing in those tracked by the code. In addition to missing traces numerous artefacts were observed in the plotted traces.

The artefacts and missing traces were not caused by any one single factor but instead the result of many contributing factors. Those factors identified as causing issues and the steps taken to improve the processing script are outlined below.

Boundary conditions

Zero padding is a common step in many image filtering functions for dealing with boundaries before applying kernels over images either in real or Fourier space. The band pass filter ‘bpass.m’, used for highlighting bacterial positions, zeros the borders of the image with a thickness related to the input feature length. Usually, the borders imposed by bpass are relatively thin, but If multiple calls to bpass are required for the same image or the feature size is relatively large, the effect can become an issue. In addition, the peak finding function ‘pkfnd.m’ cannot find locations close to borders, thus if a new border is introduced, the space available for locating positions is further reduced.

To have full control over boundary conditions and prevent border cropping or distortion, the custom filter imgFilterF.m was developed, using the matlab fast fourrier transform implementation. A band pass function was then created using ImgFilterF.m. Briefly, a low pass filtered image with cut off at frequency X is subtracted from a filtered image using another low pass filter but with a lower cut off frequency Y. The resultant image is thus made from frequencies between X and Y resulting in a band pass with upper bound X and lower bound Y. Importantly the filter ImgFilterF.m deals with boundaries by reflecting a section of the borders prior to transforming into Fourier space and applying the desired kernel. The function does not result in any cropping or distortion of image borders and gives the user more control over the band pass range compared to bpass.m. This function was also ideal for creating precise masks and finding the borders of certain features which were required for data processing later. The downside to this function, as with many custom functions using matlab, is processing time compared to bpass which uses in built matlab functions, although due to the benefits of the new function the extra processing time was tolerable.

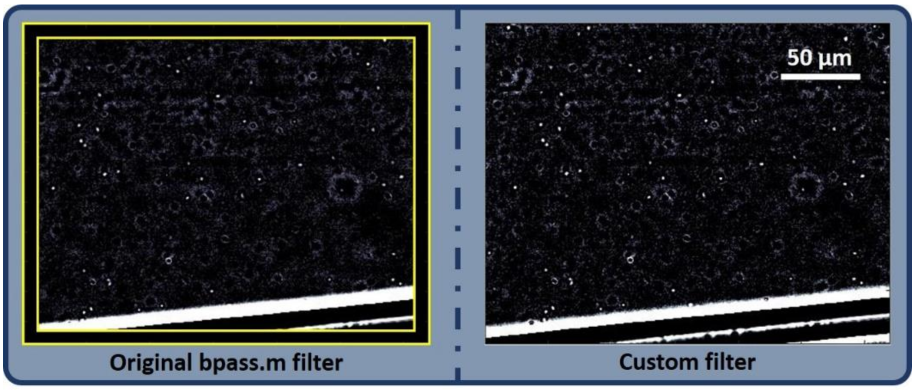

Figure 4.3. Comparison between the original band pass filter (bpass.m) and the custom filter (imgFilterF.m). Both filters where set up to achieve the same high and low cut off frequencies. Resulting images still differ slightly due to the differences between implementations, for example the kernel is applied in real space for bpass.m while for imgFilterF.m the kernel is applied in Fourier space. The area cut from the image, processed using bpass.m, is highlighted by the difference between the inner and outer yellow boxes around the image resulting from bpass.m.

With the original script it was possible to locate features of high (bright spots) or low (dark spots) relative intensity, within a narrow size range. But it was not possible to locate both high and low relative intensities in the same image or use multiple size ranges for locating bacteria. This is not an issue if all the particles/bacteria of interest occupy a single plane so that they all share the same size range and relative intensity compared to the background. In the case of the capillary cell experiments, the bacteria are free to move within a relatively large depth range (50 µm). Depending on the plane a bacterium is in, relative to the plane in focus, it can appear as a darker or lighter feature in the image. In addition their apparent size and sharpness also varies with distance from the focal plane. It is therefore desirable to locate both light and dark feature of multiple sizes, representing bacteria at varying depths, to include positions over a larger depth range which will in turn increase the average trace length.

To increase the depth in which bacteria are located the difference between the low and high bandpass filters can be increased and threshold intensity decreased. The decrease in selectivity, resulting from the broadening between band pass filters and decrease in threshold intensity, inadvertently increases the frequency of false positive bacterial locations. To overcome this, at the cost of cpu time, one can separately apply multiple band pass filters to an image, forming multiple processed images all with a different feature size selected for. This method reduces false positives while increasing the proportion of correctly located bacterial positions. Occasionally the different band pass filters identify the same bacteria usually with a difference of a few pixels between them. To prevent processing multiple positions for the same bacteria, positions found with one band pass filter within ~15 pixels of a position found using a different parameter set are compared and the lowest relative intensity location deleted. These changes to the process of locating bacteria were implemented as additional logic in a locator function which also incorporates a wrapper containing ‘imgFilterF.m’ (replacing bpass.m) and ‘pkfnd.m’ as sub functions. An abstraction of the process for locating bacterial positions is described in **scheme 4.1**.

In all microscopy videos taken only a sub-population of MR-1 were motile with a much higher proportion of non-motile bacteria. Previous investigations involving video microscopy of MR-1 have also reported only a sub population of motile cells [132-134]. To acquire large enough ‘n’ values for swimming bacteria and ensure statistical significance of the results, the bacterial density had to be sufficiently high. The penalty for processing frames with a greater bacterial density is an increase in probability for neighbouring bacteria crossing paths and having a shorter inter bacterial distance then the distance travelled per frame of the fastest bacteria. Inter bacterial trace tangling becomes an issue once the average inter bacterial distance becomes equivalent to, or lower than, the distance searched for consecutive bacterial locations between frames. Inter bacterial trace tangling is obviously not desirable and leads to spurious results and longer processing times (due to increased linking combinations).

Stationary objects with pixel intensities at the edge of the threshold applied become identified as valid bacterial locations in only a portion of the frames, appearing as transient positions. When there are two or more instances of transient stationary positions, within the max displacement distance of each other, artefacts emerge in the resulting traces. Even with only one such transient point artefacts can arise from bacteria swimming past. In the event the sensitivity for locating bacteria is too high, arbitrary positions are falsely identified from noise, which usually is not a problem unless they occur close to a transient position or in high frequency. Artefacts usually appear as highly repeated patterns of positions within a trace that can be easily spotted, as shown in **figure 4.4** by the blue traces. Such artefacts can significantly impact the analysis with inadvertent effects on the resulting average velocity and average swimming direction extracted from the traces.

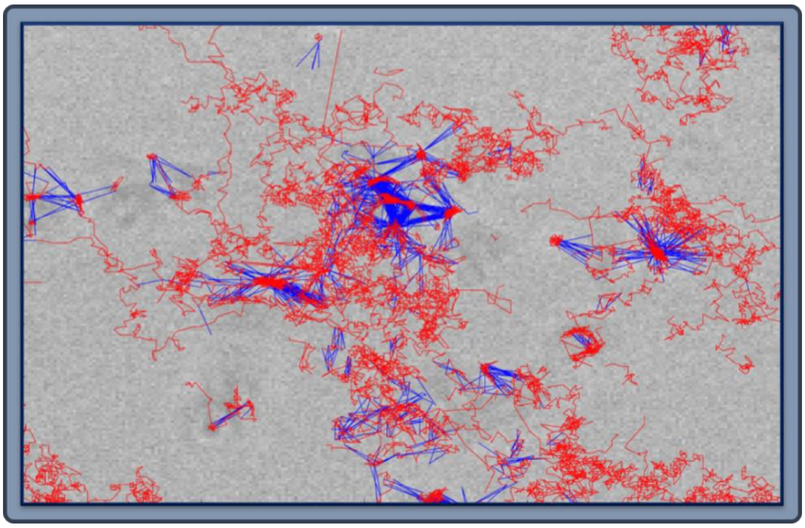

Figure 4.4. Expanded selected area of a video frame (rows 225 through to 305, columns 495 through to 785 from a frame with 1080 rows x 1280 columns), overlaid with two sets of plotted traces from results, obtained with the same input list of positions but using different tracking algorithms. Traces plotted in **blue** were obtained using the original Matlab implementation of the Crocker algorithm, with the max displacement set at 30 (30 pixels is the maximum valid max displacement value, whilst using this position list and algorithm, due to excessive linking combinations). Traces plotted in **red** were obtained using the adapted Crocker algorithm developed during this project, with the max displacement set at 50 (although higher values can be used). The blue trace only shows trajectories obtained using the original algorithm that were not found by the adapted algorithm. In places where blue and red traces follow the same path, only the red trace is visible. The selected area, expanded in this figure, was chosen due to the presents of extensive artefacts whilst using the original Crocker algorithm and illustrate the effectiveness of the developed algorithm at reducing such artefacts.

To form traces from fast moving bacteria, without creating excess linking combinations and at the same time reduce the potential for artefacts and spurious traces, a new tracking algorithm was developed. The new tracking algorithm incorporates a slightly modified version of the original 'track.m' (the Crocker algorithm) as a sub function. An abstract flow diagram of which has been laid out in **scheme 4.3**. The custom algorithm takes substantially longer to process position lists, compared to the original algorithm but the resulting traces are formed with considerably less artefacts. Importantly, the custom algorithm can track bacteria traveling at velocities over 250% of the max velocity trackable by the original algorithm from the same data set. It should be made clear, that if a higher frame rate was used for the videos or the spatial density of bacteria was lower, the original Crocker algorithm should work well. The custom algorithms main advantage is to enable the tracking of higher velocities from videos of a sub-optimal frame rate (e.g. 10 FPS).

4.3 Materials and Methods

Mutant strains

The double deletion ΔmtrC/ΔomcA (SO_1778/SO_1779) mutant of *S. oneidensis* MR-1 was obtained as a kind gift from J. butt and L. Shi [147].

The Δbfe mutant (deletion of SO_0702 which encodes a multidrug and toxin efflux transporter, renamed to bacterial flavin adenine dinucleotide exporter i.e. bfe) of *S. oneidensis* MR-1 was obtained as a kind gift from the J. A. Gralnick [107].

Growth and media

S. oneidensis MR-1 and mutants (ΔmtrC/omcA or Δbfe) were grown weekly on LB plates from -80 °C glycerol stocks. Single colonies, from plates no more than 3 days old were used to inoculate LB (15 mL) in a 50 mL falcon tube. With cap loosened, the cultures were incubated aerobically (30 °C, 200 rpm, 16 h) to an optical density $OD_{600\,\mathrm{nm}}>1$. A small sample (~500 µL) of this culture was used to inoculate LB (50 mL) supplemented with 50 mM lactate and 25 mM fumarate in a 50 mL falcon tube. To facilitate microaerobic/semi-anaerobic conditions, the top of the tube was fastened shut and the culture was grown overnight (0 rpm, 30 °C). Once the dissolved oxygen has been exhausted by the bacteria, fumarate serves as a replacement electron acceptor. This set up allows for a gradual transition from aerobic to anaerobic.

After overnight semi-anaerobic incubation, cultures reached an $OD_{600\,\mathrm{nm}}$ of approximately 0.7 and pH of 6.25–6.30. In preparation for experiments, a 2 mL sample from the 50 mL cultures was diluted 5-fold with appropriate buffer to 10 ml. The buffer used in most experiments was MOPS buffer (20 mM MOPS, 30 mM Na_2SO_4 in H_2O at pH 7.4) supplemented with 50 mM lactate, with or without 2 µM riboflavin.

Capillary electrochemical cell set up

For reference, the capillary cell set up described here is depicted as iteration **number 5** in **figure 4.1**. All equipment used in the set-up, entering the capillary cell, was autoclave sterilised where possible or treated with isopropanol for non-autoclavable items. High purity Gold (99.99+%), silver (99.99%) and platinum (99.9+%) wire (25 µm diameter, GoodFellows), along with carbon fibre (7 µm diameter fibres from untreated tow, GoodFellows) was used as the capillary cell electrodes. Capillary electrochemical cells were constructed on standard 25 x 75 mm microscope glass slides (Fisher Scientific). Before use the glass slides were treated, as per instructions, with Sigmacote® (hydrophobic coating from sigma). Glass capillary tubes (0.05 x 0.5 x 50 mm, Microslide Tube, Camlab, UK) were placed onto the centre of the glass slide and kept in place with two ~3 x 15 mm pieces of scotch tape near both ends of the capillary tube. A further, smaller capillary tube (0.02 x 0.2 x ~15 mm, Microslide Tube, Camlab, UK), shortened from its original 50 mm length, was placed inside one end of the larger capillary tube, with a ~2 mm section left out. The purpose of the smaller capillary tube is to spatially separate the counter and reference wire to prevent contact. On one side of the capillary opening/end with the smaller protruding capillary, a platinum wire (25 µm diameter, 40 - 50 mm long) was inserted along the gap between the outer and inner capillary, extending slightly (~1-3 mm) beyond where the end of the inside capillary was resting. Through the gap on the opposite side of the same end in which the platinum wire was inserted, a Ag/AgCl wire (25 µm diameter, 40 - 50 mm long) was inserted, parallel to the platinum wire but physically separated by the smaller capillary. Both wires extended ~15 mm into the main capillary with ~25 - 35 mm left protruding out from the capillary. If required, small adjustments can be made at this point, using tweezers and microscope, until both the Ag/AgCl and platinum wires extend by 1-3 mm beyond the end of the inside capillary. Once the platinum wire (counter electrode) and Ag/AgCl wire (reference electrode) had been positioned correctly silver conductive paint (Electrolube, HK Wentworth Ltd, UK) was used to fix the wires in place by liberal application over the wire ends on the outside of the capillary in contact with the glass slide. A ~10 mm gap was left between each of the two painted areas. After ~5 min, once the silver paint had become set, conductive adhesive copper tape strips (~ 10 x 40 mm) were firmly stuck onto each painted area separately, preventing any contact between them. Most of the copper tape length protrudes out of the glass slide enabling connection to potentiostat cables via crocodile clips.

To fill the half assembled capillary cell with bacterial suspension, approximately 1.5 mL of Bacteria suspension, prepared as described above, was transferred into a sterile 1.5 mL Eppendorf tube. The scotch tape was removed from near the end of the capillary with no wires inserted and the capillary tube prised gently away from the glass slide while still attached with scotch tape at the other end. Under sterile conditions (i.e. under a blue flame), with the Eppendorf in an upright position and lid wide open, the free end of the capillary tube is submerged into the bacterial suspension just below the surface. The capillary tube was filled with suspension through capillary action before careful removal from the Eppendorf. The time taken to fill the capillary varied, from a few seconds to a few minutes. With the right lighting, it was possible to see the liquid level rise. Once removed the liquid levels can also be checked under microscope and, if inadequate, the filling process repeated. Once adequate liquid levels had been confirmed the free end was re-fixed onto the glass slide with a thin slice of scotch tape. To prevent liquid level receding due to evaporation and to minimise delays between adding the bacterial suspension to the capillary cell and tracking experiments, the remainder of the cell set-up must be completed rapidly.

Silicon vacuum grease was applied to the opening, of both the larger and smaller capillary, at the end where Ag/AgCl reference and platinum counter wires were inserted. A SAM modified Au wire (25 µm diameter, 40 - 50 mm long) was then inserted into the unsealed end of the main capillary, reaching 15 - 20 mm and keeping ~15 - 20 mm distance between the Au wire and the reference/counter wires inserted into the opposite end. The unsealed end, with inserted Au wire, was then sealed with silicon vacuum grease and the section of Au wire extending out of the capillary, was fixed to the glass slide using silver paint, prior to sticking copper tape onto the painted area as previously described for the reference and counter wires. Once the silver paint is fully set (~10 mins), crocodile clips were used to connect the copper tape with the potentiostat (Chi604c, CH Instruments, Inc., Texas, U.S.A). The cell was placed on the microscope viewing area such that the lens is aligned with the end of the Au wire in the capillary.

SAM modified gold wires

The most frequently used thiol solution used to modify the surface of gold wires, prior to their use in experiments, was a 1 mᴍ 57:43 mix of 8-mercapto-1-octanol:8-mercato-1-octanoic acid in isopropanol. To form SAMs, gold wires (25 µm diameter, 40 – 50 mm long) were submerged into 10 mL of thiol solution contained in 15 mL disposable glass vials. Once the container cap was screwed shut the wires would be left to incubate for ~48 h at room temperature (20 – 25 °C). Prior to use in capillary cells the wires were rinsed with isopropanol and the excess isopropanol readily evaporated in < 1 min.

Ag/AgCl reference wire

Ag/AgCl reference electrode wires were produced electrochemically using a standard three electrode set-up. Saturated potassium chloride in H_2O was used as the electrolyte. A red rod Ag/AgCl reference electrode was used as the reference and platinum wire as the counter. Pure Ag wires (25 µm diameter, 50 – 60 mm long) were used as the working electrode with one end submerged by 20 mm into the electrolyte. Due to the fragility of the thin Ag wire, direct attachment to the potentiostat cables using crocodile clips was not practical. Instead ~ 10 mm of the non-submerged end was attached to a strip of copper tape with silver paint. Crocodile clips could then be conveniently connected via the copper tape. To form a layer of AgCl on the Ag wire a potential of +200 mV (vs Ag/AgCl) was applied for 60's, at which point the submerged part of the wire had changed from shiny silver to a dull brown/black colour. The wire was then removed from the set-up and rinsed with H_2O prior to storage in sterile plastic petri dishes with lint free microscope tissue lining (prevents the wires electrostatically, 'sticking' to the plastic petri dishes). Just before use in the capillary cell experiments the previously attached copper tape is cut off leaving just the wire, with a total length of 40 - 50 mm.

General Experiment Procedure

All potentials are given are versus standard hydrogen electrode (SHE) unless stated otherwise. For potentials recorded at room temperature, using Ag/AgCl wire reference electrode in pH 7.4 buffered solutions containing 34mM Cl^- (as used in the capillary cells), the potential versus SHE is obtained by adding 0.308 V to the applied/measured potentials. The 34 mM Cl^- arises from the 5-fold dilution of LB based media which originally contains 10g/L (~171 mM) of NaCl.

Once the capillary cell was fully prepared with loaded bacterial suspension visual checks were made around the electrodes in the capillary to qualitatively asses the initial bacterial motility using an inverted optical microscope (Eclipse Ti-U, Nikon Instruments, U.K.) with 40 x air objective N.A. = 0.7 and attached to an Andor Zyla 5.5 sCMOS camera (Andor Technology Ltd., U.K.). The capillary cell was then connected to the potentiostat (Chi604c, CH Instruments, Inc., Texas, U.S.A) and turned on. After connecting the capillary cell wires to the potentiostat cables, using the copper tape as a flexible conductive bridge, the capillary cell stability and electrical connections between wires were checked by electrochemical techniques. The open circuit potential was monitored for one minute; if the voltage was stable, cyclic voltammetry was used to check for riboflavin and a redox peak at more positive potentials attributed to Fe-lactate in **chapter 3**. These redox signals were useful for checking the potential of the Ag/AgCl wire reference electrodes before attempting to set the working electrode at a desired potential for video experiments.

After the stability of the set-up was confirmed electrochemically the capillary cell was left for ~ 30 minutes, in most cases, to allow the bacteria to exhaust the remaining oxygen and reach a relatively steady state. A suitable (visually clear) location was identified for the experiment using the optical microscope in bright field mode. The working electrode was put in focus, (required for the video processing), preferably with the plane of focus mid-way between the floor and ceiling of the capillary interior. Videos were taken at 10 FPS with 2 x binning for a typical duration of 8 - 9 minutes (using the 40 x air objective and Andor Zyla 5.5 sCMOS camera), in parallel to a pre-set regime of changes to the applied potential using chronoamperometry to record the current. Typical chronoamperometry programs used are described below. After the videos were saved (saving times can take 20 to 60 minutes), electrochemical measurements (10 and 100 mV /s CVs between -400 to +600 mV) were taken. Typically, a further 2 to 3 videos along with complementary electrochemical measurements were performed. At the end of the experiment the capillary cell was disconnected and stored in the fridge at 4 °C. Frequently extra videos were taken on the following days, for up to a maximum of 5 days (8 days in one case).

Chronoamperometry regimes

The most common regime of applied potentials consisted of 3 phases. The first phases had an initial period of 60 s with the potentiostat cell turned off at the open cell potential (OCP), this was to get a baseline of activity prior to applying any potentials. Phase 2 and 3 were periods of up to 210 s, each with a different constant applied potential. The potential applied in phases 3 would usually be of the opposite relative sign, for example if a relatively negative potential (-0.3 V) is applied in phase 2, then a relatively positive potential (+0.3 V) is applied in phase 3. A four phase regime was also commonly used, the extra phase was between 60 to 120 s in duration and involved an applied potential close to or just above the midpoint potential of riboflavin (e.g. -0.15 V). The extra phase is located between the original phase 1 and phase 2.

Centrifuge and buffer exchange effect on MR-1 motility

50 mL of overnight micro aerobic MR-1 culture was prepared as described. 4 x 1 mL samples of the MR-1 culture were transferred into sterile 1.5 mL Eppendorf tubes. Three of the samples were pelleted at either 1,000 g, 5,000 g, or 10,000 g for 15 minutes. Supernatant was then discarded, and each pellet re-suspended in 1 mL defined minimal media. The remaining sample was left unchanged, to be used as a control. 5 µL from each of the 4 samples was pipetted on to separate glass slides and covered with coverslips. MR-1 motility was then recorded using video microscopy in a qualitative manner at two separate zones (**figure 4.2**), the edge and in the centre for high and low dissolved oxygen concentrations respectively.

Four 1 mL samples, taken from 50 mL of overnight micro aerobic MR-1 culture, grown as described, were pelted (1,000 g, 4 °C, 15 minutes) and re-suspended in four different buffers/media (either 1 mL of defined minimal media, MOPS buffer supplemented with 50 mM lactate and 2 µM riboflavin, MOPS buffer supplemented with 50 mM lactate and 25 mM fumarate, or LB supplemented with 50 mM lactate and 25 mM fumarate). MR-1 motility was then recorded using video microscopy as described above.

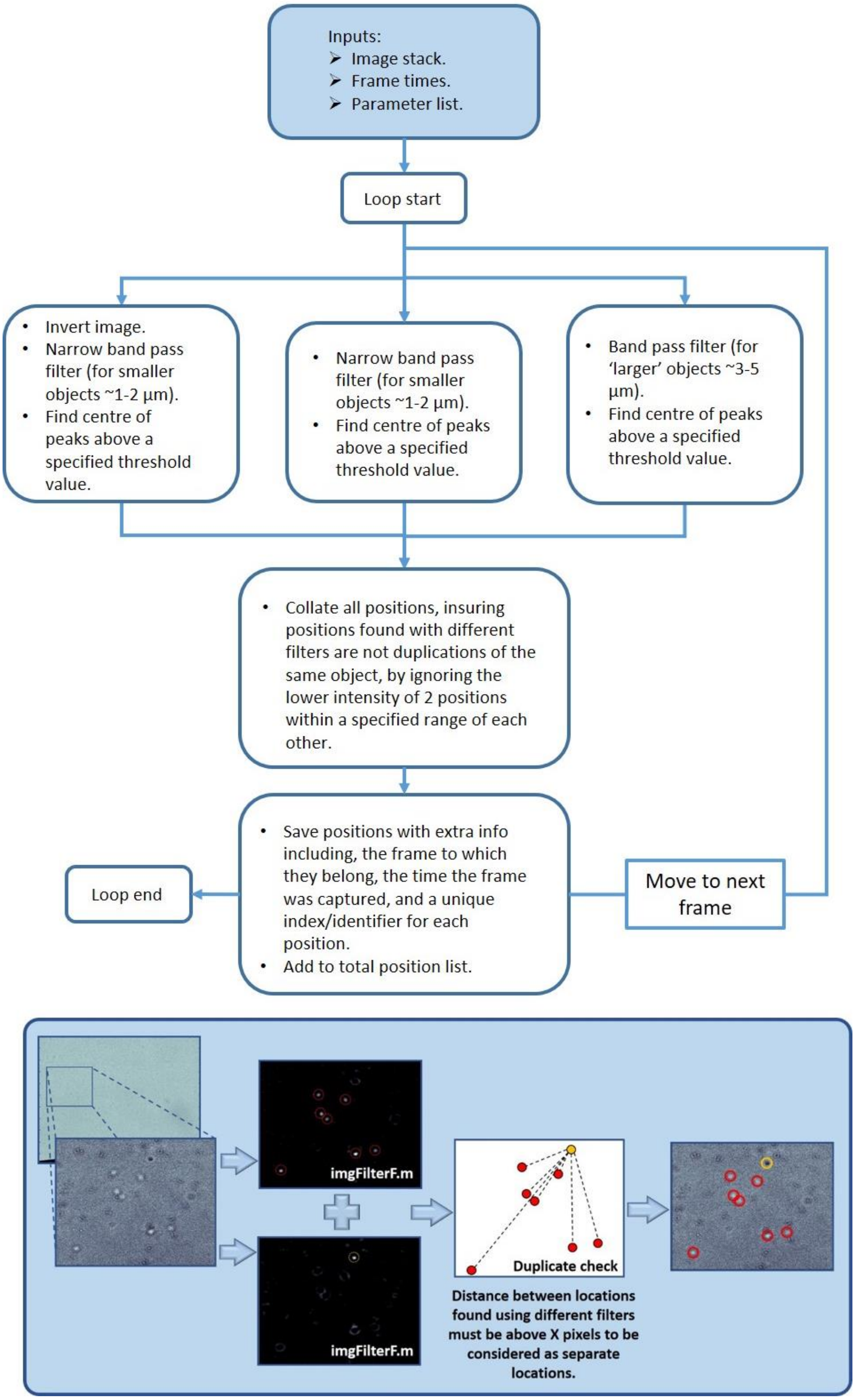

Scheme 4.1. Flow diagram overview of the bacterial position locating algorithm. The flow diagram gives a summary of the general procedures used by the code for locating bacterial positions from a stack of images and thus translating the images into a list of co-ordinates with time signatures that can be input into the tracking algorithms in **scheme 4.2 + 4.3**.

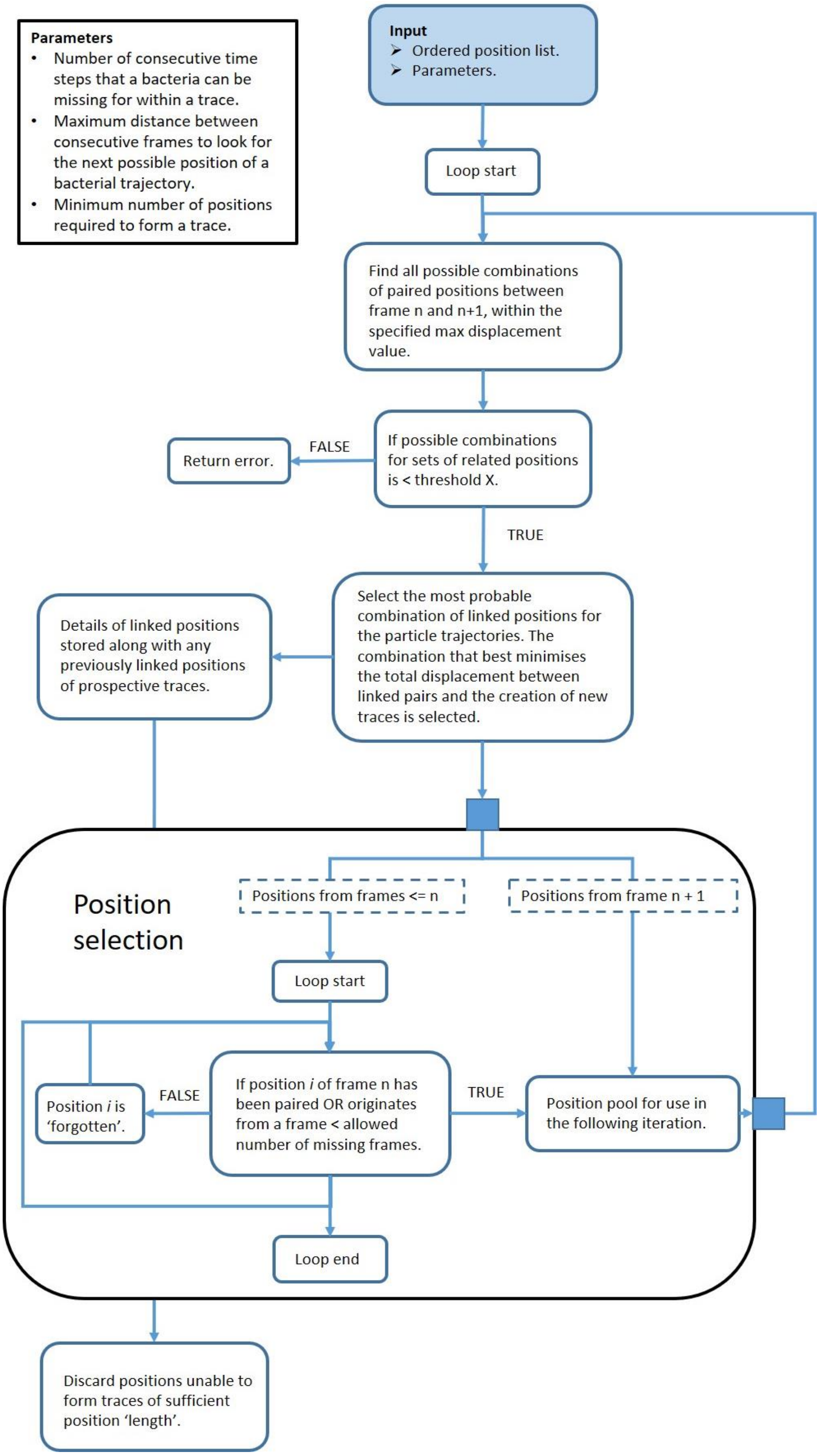

Scheme 4.2. Flow diagram overview of the original Matlab interpretation of the Crocker algorithm. The flow diagram gives an abstract summary of the general methodology used by the Crocker algorithm for generating the most likely trajectories from a particle/bacterial position list produced by the small algorithm outlined in **Scheme 4.1**.

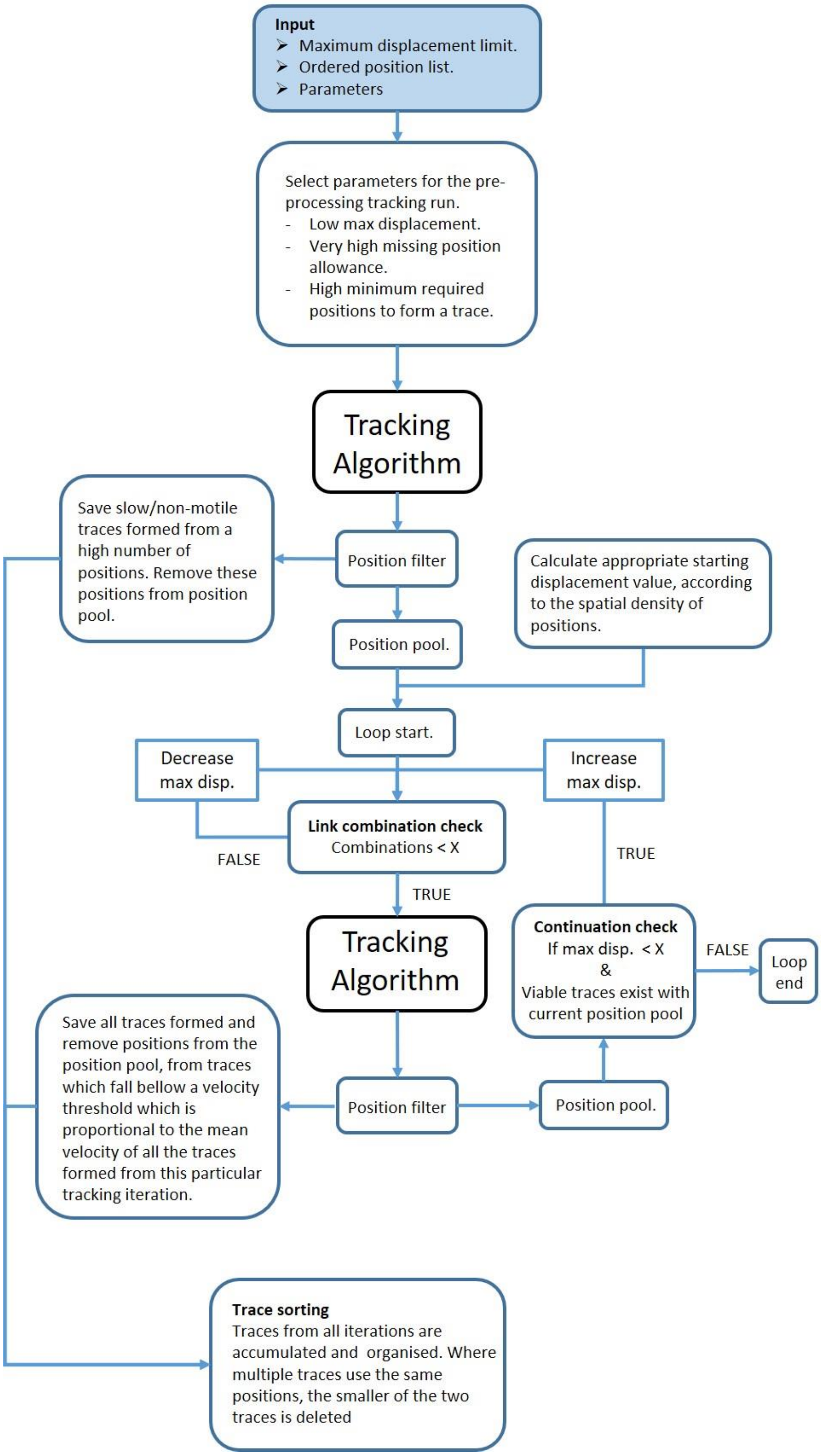

Scheme 4.3. Flow diagram overview of the custom tracking algorithm developed to address limitations with the original Matlab interpretation of the Crocker algorithm (**Scheme 4.2**). The flow diagram gives a summary of the procedures built around a modified version of the Crocker algorithm for generating trajectories with less artefacts and including traces from previously 'hidden' bacterial trajectories. Here '**Tracking Algorithm**' refers to the slightly modified version of the original Crocker algorithm, which is used here as a sub function.

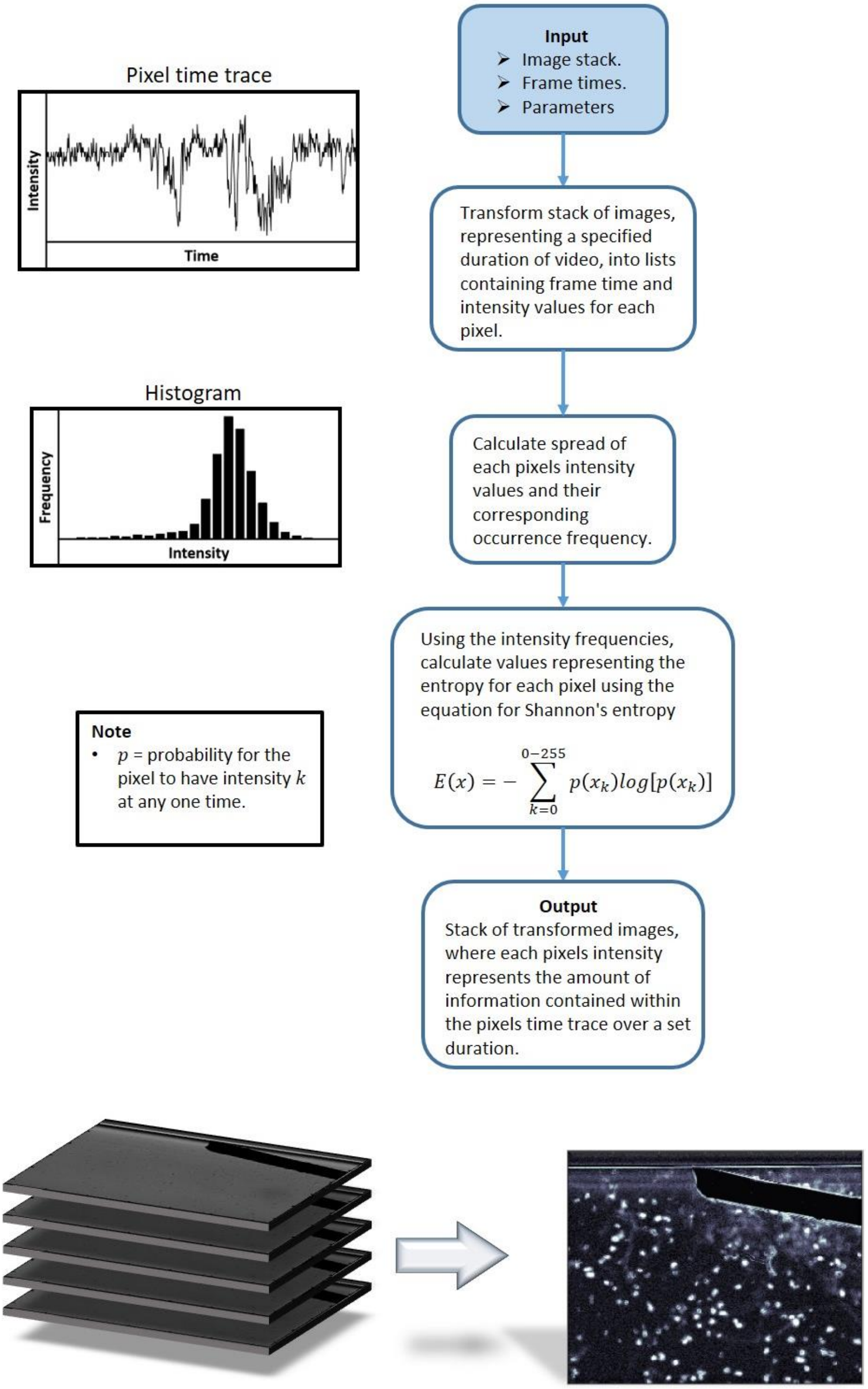

Input
- Image stack.
- Frame times.
- Parameters

Transform stack of images, representing a specified duration of video, into lists containing frame time and intensity values for each pixel.

Calculate spread of each pixels intensity values and their corresponding occurrence frequency.

Using the intensity frequencies, calculate values representing the entropy for each pixel using the equation for Shannon's entropy

$$E(x) = -\sum_{k=0}^{0-255} p(x_k)log[p(x_k)]$$

Note
- p = probability for the pixel to have intensity k at any one time.

Output
Stack of transformed images, where each pixels intensity represents the amount of information contained within the pixels time trace over a set duration.

Scheme 4.4. Flow diagram overview of the custom Shannon Entropy algorithm. The flow diagram gives a summary of the general procedure used by the algorithm for generating Shannon entropy images from an image stack.

4.4 Results

Capillary electrochemical cells were frequently monitored over 2-4 days. After the initial adaption period (approximately one hour) from loading samples into the capillary cell, bacterial motility was generally low and varied considerably between repeats of the same conditions. Over the next 8 – 48 hours, both the population of motile bacteria and average velocity increased to a peak. In a few rare cases, motility was diminished almost entirely after overnight storage. These cases typically had little motility within the first 5 h after sealing. The only indication remaining of an increased activity around the working electrode, was a build-up of stationary bacteria around the electrode, observable the following day (**figure 4.5**). Of the experiments with high motility on the first day, the electrode surface frequently developed a sparse covering of loosely bound bacteria (**figure 4.5**), a similar observation was previously reported by Harris *et al* [133], using carbon/graphite fibre electrodes and Mn_2O_3 particles.

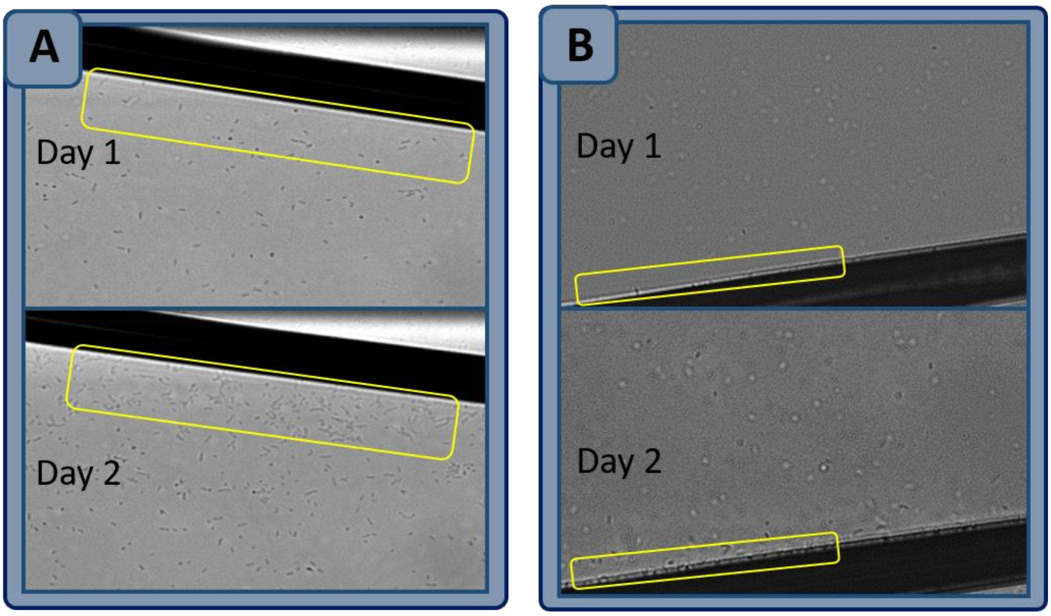

Figure 4.5. Bright field microscopy Images taken at the same location on two consecutive days for two separate experiments (**A**+**B**). On day 1, prior to the image taken, WT MR-1 samples were loaded into the capillary cells. Between taking the images on day 1 and 2, the capillary cells were stored in the fridge at 4 °C, for ~16 hr. Loaded sample contained MR-1 in overnight microaerobic culture diluted x5 with lactate (50 mM) supplemented MOPS buffer with **(B)** and without **(A)** added riboflavin. **A)** During day 1 almost no motility was observed. By day 2, the only sign that bacteria motility had probably increased considerably before declining between observations on day 1 and 2, was the significant build-up of bacteria close to the electrode. **B)** Loaded sample contained MR-1 in overnight microaerobic culture diluted x5 with lactate and riboflavin supplemented MOPS buffer (lactate and riboflavin final concentrations were 50 mM and 2 μM respectively). During day 1 low motility was observed compared to relatively high motility on day 2. By day 2, MR-1 had begun to cover the electrode, albeit sparsely.

The first measurement taken of any experiment was the open circuit potential (OCP). This was primarily to check that the capillary cell was connected properly, and the electrode wires were not short circuiting. The initial measurement was generally not a good representation of the OCP for the system in general as the system takes a while to reach an acceptable steady state and the OCP to become stable and hold a consistent value on the hour time frame. Here steady state is related to when the dissolved oxygen concentration becomes constant (i.e. after the bacteria have finished consuming the left over oxygen).

As mentioned in the methods, cyclic voltammograms at 10 and 100 mV/s were performed after initial set-up of the capillary cells and periodically throughout the experiment. Oxygen levels were monitored qualitatively using the CVs and observed to rapidly decrease (on a timescale of minutes) after the capillary cell was sealed. After 15 minutes most of the dissolved oxygen had been consumed by the bacteria. The level continued to slowly decrease further for the next 45 minutes and after 60 minutes ‘equilibrium’ had been reached, as determined by no more changes in the reduction level for oxygen (**Figure 4.9**). Only samples with the additional 2 µM riboflavin had a clear characteristic redox couple, at -0.2 V, corresponding to riboflavin (**Figure 4.7**). In the 10 mV/s CV. The riboflavin oxidation appears as a catalytic wave, indicating the bacteria are actively turning over the riboflavin for respiration. A redox couple at higher potentials (midpoint potential +0.14 to +0.21 V), was observed in almost all samples. The potential matches that of signals assigned in the literature to DET via outer membrane cytochromes (mtrC/omcA) although, after our own investigation into this signal (**chapter 3**), the author is more inclined to assign this peak to Fe-lactate. In concurrence with this, CV taken of ΔmtrC/ΔomcA deletion mutant during capillary cell experiments, maintains a redox couple with a midpoint potential of ~0.16 V and clear oxidation peaks at 0.175 V and 0.22 V for 10 and 100 mV/s respectively (**Figure 4.8**). **Figure 4.6** displays CVs of WT MR-1 with and without 10 µM $FeCl_2 \cdot 4H_2O$, the small oxidation peak at 0.175 V in the 10 mV/s CV from WT MR-1, is substantially enhanced in the presence of 10 µM Fe, suggesting that the peak is originating from Fe complexes as suspected.

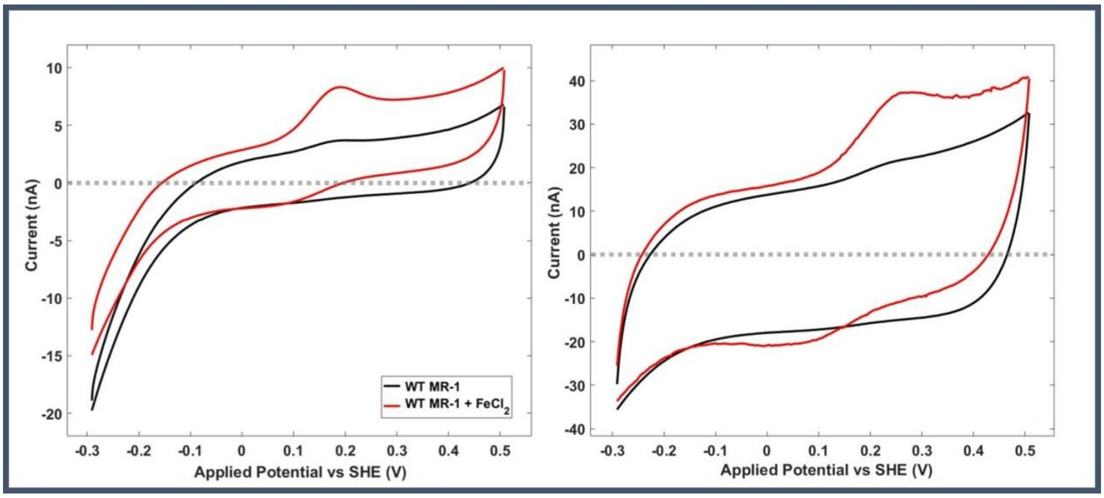

Figure 4.6. Cyclic voltammograms (CVs) at scan rates of 10 (**left**) and 100 (**right**) mV/s, recorded with capillary cells containing samples of WT MR-1, in anaerobic media, diluted 5-fold with MOPS buffer and supplemented with 50 mM lactate, with (**red**) or without (**black**) 10 µM $FeCl_2 \cdot 4H_2O$. CVs taken ~ 60 min from loading samples. The Working electrode was a gold wire (25 µm diameter) modified with a mixed 8-mercapto-1-octanol:8-mercapto-1-octanoic acid thiol solution. The counter and reference electrodes were a platinum wire (25 µm diameter) and an Ag/AgCl wire respectively. All scans start at the immersion potential E = ~0 V with an initial scan direction towards negative potentials. For clarity the initial negative partial scan is not plotted.

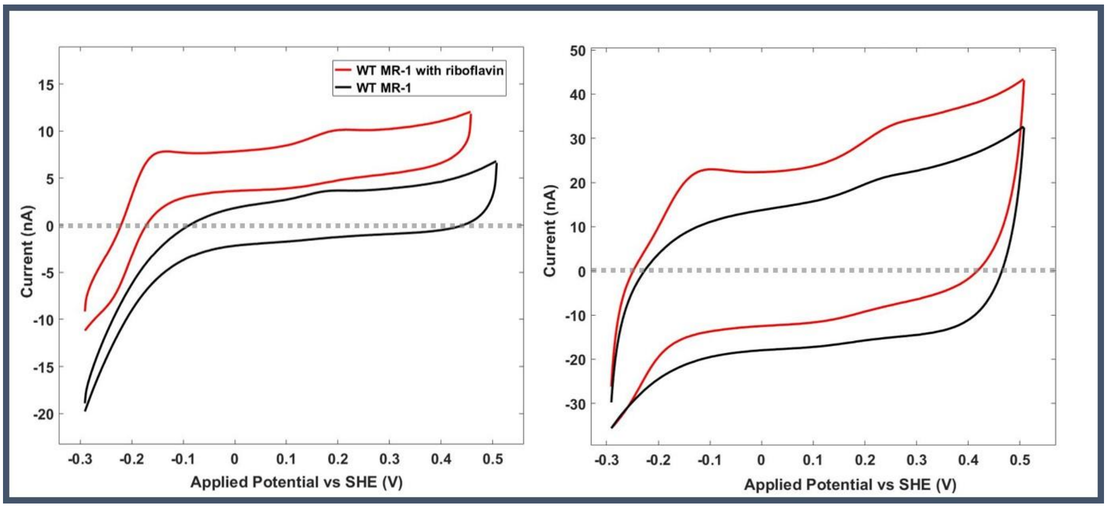

Figure 4.7. Cyclic voltammograms (CVs) at scan rates of 10 (**left**) and 100 (**right**) mV/s, recorded with capillary cells containing samples of WT MR-1, in anaerobic media, diluted 5-fold with MOPS buffer and supplemented with 50 mM lactate, with (**red**) or without (**black**) 2 µM riboflavin. CVs taken ~ 60 min from loading samples. The Working electrode was a gold wire (25 µm diameter) modified with a mixed 8-mercapto-1-octanol:8-mercapto-1-octanoic acid thiol solution. The counter and reference electrodes were a platinum wire (25 µm diameter) and an Ag/AgCl wire respectively. All scans start at the immersion potential E = ~0 V with an initial scan direction towards negative potentials. For clarity the initial negative partial scan is not plotted.

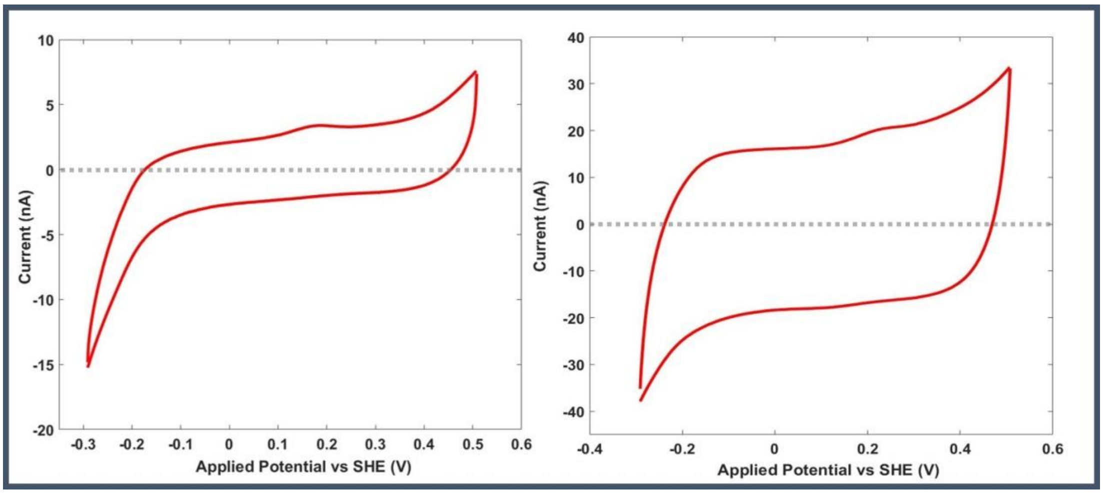

Figure 4.8. Cyclic voltammograms (CVs) at scan rates of 10 (**left**) and 100 (**right**) mV/s, recorded with a capillary cell, containing ΔMtrC/ΔOmcA, in anaerobic media, diluted 5-fold with MOPS buffer and supplemented with 50 mM lactate. CVs taken ~ 60 min from loading samples. The Working electrode was a gold wire (25 µm diameter) modified with a mixed 8-mercapto-1-octanol:8-mercapto-1-octanoic acid thiol solution. Platinum wire (25 µm diameter) and Ag/AgCl wire was used for the counter and reference electrodes respectively. Scans start at the immersion potential E = ~0 V with an initial scan direction towards negative potentials. For clarity the initial negative partial scan is not plotted.

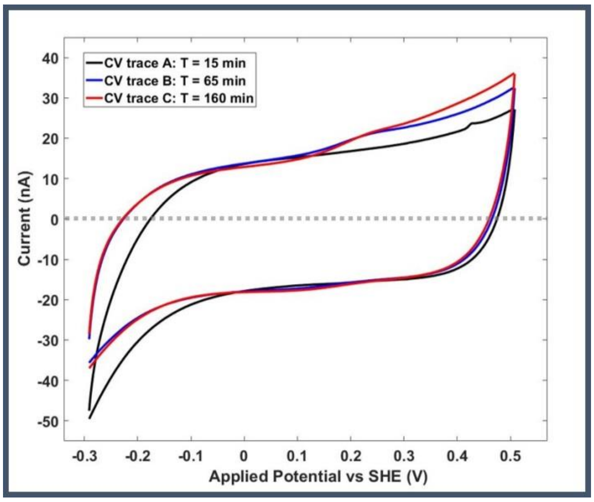

Figure 4.9. 100 mV/s Cyclic Voltammograms of a capillary cell over time after inoculation with a suspension of MR-1 diluted 5-fold from overnight micro-aerobic culture, using lactate supplemented MOPS buffer. Time zero (T = 0) refers to the moment the capillary is sealed with silicone grease. After 15 minutes most of the oxygen has been consumed by the bacteria but a small amount is present, which slowly decreases up until ~60 minutes after sealing, as seen in the reduction in the CV at T = 15 min compared to T = 65 min. Between T=65 and T=160 min, no more changes are observed with respect to reduction at potentials relevant to oxygen reduction. All scans start at the immersion potential E = ~0 V with an initial scan direction towards negative potentials. For clarity the initial negative partial scan is not plotted.

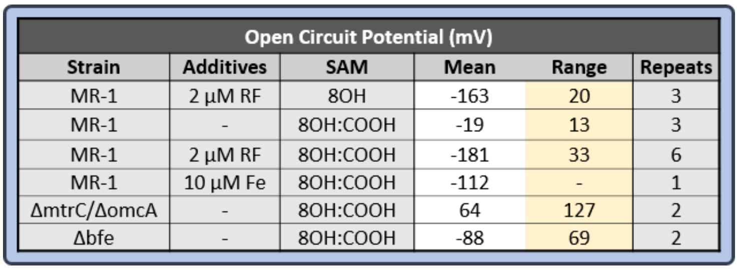

Open Circuit Potential (mV)					
Strain	Additives	SAM	Mean	Range	Repeats
MR-1	2 µM RF	8OH	-163	20	3
MR-1	-	8OH:COOH	-19	13	3
MR-1	2 µM RF	8OH:COOH	-181	33	6
MR-1	10 µM Fe	8OH:COOH	-112	-	1
ΔmtrC/ΔomcA	-	8OH:COOH	64	127	2
Δbfe	-	8OH:COOH	-88	69	2

Table 4.1. Table comparing open circuit potentials (OCP) of WT MR-1, with and without added 2 µM riboflavin or 10 µM $FeCl_2 \cdot 4H_2O$, Δbfe, and ΔmtrC/omcA. In the case of WT MR-1 OCPS were recorded using both 57:43 8OH:8COOH and 100% 8OH SAM modified Au wire electrodes. OCPs were recorded once they had become stable. At the start of an experiment the OCP drifts in one direction until reaching a point of relative stability. The means were calculated from n values >= 3, except for ΔmtrC/omcA and Δbfe where only two repeats had been conducted and MR-1 + Fe, which had only been tried once. Displayed alongside the means are the maximum variations between repeats given as a range. 8OH refers to SAMs formed using 1 mM 100% 8-mercapto-1-octanol. 8OH:8COOH refers to SAMs formed using a 1 mM 57:43 mix of 8-mercapto-1-octanol: 8-mercapto-1-octanoic acid.

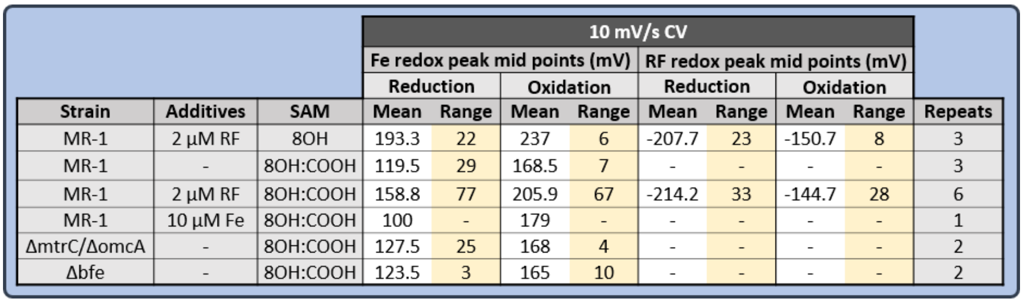

			10 mV/s CV								
			Fe redox peak mid points (mV)				RF redox peak mid points (mV)				
			Reduction		Oxidation		Reduction		Oxidation		
Strain	Additives	SAM	Mean	Range	Mean	Range	Mean	Range	Mean	Range	Repeats
MR-1	2 µM RF	8OH	193.3	22	237	6	-207.7	23	-150.7	8	3
MR-1	-	8OH:COOH	119.5	29	168.5	7	-	-	-	-	3
MR-1	2 µM RF	8OH:COOH	158.8	77	205.9	67	-214.2	33	-144.7	28	6
MR-1	10 µM Fe	8OH:COOH	100	-	179	-	-	-	-	-	1
ΔmtrC/ΔomcA	-	8OH:COOH	127.5	25	168	4	-	-	-	-	2
Δbfe	-	8OH:COOH	123.5	3	165	10	-	-	-	-	2

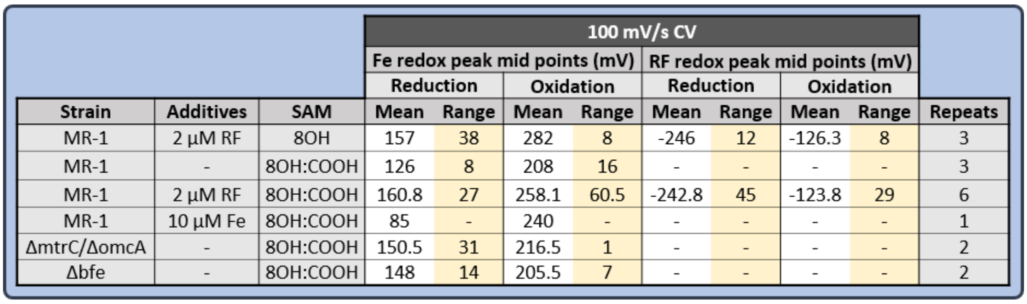

			100 mV/s CV								
			Fe redox peak mid points (mV)				RF redox peak mid points (mV)				
			Reduction		Oxidation		Reduction		Oxidation		
Strain	Additives	SAM	Mean	Range	Mean	Range	Mean	Range	Mean	Range	Repeats
MR-1	2 µM RF	8OH	157	38	282	8	-246	12	-126.3	8	3
MR-1	-	8OH:COOH	126	8	208	16	-	-	-	-	3
MR-1	2 µM RF	8OH:COOH	160.8	27	258.1	60.5	-242.8	45	-123.8	29	6
MR-1	10 µM Fe	8OH:COOH	85	-	240	-	-	-	-	-	1
ΔmtrC/ΔomcA	-	8OH:COOH	150.5	31	216.5	1	-	-	-	-	2
Δbfe	-	8OH:COOH	148	14	205.5	7	-	-	-	-	2

Tables 4.2. Tables comparing redox peak potentials (vs SHE) associated with redox signals assigned to iron (Fe) species and riboflavin (RF) from 10 mV/s (**TOP**) and 100 mV/s (**BOTTOM**) cyclic voltammograms. Displayed alongside the means are the maximum variations between repeats given as a range. Experiments displayed were carried out using WT MR-1, with and without added 2 µM riboflavin or 10 µM $FeCl_2 \cdot 4H_2O$, Δbfe, and ΔmtrC/omcA. In the case of WT MR-1 CV were recorded using both 57:43 8OH:8COOH and 100% 8OH SAM modified Au wire electrodes. CVs were recorded multiple times throughout each repeat. The means were calculated from n values >= 3, except for ΔmtrC/omcA and Δbfe where only 2 experiments had been conducted and MR-1 + Fe, which had only been tried once. 8OH refers to SAMs formed using 1 mM 100% 8-mercapto-1-octanol. 8OH:8COOH refers to SAMs formed using a 1 mM 57:43 mix of 8-mercapto-1-octanol: 8-mercapto-1-octanoic acid.

After ~60 minutes from loading the samples, videos were recorded in parallel to a chronoamperometry program, to gather data on the response of different MR-1 strains (WT, ΔmtrC/ΔomcA, Δbfe) to relevant applied potentials, and in the case of WT, the effects of adding 2 µM riboflavin or 10 µM $FeCl_2{\cdot}4H_2O$. Except for WT MR-1 with added Fe, all experiments were repeated for reproducibility. Specifically, experiments of WT MR-1 without riboflavin were repeated three times, experiments of WT MR-1 with riboflavin were repeated six times and experiments using the mutant stains were repeated twice (**Tables 4.1** & **4.2**). Each repeat used a completely new set-up and the bacteria samples were grown using a single colony from a fresh plate (<= 3 days old). Because variation in the bacterial motility can be high between repeats the analysed data from the WT + Fe videos is not reported here due to the absence of any repeats. Ideally, if time permitted, more repeats of each experiment would be carried out. Video microscopy experiments with the mutants were only carried out twice per mutant and the results obtained were consistent between repeats.

Once videos had been processed using the tracking algorithm described in **scheme 4.3**, the resultant traced trajectories could be processed further to remove effects from non-motile bacteria before calculating the average and instantaneous velocities from the trajectories or simplifying each trajectory into vectors using their start and end points. Once in vector form, the overall direction and magnitude (distance travelled) relative to the electrode can be calculated for each trajectory. After obtaining a selection of desired parameters from each trace the available area for which bacteria can move through was segmented into a series of zones according to distance from the electrode surface. The range of distances covered by each zone (i.e. the thickness) was kept equal for all zones. In **figure 4.10** the zones have been highlighted for one experiment. This enables plotting of variables, such as average bacterial velocity against the distance from the electrode, to visualise any potential relationships dependant on the bacteria's proximity to the electrode. Other parameters of interest, for example directional bias of the bacterial movement, can be compared over time in relation to an applied potential.

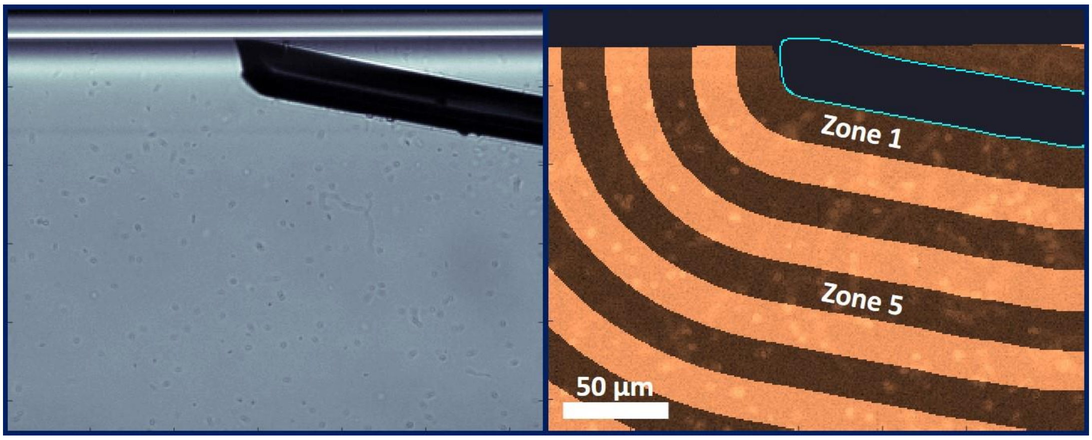

Figure 4.10. The image on the **LEFT,** is a representative frame of a capillary cell video experiment. On the **RIGHT** is a graphical representation of how the area is separated into the 10 zones used to divide data, derived from either traces or Shannon entropy, according to the origin distance from the electrode surface (highlighted in teal). Zone 1 and 5 are used in the time traces of **figures 4.12 + 4.13**.

To visualise the relationship between bacterial velocity and motile population density with respect to location heat maps were generated using two different intensity factors, the mean velocity and the normalised sum of velocities. The mean velocity as the intensity factor allows one to visualise the distribution of bacterial velocities around the electrode, while the normalised sum of velocities indicates both velocity and motile population density.

The normalised sum of bacterial velocities is calculated using the sum of velocities from all the bacteria traveling through an area, over a set duration, which is then normalised to a specified area (1 μm^2). Each bacterial velocity is calculated as the mean velocity from the bacteria's traced trajectory. Alternatively, one can use the sum of instantaneous velocities (i.e. the velocity of bacteria between consecutive frames) for a higher resolution result. The normalised sum of bacterial velocities can be viewed as a measure of motile activity from bacteria over an area directly comparable to other areas of various sizes.

Where video tracking experiments are reported in the literature it is common to see both traces obtained algorithmically and manually (for shorter durations). This way the accuracy of the algorithm can be checked. Manual tracking is also useful for measuring the frequency of certain behaviours such as changing direction, i.e. reversing and forward-reverse-flick in the case of MR-1. The identification of reversals and forward-reverse-flicks requires very accurate traces of a high time resolution and is highly sensitive to any artefacts arising from automated tracking algorithms. In the experiments carried out here, each video consists of

>= 48,000 frames, and each frame can have hundreds of motile bacteria alongside > 1,000 stationary bacteria, making manual tracking impractical for obtaining quantitative results regarding the frequency of direction changes. Even manual tracking for short periods of time would be an issue due to the number of bacteria per frame, thus manual tracking to form traces in a quantitative manner was not undertaken. Instead, the videos were watched alongside the automatically generated traces to check that the bacterial swimming paths, as determined by eye, overlap with the traces formed by automatic tracking. With the original algorithm it was observed that the high velocity bacteria were not being tracked. This was a major incentive for developing the custom algorithm, as discussed in the experimental development section. With the custom algorithm these high velocity bacteria were tracked along with most bacteria that were relatively close to the focal plane. By eye it was possible to see trajectories of out of focus bacteria that could not be traced by the algorithm and to follow bacteria beyond their automatically generated trajectories. It was also possible to observe, by eye, phenomena that the automatic tracking could not pick up. For example, at the surface of the electrode bacteria would frequently stick transiently to the electrode surface and ‘wiggle’. This behaviour was exacerbated during oxidative potentials (> -0.1 V vs SHE). Surface phenomena was ‘invisible’ to the tracking algorithm due to the requirement of masking the electrode to prevent false positive locations due to visual artefacts related to the light reflecting of the gold electrode surface. Overall the algorithm used here tracks MR-1 to an acceptable standard for abstracting variables such as bacterial velocity and average swimming direction. Individual bacterial behaviours such as reverse and forward reverse flick are also clearly present in the tracked trajectories (**figure 4.11**).

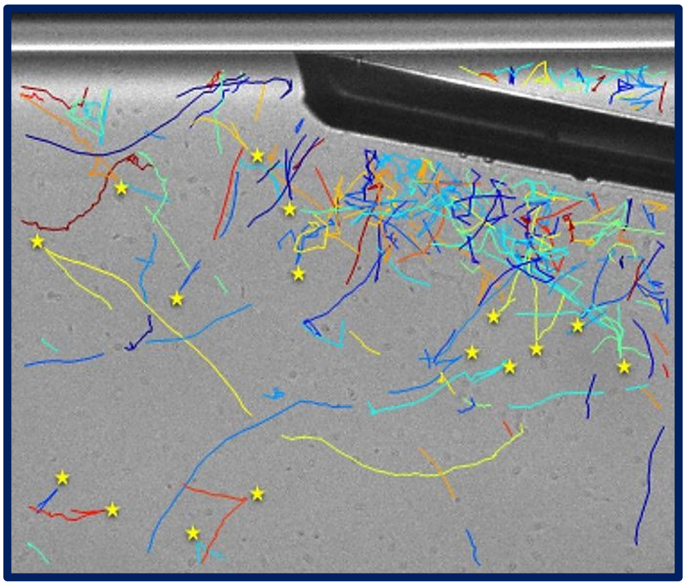

Figure 4.11. Coloured traces represent tracked WT MR-1 over a period of 10 seconds from the application of an applied potential of -0.3 V (SHE). Yellow stars represent a proportion of direction changes resulting from reversals or flicks. Traces are coloured according to their swimming direction in relation to the electrode Red and orange represent traces of bacteria moving in the general direction of the electrode, with dark red being the most direct. Blue represents traces of bacteria moving away from the electrode, with dark blue for the most direct traces. Green and yellow are swimming roughly in parallel with the electrode.

Shannon's entropy

As an alternative to manual tracking for validating the tracking algorithm, videos were analysed using an unrelated processing method. The alternative method is based on Shannon's entropy which does not rely on tracking bacterial trajectories. Thus, it does not require the identification of bacterial locations or linking up of possible trajectories, all of which can be biased depending on the tracking algorithm used. Instead, the method simply calculates a value for each pixel in the video, based on the pixel's intensity fluctuations over a specified duration, representing the degree of uncertainty for each pixel. The value calculated is known as the Shannon entropy which can be applied to any probabilistic distribution and has previously been used in the analysis of time series data in numerous fields including meteorology, ecology, astronomy, and most importantly bacterial population motility by Nisenbaum *et al* [148]. A summary of how the videos were processed using Shannon entropy can be viewed in **scheme 4.4**. For the videos recorded here two factors are primarily responsible for variations in a pixel's intensity which are pixel noise and movement of some contrasting image features, such as a bacterium. Therefore, the

Shannon entropy value for pixels in areas of high bacteria movement will be higher than areas of low or no movement. Assuming the tracking method is relatively accurate, one would expect a good correlation between the average Shannon entropy value (determined in part by bacterial motility) and the number of motile (> 4 µm/s) bacteria per area (motile population density) for the same area, calculated using the trajectories formed by the tracking algorithm. For comparison, graphs of Shannon entropy have been placed alongside graphs of motile bacteria population density (**figure 4.12 & 4.13**). Qualitatively identical results were obtained using either measure for bacterial motility either directly by analysing the automatically tracked results or indirectly from the Shannon entropy. Agreement between results obtained from trajectories and an independent processing method which was previously verified suggests the trajectories obtained here, by the custom algorithm, are valid.

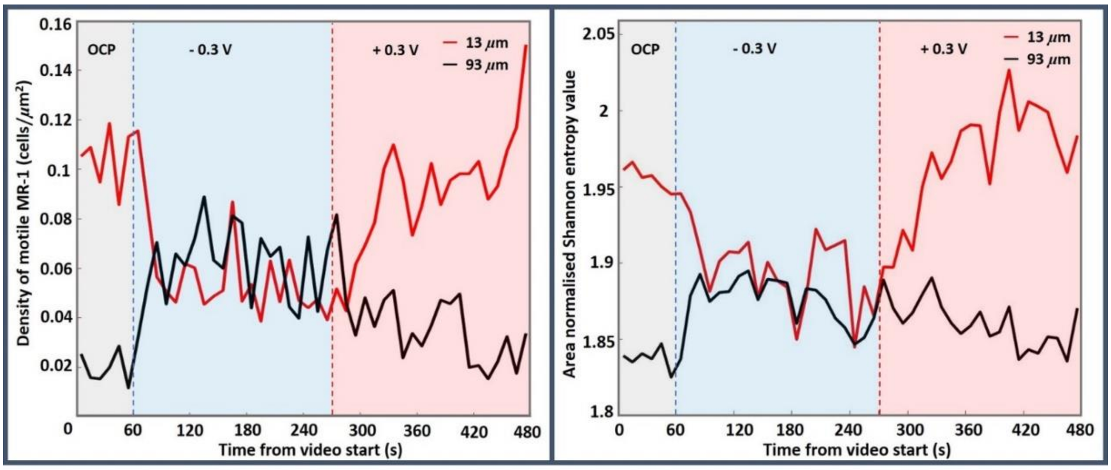

Figure 4.12. Time traces of the mean Shannon entropy (**RIGHT**) and MR-1 motile population density (**LEFT**) from two spatially localised zones out of a total of 10 zones. The Shannon entropy of each pixel was calculated using 10 s (~100 frame) intervals. The motile population density was calculated from the number of motile bacteria counted for a zone and divided by that zones area. If the bacteria's mean velocity is >= 4 µm/s then it is counted as motile. The zones are separated according to their distance to the electrode, each representing a range of roughly 20 µm. The **red** trace represents the first zone (zone 1) and is closest to the electrode with a mean distance of 13 µm from the electrode surface. The **black** trace represents zone 5, at a mean distance of 93 µm from the electrode surface. The video was taken after ~90 min from loading the capillary with MR-1 suspension and sealing the entrances with silicon grease. The suspension consists of WT MR-1 in anaerobic growth media, diluted 5-fold with MOPS buffer and supplemented with 50 mM lactate and 2 µM riboflavin. In parallel to the video, the potentiostat cell was left 'off' with an OCP of -0.18 V for the first 60 s prior to an applied potential of -0.3 V for 210 s, followed by +0.3 V for 210 s.

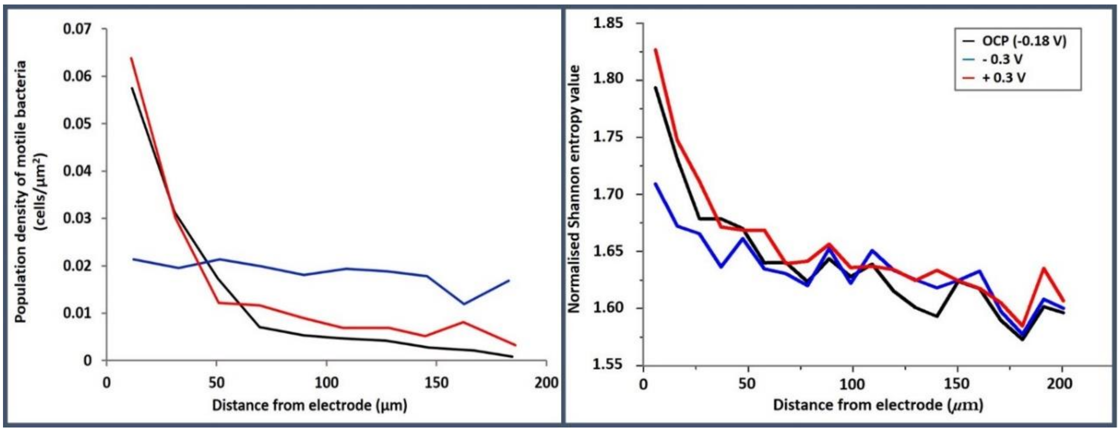

Figure 4.13. Graph of the mean Shannon entropy (**RIGHT**) and MR-1 motile population density (**LEFT**) against distance from the electrode. The Shannon entropy of each pixel was calculated using 2 s (~20 frame) intervals. The video frames are separated into zones according to their distance to the electrode, each representing a range of roughly 20 µm. The video was taken ~ 90 min from loading the capillary with WT MR-1 suspension and sealing the entrances with silicon grease. The suspension consists of WT MR-1 in anaerobic growth media, diluted 5-fold with MOPS buffer and supplemented with 50 mM lactate and 2 µM riboflavin. In parallel to the video, the potentiostat cell was left off for the first 60 s prior to an applied potential of -0.3 V for 210 s, followed by +0.3 V for 210 s. **Blue** lines represent the last 60 s of a 210 s period with an applied potential of -0.3 V. **Red** lines represent the last 60 s of a 210 s period with an applied potential of +0.3 V. **Black** lines represent 60 s with the cell off (no applied potential).

From the plots of motile bacteria population density against distance from the electrode in **figure 4.13**, one can observe an increase in the number of motile bacteria per area while approaching the electrode during potentials above a certain threshold. This dependence on proximity to the electrode is dramatically reduced as seen by both measures (Shannon entropy and motile bacteria per area), after switching the potential to a relatively low (reducing) potential of -0.3 V (SHE). Heat-maps of the same experiment are displayed in **figure 4.14**, coloured according to average velocity and the normalised summed velocity. The heat-maps representing average velocity show that, in addition to an increase in the overall population of motile bacteria with proximity to the electrode, the average velocity of the swimming bacteria also increases on approach to the electrode at relatively positive (oxidative) potentials.

In general, the entropy and population density of motile bacteria (> 4 µm/s) follow similar trends with respect to distance from the electrode, but as one can see in **figure 4.13** there are areas where the two measures diverge. For example, close to the electrode surface (< 40 µm) an upward inflection is observable for both the entropy and MR-1 motile population density at positive (+0.3 V) and open circuit potentials (-0.18 V), whilst at negative potentials (-0.3 V) the inflection for motile bacteria density is abolished whereas the inflection for entropy only decreases but is still present. For most experiments the electrode rests on one of the capillary inner side walls. At this region, the glass is curved which effects the local illumination and, in the case of **figure 4.11 or 4.10**, has resulted in a bright band extending predominantly into the area around the electrode. As mentioned above, the Shannon entropy value for a pixel is determined by variations in the pixels intensity. The magnitude of a pixel's intensity variations is affected by the base level of illumination it receives. Thus, the persistent inflection in entropy, present to a degree even during the negative potential (-0.3 V), could be an artefact introduced by uneven illumination. An additional difference between the two measures can be seen in the mid to long distance region (> 50 µm), where the entropy stays relatively constant between the different potentials but the motile bacterial population density significantly rises in this region on switching to a negative (-0.3 V) potential.

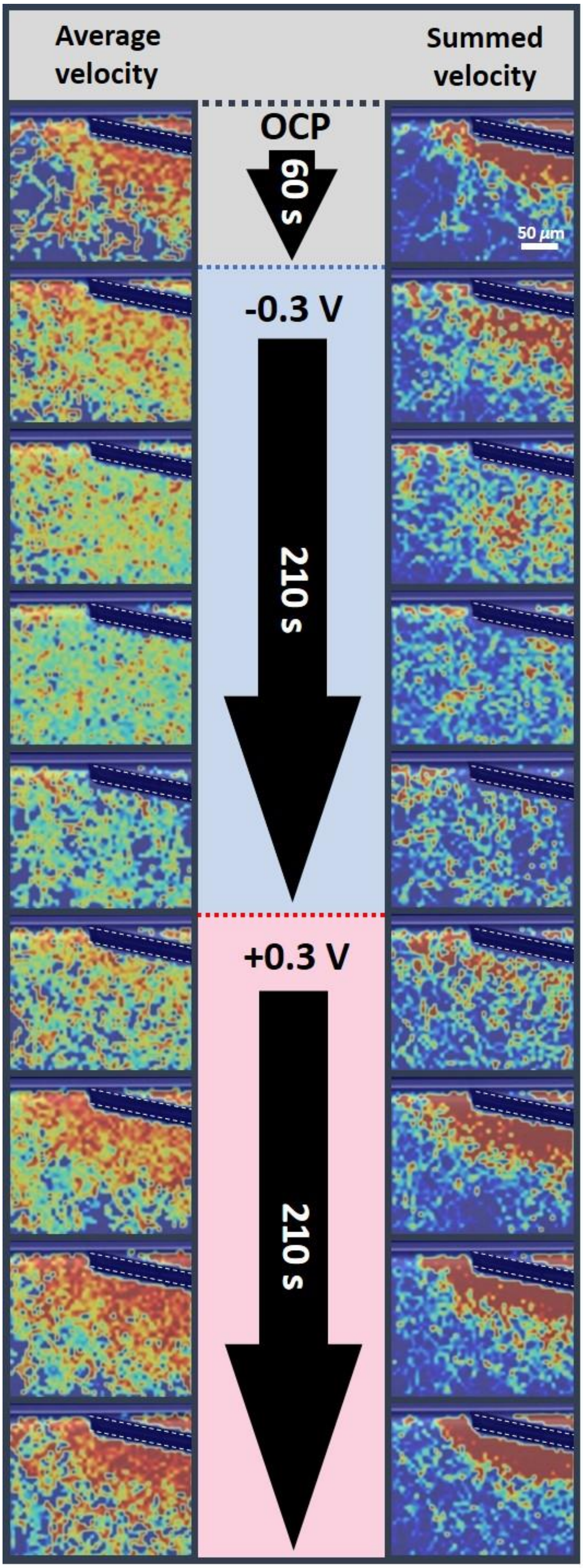

Figure 4.14. Heat maps using two different measures of MR-1 motility to present the changes in motile activity over a period of 8 minutes, during changes in the applied potentials. Heatmaps created using a jet colour scheme, overlaid onto a representative greyscale frame from the video. The colormap of heat maps on the left side is scaled according to MR-1 average motility (low-lim = 0, high-lim = 30 *µm/s*), while that of the right is scaled according to the normalised summed velocity (low-lim = 0, high-lim = 1.67 $\Sigma(\mu m/s)/min/\mu m^2$). Dotted white lines highlight the electrode edges. The video was taken after >60 min from loading the capillary with MR-1 suspension and sealing the entrances with silicon grease. The suspension consists of WT MR-1 in anaerobic growth media, diluted 5-fold with MOPS buffer and supplemented with 50 mM lactate and 2 µM riboflavin. In parallel to the video, the potentiostat cell was left off with a OCP of -0.18 V for the first 60 s prior to an applied potential of -0.3 V for 210 s, followed by +0.3 V for 210 s.

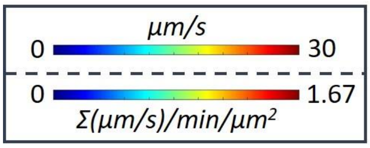

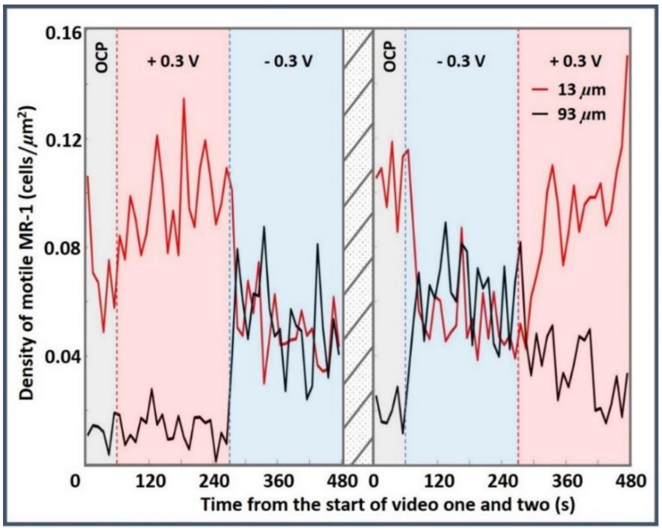

Figure 4.15. Time traces of the MR-1 motile population density from two spatially localised zones out of a total of 10 zones. The zones are separated according to their distance to the electrode, each representing a range of roughly 20 μm. The **red** trace represents the first zone (zone 1) and is closest to the electrode with a mean distance of 13 μm from the electrode surface. The **black** trace represents zone 5, at a mean distance of 93 μm from the electrode surface. The traces are spread over two consecutive videos, the second video was taken ~30 min after the end of the first video (due to the time taken to save the first video). The first video was taken after 40-60 min from loading the capillary with MR-1 suspension and sealing the entrances with silicon grease (allowing MR-1 time to consume any remaining dissolved oxygen and adapt to the new conditions). The suspension consists of WT MR-1 in anaerobic growth media, diluted 5-fold with MOPS buffer and supplemented with 50 mM lactate and 2 μM riboflavin. During video 1, the potentiostat cell was left off with a OCP = -0.18 V for the first 60 s prior to an applied potential of +0.3 V for 210 s, followed by -0.3 V for 210 s. Video 2 also began with the cell off with a OCP = -0.18 V for 60 s, but was followed by an applied potential of -0.3 V before switching to +0.3 V.

Time traces for the zone closest to the electrode (3-23 μm) and a zone at mid distance (83 – 103 μm) form the electrode are compared in **figure 4.15 & 4.16**, using either motile population density or average Shannon entropy value as a measure of motile bacteria. The number of motile bacteria around the electrode suddenly drops when switching from an open circuit potential (OCP/cell off) of approximately -0.18 V to a relatively negative/reducing potential of -0.3 V at t = 60 s, while the activity in the mid distance zone increases. On watching the video, one can observe a high amount of highly motile MR-1 around the electrode during the open circuit potential and more positive potentials and a low number of motile bacteria further away from the electrode. When the potential is switched to a negative potential e.g. -0.3 V, the highly motile MR-1 close to the electrode moves away from the electrode, almost instantly. In doing so, the highly motile MR-1, pass through areas further away from the electrode that originally had very low levels of motile bacteria. In occurrence with the move array from the electrode but on a significantly longer timescale the velocity of the bacteria also decreases. This observation explains the decreases in motility close to the electrode and increase in motility further away from the electrode, seen in **figure 4.16**, on switching the potential to -0.3 V. On switching the potential back to a relatively positive potential (+0.3 V) the number of motile bacteria around the electrode rises again and, in the video, this is seen as a recovery in the motility of bacteria in the vicinity of the electrode and migration towards the electrode by bacteria further away from the electrode.

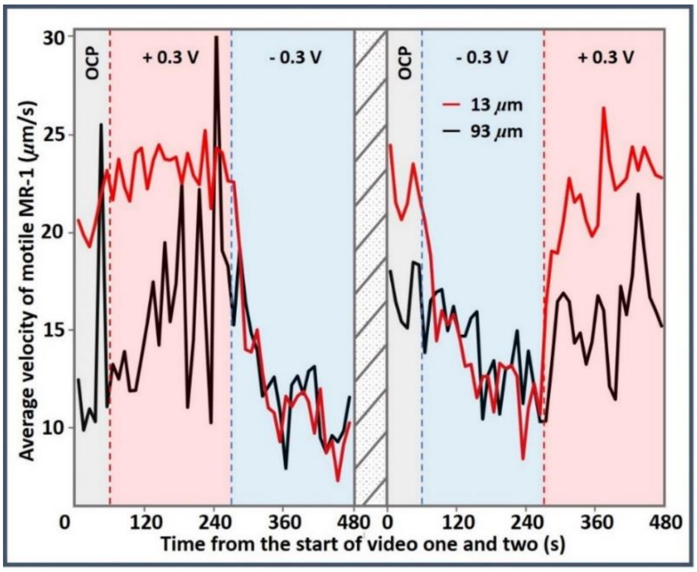

Figure 4.16. Time traces of MR-1 average/mean velocity from two spatially localised zones out of a total of 10 zones. The zones are separated according to their distance to the electrode, each representing a range of roughly 20 µm. The **red** trace represents the first zone (zone 1) and is closest to the electrode with a mean distance of 13 µm from the electrode surface. The **black** trace represents zone 5, at a mean distance of 93 µm from the electrode surface. The traces are spread over two consecutive videos, the second video was taken ~30 min after the end of the first video (due to the time taken to save the first video). The first video was taken after 40-60 min from loading the capillary with MR-1 suspension and sealing the entrances with silicon grease (allowing MR-1 time to consume any remaining dissolved oxygen and adapt to the new conditions). The suspension consists of WT MR-1 in anaerobic growth media, diluted 5-fold with MOPS buffer and supplemented with 50 mM lactate and 2 µM riboflavin. During video 1, the potentiostat cell was left off with a OCP = -0.18 V for the first 60 s prior to an applied potential of +0.3 V for 210 s, followed by -0.3 V for 210 s. Video 2 also began with the cell off with a OCP = -0.18 V for 60 s, but was followed by an applied potential of -0.3 V before switching to +0.3 V.

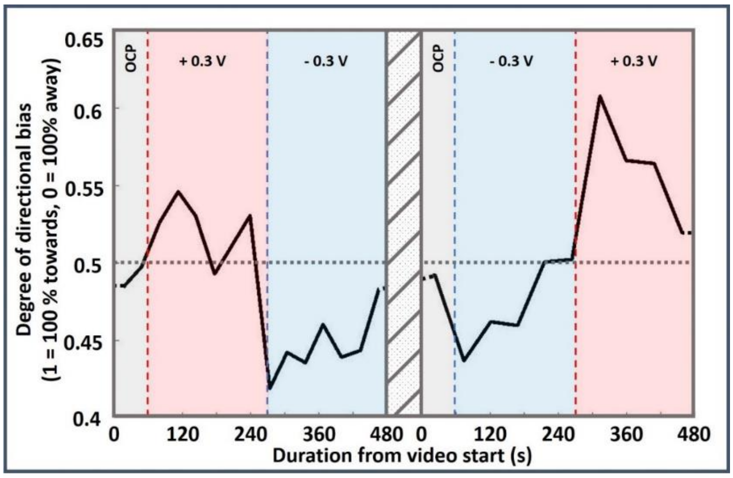

Figure 4.17. Time trace of bacterial directional bias with respect to the electrode over two consecutive videos with a gap of ~ 30 min between them (time taken to save the first video). The first video was taken after 40-60 min from loading the capillary with MR-1 suspension and sealing the entrances with silicon grease (allowing MR-1 time to consume any remaining dissolved oxygen and adapt to their new enviroment). The suspension consists of WT MR-1 in anaerobic growth media, diluted 5-fold with MOPS buffer and supplemented with 50 mM lactate and 2 µM riboflavin. Chronoamperometry regime consisted of 60s at OCP (-0.18 V) prior to an applied potential of +0.3 V for 210 s, followed by -0.3 V for 210 s. Video 2 began with the OCP (-0.18 V) for 60 s, followed by an applied potential of -0.3 V before switching to +0.3 V. Each point plotted, is the weighted mean of the direction travelled by bacteria relative to the electrode, expressed as a fraction, calculated from vectors of traces accumulated during the respective time period. The number of traces used to calculate each point varies from 211 to 773 traces, with a mean of 450.32.

As described above, Mr-1 is observed in the videos rapidly moving away from the electrode on switching from the OCP (-0.18 V) or positive (+0.3 V) potentials to negative potentials (-0.3 V), and this qualitative observation is also backed up by the time traces in **figure 4.12**. The is also a general decrease in all bacteria velocity as time progresses while applying a negative potential. Switching the potential to positive (+0.3 V) caused a gradual increase in bacterial velocity in the electrodes vicinity, parallel to a bias in direction of bacteria movement towards the electrode. As bacteria move closer towards the electrode their velocity also increases. Observations regarding directional bias of bacterial motility are confirmed by the quantitative data obtained from traces expressed as a fraction and plotted against time (**figure 4.17**). To reach a fraction representing the direction of travel for a bacterial trajectory relative to the electrode the traces were first converted into vectors using the co-ordinates of the trace beginning **A** and end **B**. The closest co-ordinate on the electrode surface **E** to the beginning co-ordinate **A** of each trace was then found and used to generate a second vector using the co-ordinates of **A** and **E**. The angle **α** at **A**, between vectors **AB** and **AE**, was then calculated and finally the angle turned into a fraction **f**, where **f = 1** when **α** = 0° and **f = 0** when **α** = 180°. After all the trajectories were assigned a fraction representing their overall direction of travel, relative to the electrode, the average movement direction representing all the bacteria in frame over a set duration was then calculated using this direction factor. Each direction factor was weighted according to the vectors magnitude (i.e. distance between start and finish point) prior to calculating the mean direction factor as used in **figure 4.17**.

The shift in bacterial velocities on changing the applied potential is evident in the velocity histograms, plotted for periods at no applied potential (OCP), along with periods at relatively positive (oxidative) and relatively negative (reducing) potentials (**figure 4.18 & 4.19**). For WT MR-1 without additional riboflavin, the mean velocities, for three different potentials plus the OCP (OCP = - 0.027 V), were 7.7 µm/s at −0.25 V, 11.8 µm/s at −0.15 V, 12.5 µm/s with the cell off, and 13.6 µm/s for +0.3 V. WT MR-1 samples with an additional 2 µM of riboflavin had substantially higher average velocities of 10.3, 17.3, and 20 µm/s for −0.3, OCP, and +0.3 V respectively.

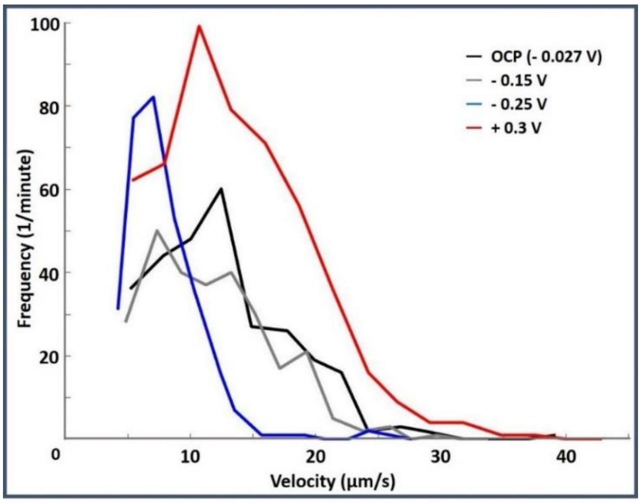

Figure 4.18. Histogram representing the distribution of bacterial swimming speeds above 4 µm/s. Each point constructed from trace counts over a duration of one minute, within the respective velocity ranges. The video was taken ~60 min from loading the capillary with WT MR-1 suspension and sealing the entrances with silicon grease. The suspension consists of WT MR-1 in anaerobic growth media, diluted 5-fold with MOPS buffer and supplemented with 50 mM lactate. During the video, the potentiostat cell was left off with OCP = -0.027 V for the first 60 s prior to an applied potential of -0.15 V for 60 s followed by -0.25 V for 210 s, and then +0.3 V for the remaining 210 s. The bacterial velocities were calculated as the mean velocity over each complete trace (total trace length divided by the duration of each trace). The mean population velocity for the different periods are; OCP (-0.027 V) = 12.6 µm/s, -0.15 V = 11.8 µm/s, -0.25 V = 7.7 µm/s, +0.3 V = 13.6 µm/s. For the modes; OCP (-0.027 V) = 7.8 µm/s, -0.15 V = 7.3 µm/s, -0.25 V = 7.0 µm/s, +0.3 V = 10.7 µm/s.

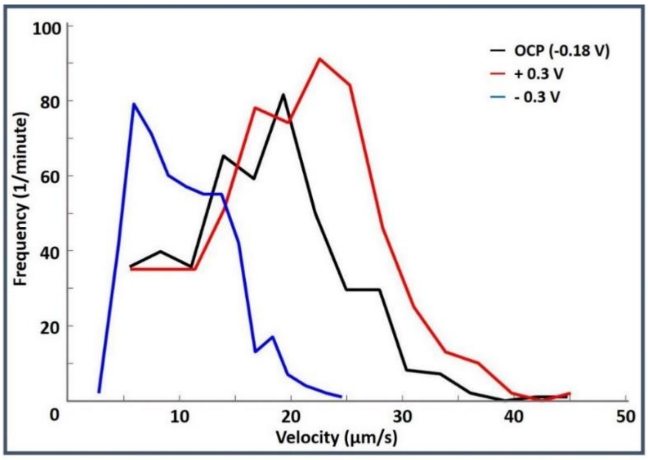

Figure 4.19. Histogram representing the distribution of bacterial swimming speeds above 4 µm/s. Each point constructed from trace counts over a duration of one minute, within the respective velocity ranges. The video was taken ~60 min from loading the capillary with WT MR-1 suspension and sealing the entrances with silicon grease. The suspension consists of WT MR-1 in anaerobic growth media, diluted 5 fold with MOPS buffer and supplemented with 50 mM lactate and 2 µM riboflavin. During the video, the potentiostat cell was left off with OCP = -0.18 V for the first 60 s prior to an applied potential of +0.3 V for 210 s followed by -0.3 V for the remaining 210 s. The bacterial velocities were calculated as the mean velocity over each complete trace (total trace length divided by the duration of each trace). The mean population velocity for the different periods are; OCP (-0.18 V) = 17.3 µm/s, +0.3 V = 20.0 µm/s, -0.3 V = 10.3 µm/s. For the modes; OCP (-0.18 V) = 19.3 µm/s, +0.3 V = 22.6 µm/s, -0.3 V = 5.9 µm/s.

By applying a series of potentials, whilst measuring the bacterial response through quantifiable parameters (bacterial velocity and direction), one can identify the potential at which the change in bacterial behaviours occurred and if the change in behaviour is gradual or abrupt. The shift in behaviour occurred suddenly between -0.25 and -0.15 V for WT MR-1, with or without added riboflavin. For MR-1 with riboflavin, the window where the change occurred could be narrowed further by considering OCPs, as seen in the heat-maps of **figure 4.20**, where the change occurs between -0.25 V and -0.205 V. As discussed later, the range between -0.25 and -0.15 V is significant in relation to the hypothesis on flavins role in MR-1 taxis towards insoluble electron acceptors, because it coincides with the potential region where the midpoint potential for riboflavin is located.

As described above, **figures 4.15** & **4.16** represents time traces of MR-1 motile population density (**4.15**) and average velocity (**4.16**), over two consecutive videos. Both **4.15** and **4.16** represent the same experiment and compare the area closest to the electrode surface (zone 1, representing 3 – 23 µm from the electrode surface) with a mid-distance area (zone 5, representing 83 – 103 µm). By zone 5 the number of motile bacteria is relatively low, thus the 'n' values for calculating the means are also low. Mean values calculated using small 'n' values are associated with high uncertainty which manifests as noise when plotted (as can be seen in **4.16**). The high noise level, in the average velocity trace of zone 5, makes it difficult to establish a valid relationship with regards to the effect of switching potential on bacterial velocity for this zone. Taking into account the noise, the average velocity does appear to rise gradually in zone 5, with high potentials (+0.3 V) and decrease on applying negative potentials (-0.3 V) whilst at zone 1, the average velocity is affected significantly with changing potentials. From a positive potential (+0.3 V) or OCP (-0.18 V), the average velocity decreases by approximately half within one minute from switching to a negative potential (-0.3 V). On applying a positive potential, the average velocity returns to its original velocity.

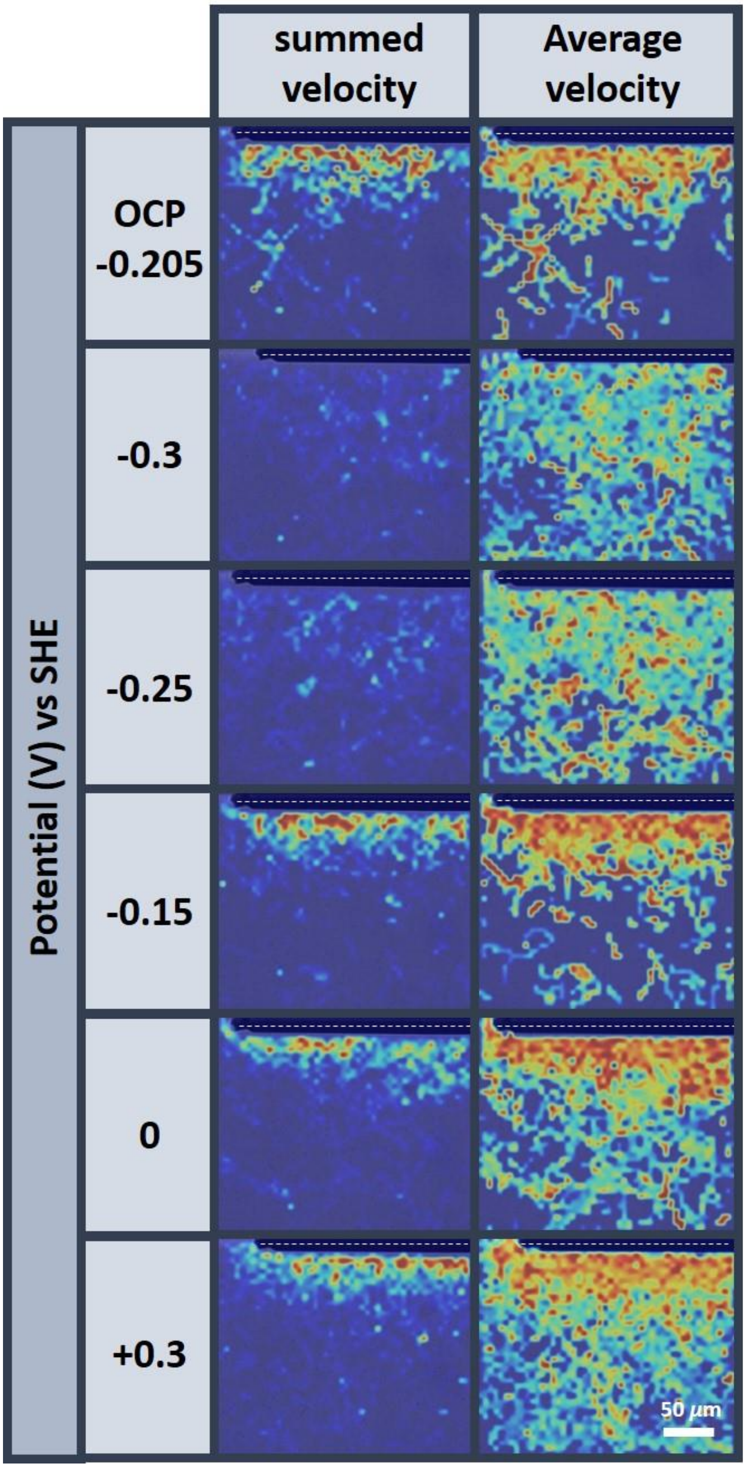

Figure 4.20. Heat maps using two different measures of MR-1 motility to present the changes in motile activity at a range of applied potentials. Heatmaps created using a jet colour scheme, overlaid onto a representative greyscale frame from the video. The colormap of heat maps on the left side is scaled according to the normalised summed velocity (low-lim = 0, high-lim = 1.67 $\Sigma(\mu m/s)/min/\mu m^2$), while that of the right is scaled according to MR-1 average motility (low-lim = 0, high-lim = 30 $\mu m/s$). Dotted white lines highlight the electrode edges. Videos taken after >60 min from loading MR-1 suspension and sealing the entrances with silicon grease. The suspension consists of WT MR-1 in anaerobic growth media, diluted 5-fold with MOPS buffer and supplemented with 50 mM lactate and 2 μM riboflavin. In parallel to the videos, the potentiostat cell was left off with a OCP of -0.205 V for the first 60 s prior to applied potential including -0.3, -0.25, -0.15, 0, and +0.3 V.

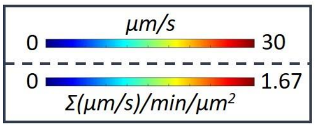

Mutants

In addition to WT MR-1, two mutant stains were also evaluated, the double ΔmtrC/ΔomcA deletion strain LS784 (severely deficient in EET) and the Δbfe deletion strain [107]. bfe stands for bacterial flavin adenine dinucleotide exporter and the Δbfe strain is severely deficient in extracellular flavin secretion. Results obtained using *ΔmtrC/ΔomcA*, suggest the EET pathway is important for tactic responses towards insoluble electron acceptors. Similar results have been previously reported in the literature using different EET deficient mutants. For example, Harris *et al* [132] reported that a *ΔcymA* deletion mutant (deficient in EET) failed to respond to a carbon fibre electrode poised at +0.7 V (Ag/AgCl) or to MnO_2 particles, whereas WT MR-1 responded to both.

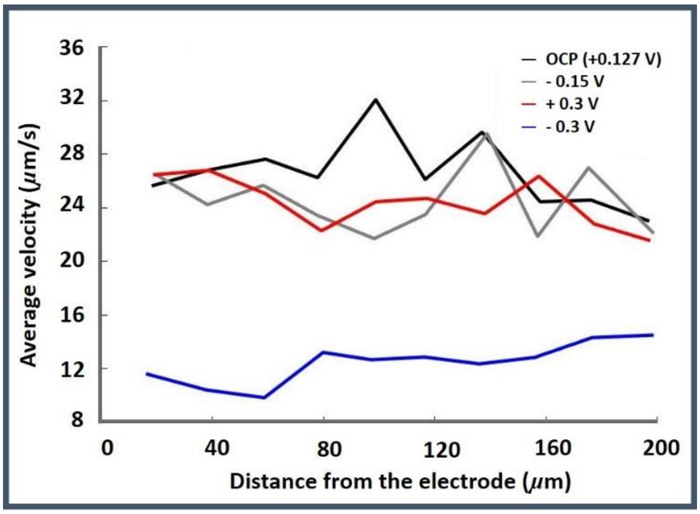

Figure 4.21. Graph of the mean velocity from ΔmtrC/ΔomcA swimming above 4 μm/s, against distance from the electrode (anything recorded below 4 μm/s, is assumed to be not moving by its own accord). Each point on the graph is calculated from the traces, passing through the respective zone for one minute. Each zone is within a set distance range from the electrode. The video was taken as soon as possible (~15 min) from loading the capillary with ΔmtrC/ΔomcA suspension and sealing the entrances with silicon grease. At the time the video was taken a large fraction of the bacteria is highly mobile, probably due to an aerokinetic response by the bacteria to the remaining dissolved oxygen in the capillary. The suspension consists of ΔmtrC/ΔomcA strain in anaerobic growth media, diluted 5-fold with MOPS buffer and supplemented with 50 mM lactate. During the video, the potentiostat cell was left off with OCP = +0.127 V for the first 60 s prior to an applied potential of -0.15 V for 60 s followed by +0.3 V for 210 s, and switching to -0.3 V for the remaining 210 s.

ΔmtrC/ΔomcA (LS784)

High motility was observed with the *ΔmtrC/ΔomcA* strain within the initial 15 minutes after loading into the capillary cell, but there was no relationship between velocity or population density with distance to the electrode and all motility rapidly declined to almost zero after 60 minutes. During a video experiment conducted within the first 15 minutes, on the application of an oxidative potential (+0.3 V), no effect was observed, but on applying a reducing potential (-0.3 V), a significant decline in the average bacterial velocity was observed (**figure 4.21**), with a possible negative relationship with distance from the electrode. At -0.3 V, dissolved oxygen is reduced into water, thus it is possible that a negative concentration gradient of dissolved oxygen is established around the electrode, leading to the observed decrease in velocity around the electrode. Heat maps in **figure 4.23**, illustrate the even spread of high velocities during the first 15 minutes. This is in contrast with the heat maps from other strains (**figures 4.14, 4.20 & 4.27**) where a clear dependency with proximity to the electrode can be seen. It should be also noted that no directional bias was observed (**figure 4.22**).

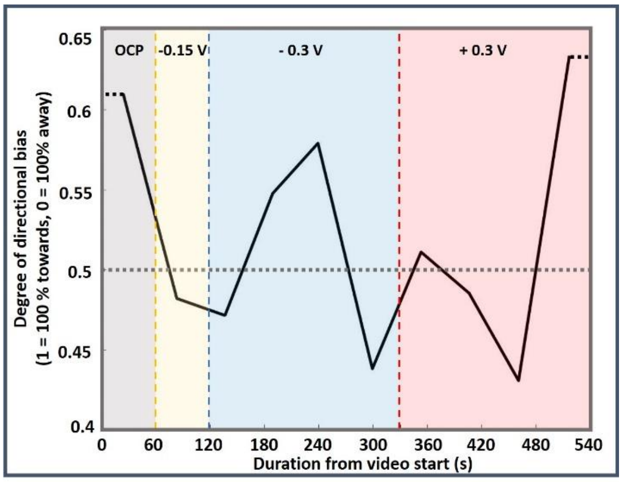

Figure 4.22. Time trace of bacterial directional bias with respect to the electrode against time. Video taken 60 min from loading the capillary with *ΔmtrC/ΔOmcA* suspension and sealing the entrances with silicon grease. The suspension consists of *ΔmtrC/ΔomcA* in anaerobic growth media, diluted 5 fold with MOPS buffer and supplemented with 50 mᴍ lactate. Chronoamperometry regime consisted of OCP = +0.054 V for the first 60 s prior to an applied potential of -0.15 V for 60 s followed by -0.3 V for 210 s, and then +0.3 V for the remaining 210 s. Each point plotted, is the weighted mean of the direction travelled by bacteria relative to the electrode, calculated as described for **figure 4.17**. The number of traces used to calculate each point varies from 35 to 67 traces, with a mean of 51.8.

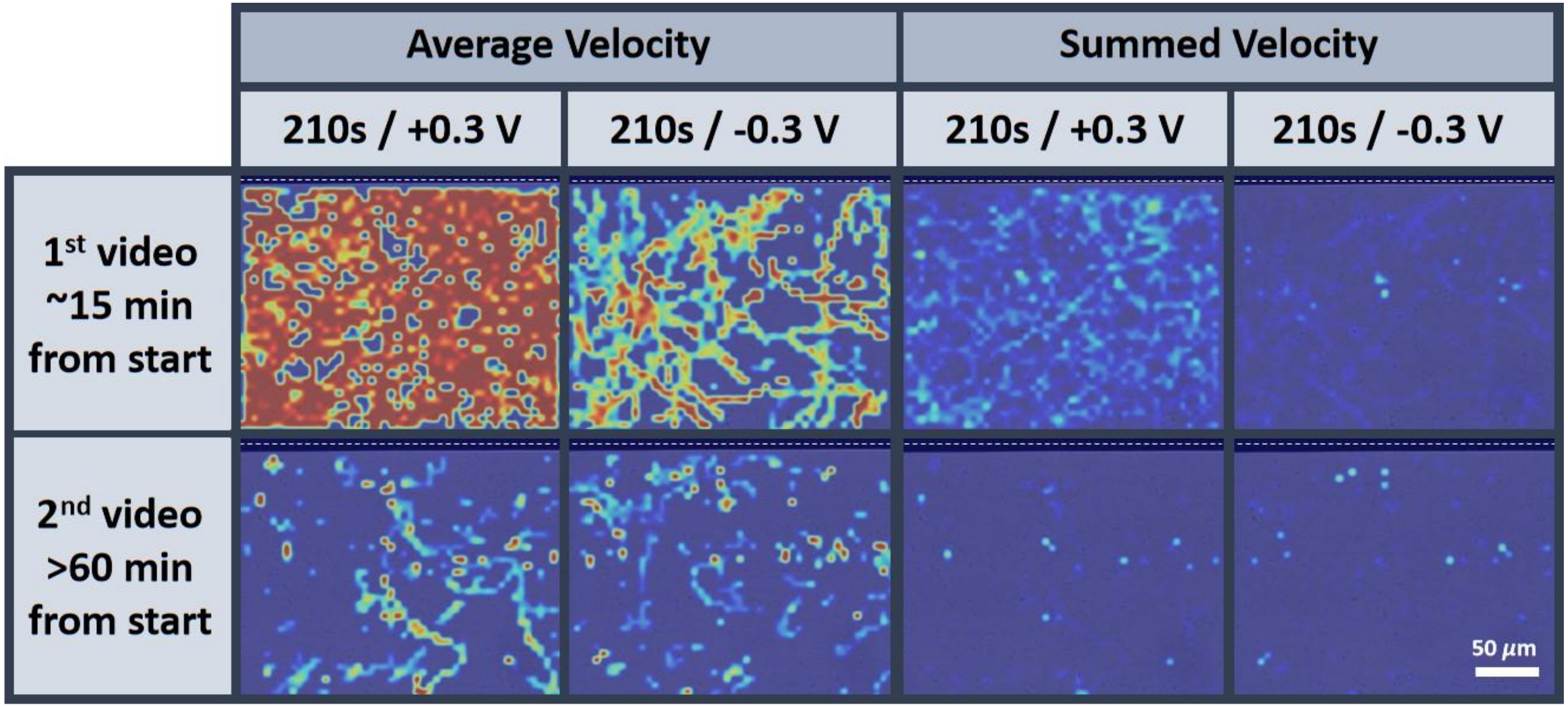

Figure 4.23. Heat maps representing ΔmtrC/ΔomcA motility in videos taken ~15 and 65 minutes from sealing the capillary cell, using two different applied potentials (+0.3 & -0.3 V). Heatmaps created using a jet colour scheme, overlaid onto a representative greyscale frame from the respective video. The colormap is scaled according to average velocities (low-lim = 0, high-lim = 30 *μm/s*) on the left and normalised summed velocity (low-lim = 0, high-lim = 1.67 $\Sigma(\mu m/s)/min/\mu m^2$) on the right. Dotted white lines highlight the electrode edges. The suspensions contained ΔmtrC/ΔomcA in anaerobic growth media, diluted 5-fold with MOPS buffer and supplemented with 50 mM lactate. In parallel to the video, the potentiostat cell was left off for the first 60 s prior to an applied potential of +0.3 V for 210 s, followed by -0.3 V for 210 s.

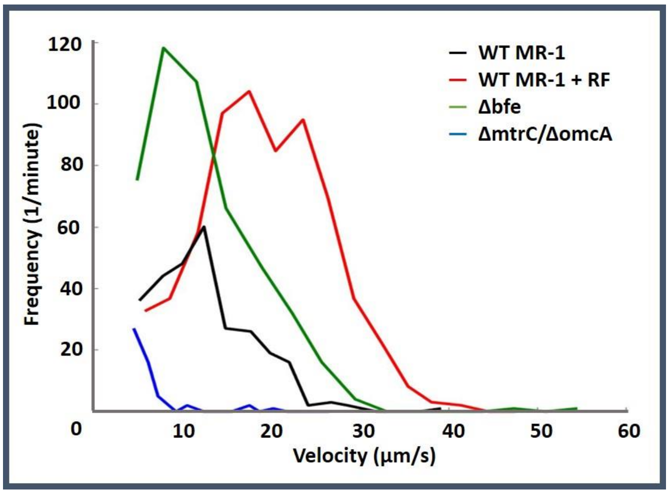

Figure 4.24. Histogram representing the distribution of bacterial swimming speeds above 4 μm/s. Each point constructed from trace counts over a duration of one minute, within the respective velocity ranges. The videos were taken ~60 min from loading the capillary with WT MR-1 suspension and sealing the entrances with silicon grease. The suspension consist of either WT MR-1, *Δbfe*, or *ΔmtrC/ΔomcA* in anaerobic growth media, diluted 5 fold with MOPS buffer, supplemented with 50 mM lactate and in the case of one of the two suspensions containing WT MR-1, 2 μM riboflavin (RF). During the one minute for which the histograms represent, the potentiostat cell was left off. The bacterial velocities were calculated as the mean velocity over each complete trace (total trace length divided by the duration of each trace). The mean population velocity for the different experiments are; WT MR-1 with RF = 19.3 μm/s, WT MR-1 = 12.6 μm/s, *Δbfe* = 12.4 μm/s, *ΔmtrC/ΔomcA* = 6.3 μm/s. For the modes; WT MR-1 with RF = 17.6 μm/s, WT MR-1 = 12.5 μm/s, Δbfe = 7.9 μm/s, *ΔmtrC/ΔomcA* = 4.5 μm/s.

Figure 4.24 compares the velocity histogram of *ΔmtrC/ΔomcA* with histograms from the other MR-1 strains, all from videos after >60 minutes from loading. Here it is evident that motility above 4 μm/s is minimal in the *ΔmtrC/ΔomcA* strain. The was no directional bias in motility, relative to the electrode on switching potentials between +0.3 and -0.3 V, observed in videos taken at 15 or >60 minutes from loading the sample (**figure 4.22**), unlike with WT MR-1 (**figure 4.17**). The fluctuations in directional bias throughout the experiment centred around 0.5 (no bias), showed no correlation with the applied potentials. The relatively large fluctuations are attributed to the increase in uncertainty due to reduced 'n' values (35 to 67) for each point plotted, compared with the same plot for WT MR-1 (N = 211 to 773). The low N values are because few bacteria are traveling at > 4 μm/s (i.e. considered moving on their own accord). *ΔmtrC/ΔomcA* effectively acts as a negative control strain, and this is exemplified in **figure 4.25**, comparing the population density of motile bacteria, with velocities > 4 μm/s, of all the stains tested at two different potentials (+0.3 V or <= -0.25 V).

The blue lines representing *ΔmtrC/ΔomcA* run flat along the bottom with no change between potentials (+0.3 V and -0.3 V). All other strains express a relationship between bacterial motility and proximity to the electrode which is depressed upon switching potentials to <= -0.25 V.

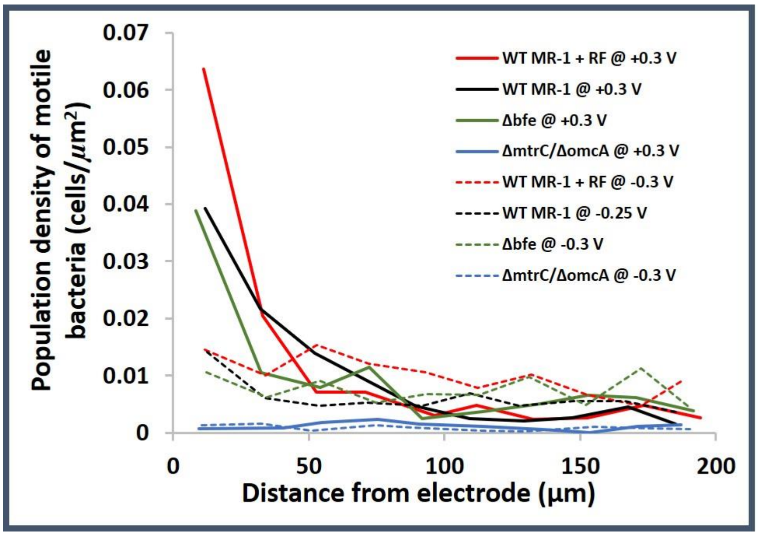

Figure 4.25. Graph of the normalised sum of velocities from bacteria swimming speeds above 4 µm/s against distance from the electrode. Each point on the graph is calculated from the accumulation of velocities (each velocity is calculated from a whole trace), over one minute, from the available area of a zone within a set distance range from the electrode. The videos were taken ~60 min from loading the capillary with WT MR-1 suspension and sealing the entrances with silicon grease. The suspensions consist of either WT MR-1 [with riboflavin = **red** | without = **black**], Δbfe [**green**], or ΔmtrC/ΔomcA [**blue**] in anaerobic growth media, diluted 5-fold with MOPS buffer, supplemented with 50 mM lactate and in the case of one of the two suspensions containing WT MR-1, 2 µM riboflavin (RF). During the one minute for which the data of each line was obtained, the potentiostat was set to apply an oxidative potential (+0.3 V) [represented by full lines —] or a reducing potential (-0.3 V or -0.2 V in the case of the suspension of WT and no added riboflavin) [represented by dotted lines ⋯].

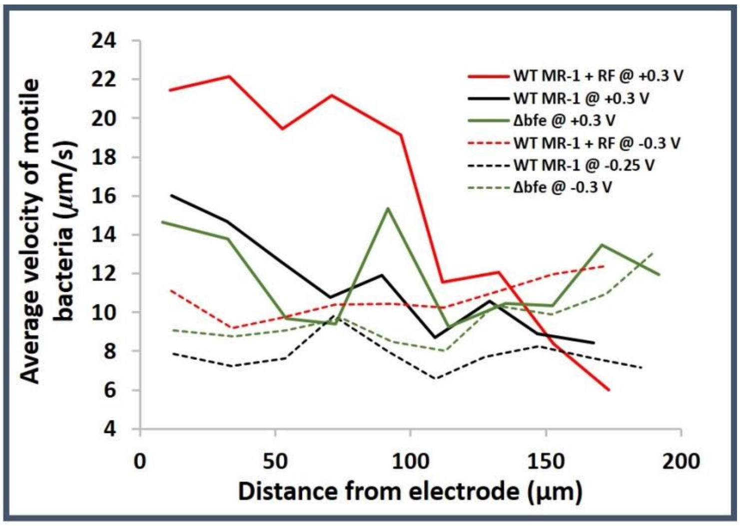

Figure 4.26. Graph of the mean velocity from bacteria swimming above 4 μm/s, against distance from the electrode (anything recorded below 4 μm/s, is assumed to be not moving by its own accord). Each point on the graph is calculated from the traces, passing through the respective zone during one minute. Each zone is within a set distance range from the electrode. The videos were taken ~60 min from loading the capillary with WT, WT + 2 μM riboflavin, or Δbfe suspension and sealing the entrances with silicon grease. The suspensions consisted of the bacterial strain in anaerobic growth media, diluted 5-fold with MOPS buffer and supplemented with 50 mM lactate and in the case of one of the WT MR-1 samples, 2 μM riboflavin. During the relevant parts of the videos, +0.3 V was applied.

Δbfe

The Δbfe deletion strain is missing its periplasmic Flavin adenine dinucleotide (FAD) transporter. FAD is the precursor to flavin mononucleotide (FMN) and riboflavin, both of which are implicated as redox mediators. Without the periplasmic FAD transporter MR-1 is unable to build up FMN and riboflavin in the periplasm or secrete them into their extracellular environment. Assuming the Δbfe strain's deficiency in flavin excretion results in negligible levels of extracellular flavins in the capillary cells, then comparing the behaviour of Δbfe with WT MR-1, in relation to electrodes at oxidising and reducing potentials, should provide the necessary data to assess the importance of extracellular flavins regarding the taxis of MR-1 towards electrodes. Unfortunately, the results were not so clear cut. Possible differences in behaviour between the Δbfe strain and WT MR-1 were observed, but they were subtler than expected. To quantify, these possible differences, more repeats are required so that the inter strain differences can be separated from the intra strain variations between repeats. Ideally experiments using the Δbfe strain would have five repeats as opposed to only two.

From the histograms of **figure 4.20**, one can see the distribution of velocities in the Δbfe population is similar to WT MR-1. The mean velocities for Δbfe (12.4 µm/s) and WT MR-1 (12.5 µm/s) are effectively the same around the electrode during OCPs. Overall, the Δbfe strain shares the same behavioural responses around the SAM modified gold electrode. The potentials at which the Δbfe strain switches motile behaviours has also been preserved from WT MR-1. On switching potentials from <= -0.25 V to >= -0.15 V, the Δbfe strain migrates towards the electrode whilst increasing its average velocity. Switching potentials from >= -0.15 V to <= -0.25 results in a sudden bias away from the electrode and a decrease in bacterial velocity. The one behaviour that could potentially be considered at odds with WT MR-1 is the apparent increase in the number of bacteria with enhanced velocities when oxidation potentials were applied but which are not localised around the electrode and have a relatively "loose" relationship between velocity and electrode proximity. The velocity of these "loose" bacteria is affected on a continuum with increasing positive potential. This subset of bacteria also appears to continue increasing in both number and velocity passed the applied potential of +0.3 V. The described differences are visible in heatmaps for Δbfe in **figure 4.27** where extra motile activity can be seen throughout and not just next to the electrode, as is the case for WT MR-1. The differences between WT MR-1 and Δbfe are subtle and may not be significant. Thus, further repeats are necessary. It may also be informative to add exogenous riboflavin to a Δbfe sample to see if the subtle difference in behaviour can be reversed.

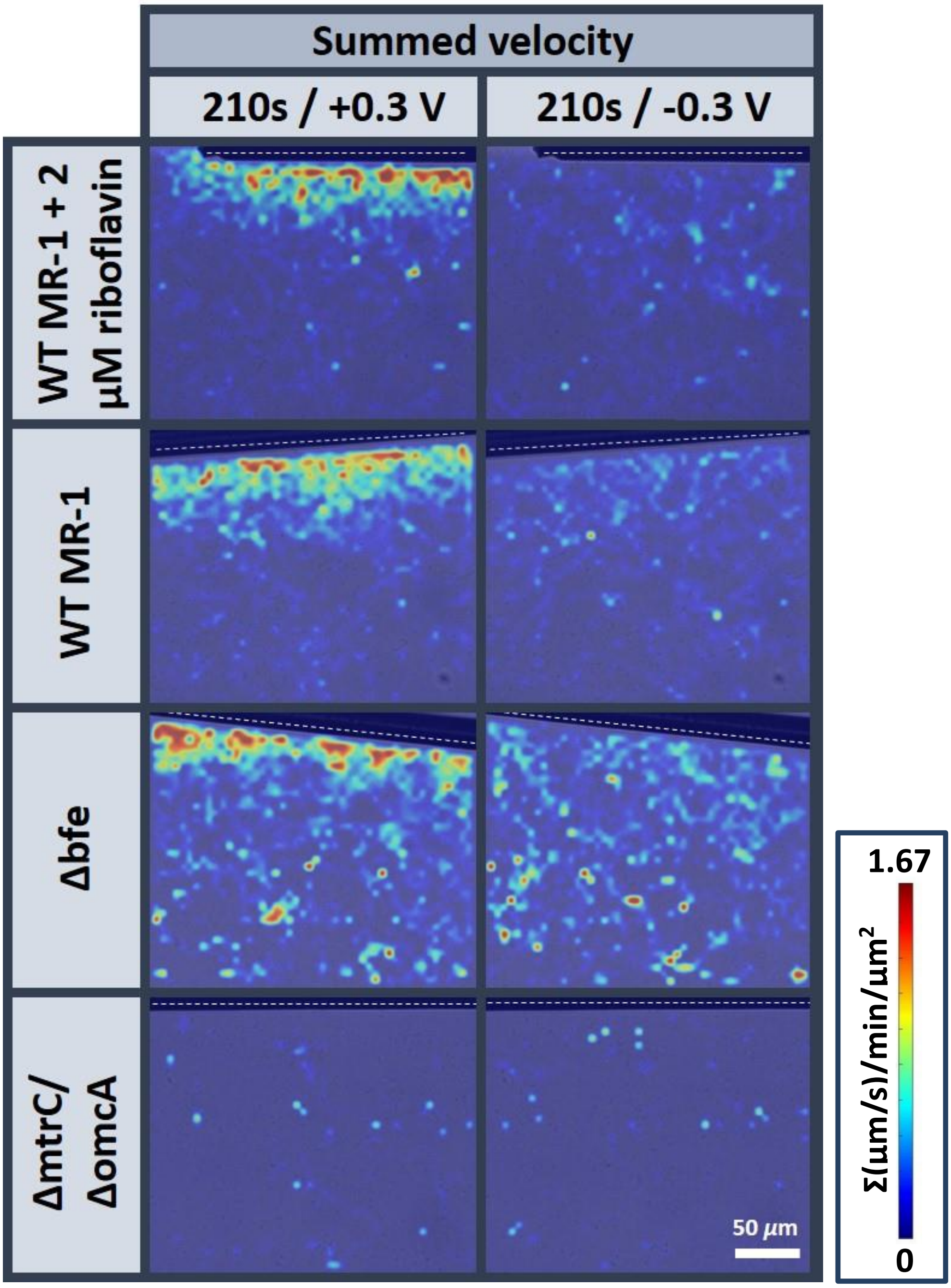

Figure 4.27. Heat maps representing MR-1 motility of two mutant strains (ΔmtrC/ΔomcA and ΔBfe) along with WT MR-1 with and without 2 µM of exogenously added riboflavin, at two different applied potentials (+0.3 V & -0.3 V). Heatmaps created using a jet colour scheme, overlaid onto a representative greyscale frame from the respective video. The colormap is scaled according to MR-1 normalised summed velocity (low-lim = 0, high-lim = 1.67 *Σ(µm/s)/min/µm*^{2}). Dotted white lines highlight the electrode edges. Video were taken after >60 min from loading the capillary with MR-1 suspension and sealing the entrances with silicon grease. The suspensions contained bacteria in anaerobic growth media, diluted 5-fold with MOPS buffer and supplemented with 50 mM lactate, and in one sample of WT MR-1, 2 µM added riboflavin. In parallel to the video, the potentiostat cell was left off for the first 60 s prior to an applied potential of -0.3 V for 210 s, followed by +0.3 V for 210 s.

4.5 Discussion

Early studies around MR-1 taxis towards electron acceptors, carried out by Nealson *et al* [81, 82], and Bencharit *et al* [84] used multiple techniques including chemical in well/plug and swarm plate assays (techniques are described in **chapter 2.1** and **figure 2.1.3**), capillary assays and an in house developed spectrophotometric device. Both conclude from their respective experimental results that chemotaxis is likely the predominant mechanism for MR-1 electron acceptor taxis, although Bencharit *et al* separated out the MR-1 responses towards Mn(III) and Fe(III) as candidates for energy taxis.

Contrary to the conclusion above by Nealson *et al*, a later comprehensive study by Baraquet *et al* [77] into the mechanism of MR-1 taxis towards anaerobic electron acceptors provided very compelling evidence supportive of an energy taxis mechanism for taxis towards the majority of electron acceptors. The mutants ΔtorA and ΔdmsA, deficient in terminal reductases TorA and DmsA, were unable to respond to the substrates TMAO and DMSO, respectively. Inhibition of molybdoenzymes which includes the reductases TorA, DmsA, and NapA, by pre-growing MR-1 with excess tungsten, resulted in the inhibition of taxis towards TMAO, DMSO and nitrate, but had no effect on taxis towards electron acceptors reduced by non-molybdoenzyme reductases such as nitrite and fumarate. These results demonstrate the requirement of terminal reductases for taxis towards the corresponding electron acceptors. The proton motive force (PMF) is considered the final outcome of energy generation. Either of the two components making up the PMF, ΔpH or membrane potential can be potentially sensed by bacteria in order to infer their own metabolic activity for the purpose of energy taxis. To distinguish which of the two components is required for MR-1 energy taxis the authors used nigericin to neutralise proton gradients and valinomycin to disrupt the membrane potential. Only the addition of nigericin had a detrimental effect on taxis towards electron acceptors, indicating ΔpH is the required component for MR-1 energy taxis towards electron acceptors [77]. Separate results from Li *et al* [85] using a custom-made diffusion gradient chamber to evaluate MR-1 electron acceptor taxis, corroborate the results and conclusions of Baraquet *et al.* A subsequent study by Li *et al* [83] sheds insight onto how an energy taxis type mechanism, which requires a gradient of soluble substrate, could help MR-1 locate insoluble electron acceptors. Once stabbed into swarm plates with embedded amorphous MnO_2 or $Fe(OH)_3$ particles, MR-1 migrates outward, with a rate dependant on the concentration of particles, in a similar manner to swarm plates with soluble electron acceptors. On the addition of riboflavin, the MR-1 tactic band migration rate increased dramatically suggesting that flavins, secreted by MR-1 at significant concentrations (~100 nM), play a part in the taxis towards insoluble metal oxides. The authors propose a mediated energy taxis mechanism, whereby MR-1 secretes reduced flavins which diffuse outward. On contact with insoluble electron acceptors the flavin becomes re-oxidised and thus forms a concentration gradient between the MR-1 and the insoluble electron acceptor. MR-1 can then use energy taxis to migrate up the concentration gradient of oxidised flavin.

A recent study by Kim *et al* [134] investigated the effects of flavin and oxygen on MR-1 migration. Using a microfluidics device and video microscopy, the authors performed cell tracking experiments with gradients of oxygen and riboflavin. The results show that MR-1 migrates up concentration gradients of both oxygen and flavin. Going up the concentration gradients, MR-1 swimming speed increases in combination with an increase in the frequency of direction changes. Reportedly, MR-1 displayed reversal and forward-backward-flick behaviours both of which are indicative of unipolar flagellates [149, 150], to change its direction. Interestingly, the velocity of MR-1 in the direction of riboflavin gradients is significantly increased under anaerobic conditions. Together, these findings give further support to an energy taxis mechanism, specifically the mechanism proposed by Li *et al* [83] of mediated energy taxis with flavins as the mediator.

Prior to the video microscopy cell tracking experiments of Kim *et al* [134], Harris *et al* [132, 133] used a similar cell tracking technique to investigate MR-1 taxis towards insoluble electron acceptors including MnO_2 particles and electrodes which supported previous findings that MR-1 is capable of tactic responses towards insoluble metal oxide electron acceptors[83, 84]. A strong positive response was demonstrated towards MnO_2 particles which is in keeping with swarm plate assays (embedded with MnO_2) by Worden *et al* [83]. MR-1 bacteria that are close to MnO_2 particles display an increase in swimming speed and an associated increase in reversal frequency similar to that observed later by Kim *et al* [134] for flavin and O_2 gradients. In contrast to the flavin mediated energy taxis proposed by Li *et al* [83], Harris *et al* suggests gradients of Mn(II), formed by MR-1 reducing MnO_2 at the particle surface, could facilitate chemotaxis. A similar, albeit to a much lesser extent, response was observed with $Fe(OH)_3$ particles indicating the response is not isolated to MnO_2. In addition to using insoluble metal oxides, Harris *et al*, also tested carbon fibre micro electrodes, poised at +600 mV (vs Ag/AgCl, i.e. ~+800 mV vs SHE), to mimic the redox potential of MnO_2 particle surfaces. The response of MR-1 to oxidative electrode potentials was almost identical to that of the metal oxides. Of the potentials tested no swimming response was observed at potentials below +500 mV (vs Ag/AgCl, i.e. ~+700 mV vs SHE), with optimal responses seen between +550 to

+800 mV (vs Ag/AgCl, i.e. ~+750 to +1000 mV vs SHE). Manual tracking of cells close to the metal oxide particles and poised electrode surface showed that those cells that made contact would swim faster with a significantly higher reversal frequency then non-contacting cells. Mutant strains deficient in any of the genes required for EET (e.g *cymA*), abolished the responses observed with the WT MR-1 to MnO_2, $Fe(OH)_3$, and poised electrodes, demonstrating the requirement of EET for MR-1 migration to insoluble electron acceptors. As expected, a cheomotaxis deficient ΔcheA-3 strain, incapable of reversing the direction of its flagella motor and therefore unable to reverse its swimming direction, was also unable to congregate around the insoluble electron acceptors. These results put together led Harris *et al* to propose a hypothetical model, termed 'congregation' to explain how MR-1 accumulates around insoluble electron acceptors. Congregation is first initiated when MR-1 randomly encounters an insoluble electron acceptor allowing transfer of electrons through the MtrC/OmcA pathway from the bacteria to the electron acceptor. This event causes a change in swimming behaviour whereby speed and reversal frequency increases which allows the bacteria to keep within proximity of the insoluble electron acceptor. Over time this 'congregation' can lead to attachment and biofilm formation [132].

In our experiments, using a similar experimental set-up as Harris *et al*, an increase in the average MR-1 velocity and population density was observed around electrodes poised at oxidative potentials. At a qualitative level, these results are consistent with the behavioural changes reported by Harris *et al* for MR-1 in close proximity to metal oxides and carbon fibre electrodes poised at oxidative potentials. The potential range of +0.55 to +0.8 V (vs Ag/AgCl, i.e. ~+0.75 to +1.0 V vs SHE) reported by Harris *et al*, required to induce tactic responses around carbon fibre electrodes was far more positive than the -0.15/-0.205 V (vs SHE) lowest potential required to switch the tactic behaviour on around the SAM modified Au wire electrodes employed here.

A simple Ag/AgCl wire was employed as the reference electrode in our capillary cell set-up. The potential offset from a SHE was calculated using the samples Cl^- concentration as described above. It is possible that elements in the experimental samples (MR-1 suspension) can affect the Ag/AgCl wires surface and cause the potential to drift over time. Fortunately, a significant proportion of our samples included 2 µM of exogenous riboflavin which could be used as an internal reference redox system. Using riboflavin to check the potentials, only minimal (up to ~20 mV) variation was observed over the duration of the experiments (1-5 days) or between different experiments/electrodes. Potential drifts of up to 20 mV cannot account for the ~ 1 V difference in potentials, reported here and those reported by Harris *et al*, required to elicit a behavioural response.

The difference in potentials could be related to the different electrodes and media used. For most of our experiments SAM modified gold wire electrodes were used with a media/electrolyte containing lactate supplemented MOPS buffer with or without added riboflavin in addition to dilute anaerobic culturing media (containing LB, fumarate and lactate). In comparison Harris *et al* used carbon fibre electrodes with a defined minimal media **[132]**. The presence of soluble electron acceptors has previously been reported to effect MR-1 tactic responses to other electron acceptors **[81]**. The media used by Harris *et al* did not contain significant concentrations of any electron acceptors, although it did contain significant concentrations (relative to the amounts secreted by MR-1) of the mediator riboflavin (132.8 nM) whilst the media used in our experiments either contained zero additional riboflavin or the relatively high concentration of 2 µM of riboflavin. In addition, all the samples used to obtain the results in this chapter would have contained a low concentration of the soluble electron acceptor fumarate which seemed to improve the MR-1 tactic activity around the electrode. As discussed in **chapter 3**, the electrode material and surface characteristics can alter the electrochemistry at the interface with some electrodes requiring much higher overpotentials for a reaction (at a significant rate) than others. Protein film electrochemistry with the relevant outer membrane cytochromes for DET has been successfully performed on both alcohol terminated SAM modified gold **[105]** and carbon electrodes **[151]** with no major differences in the potential window required. In relation to riboflavin electrochemistry, both carbon fibre electrodes and the SAM modified gold wire electrodes used in our experiments appeared to have relatively facile ET kinetics with riboflavin. Thus, assuming the tactic behaviour observed around electrodes poised at oxidative potentials is controlled by ET, which the evidence suggests, then there should not be a significant difference in oxidative overpotential between the electrodes used here and the carbon fibre electrode used by Harris *et al*.

After > 2 minutes at a sufficiently negative (reductive) potential, previously highly motile MR-1 around the electrode, became sluggish and effectively non-motile in some cases. On switching the potential to a sufficiently positive (oxidative) potential, MR-1 in the area around the electrode gradually increased motility. No requirement for direct contact with the electrode was found, instead MR-1 >10 µm from the electrode surface were observed transitioning from non-motile states into highly motile states on switching the potential without encountering the electrode. If MR-1 does not require contact of the electrode to sense relevant changes to the electrode potential, as seems to be the case from our results, then MR-1 must indirectly sense the electrode potential. Indirect sensing could be achieved using a soluble redox active molecule which is oxidised by insoluble electron acceptors. The potential range in which MR-1 switched between tactic behaviours towards the working electrode was found to be between -0.25 V to -0.15 V (SHE). This potential region corresponds to the midpoint potential of riboflavin which fits with the hypothesis that MR-1 uses self-secreted redox mediators for finding insoluble electron acceptors.

MR-1 reduces flavins almost exclusively through the Mtr pathway [152] with both MtrC and OmcA functioning effectively as terminal reductases for riboflavin and flavin mononucleotide. If MR-1 employs self-secreted flavin as redox sensors in a mediated energy taxis like mechanism, then disrupting the Mtr EET pathway should have a detrimental effect on the MR-1 tactic response to electrodes poised at sufficiently positive (oxidative) potentials. As expected, electrochemical video tracking experiments using the ΔmtrC/ΔomcA double deletion mutant showed no tactic response towards electrodes poised at > -0.15 V. On initial loading of the mutant into the capillary cell, the bacteria were highly motile but without any relation to their distance from the electrode surface, as was the case with WT-MR-1 for the first ~ 15 to 60 minutes after loading. Initial motility in both the WT and ΔmtrC/ΔomcA strain is thought to be due to an aerotactic response which soon dies down as the remaining dissolved oxygen is consumed by the respiring MR-1. In the case of WT MR-1 once the oxygen has been consumed a tactic response around the working electrode develops, whilst with the ΔmtrC/ΔomcA strain no motile behaviour is observed after the oxygen has been consumed. Although these results support the flavin mediated energy taxis hypothesis, the Mtr pathway is nonspecific and capable of reducing many electron acceptors in addition to its role as the predominant pathway for DET. One scenario/possibility is that MR-1 can utilises any appropriate soluble redox active molecules available for mediated energy taxis towards areas of abundant electron acceptors.

In addition to MR-1 velocity and motile population density, swimming direction in relation to the electrode was also analysed. On switching potentials from < -0.25 V to > -0.15 V there is an initial increase of MR-1 swimming towards the electrodes which then decreases over time. Conversely, switching from > -0.15 V to < -0.25 V causes MR-1 to swim away from the electrode. On switching to an oxidising potential, if flavin is present in the sample, a gradient of oxidised flavin will develop around the electrode. It is proposed MR-1 can travel up this gradient, or possibly any gradient of oxidised redox molecules (assuming they are substrates of the Mtr pathway) with an appropriate redox potential. On switching to reductive potentials, the flavin close to the electrode will become reduced and a negative gradient of oxidised flavin will develop in the short term causing the bacteria to travel in the opposite direction to the electrode

The flavin secretion deficient Δbfe strain still responded towards the working electrode and maintained the same potential range (-0.25 to -0.15 V vs SHE) as the WT MR-1 for switching its behaviour towards the electrode. Just as with WT MR-1, direct contact with the electrode was not required in order to elicit a change in behaviour. On changing the potential to >= -0.15 V, bacteria that were >40 µm from the electrode surface and not moving or moving very slow, begin to move and increase their velocity without prior contact with the electrode. This observation suggests that a redox mediator is still present in the Δbfe samples. Either small concentrations of flavin still exist in the samples or another redox mediator is present.

The samples were comprised of a significant amount (20% v/v) of overnight anaerobic culture media. The culture contained left over fumarate, lactate and metabolites from growing MR-1 along with an undefined mix of peptides, free amino acids, sugars, vitamins, and trace elements from the tryptone and yeast extract components. The yeast extract is of concern due to a possible high content of B vitamins. A recent technical note [153] puts the riboflavin concentration in yeast extract between 60 – 90 mg/kg which translates into a final concentration of around 160 – 200 nM. This concentration is roughly equivalent to that secreted by WT MR-1. Thus, the likely high flavin content of yeast extract explains the similarity in behaviour between Δbfe and WT-MR-1. Ideally the samples would have been in defined media but as explained in the development of the experimental set up, attempts at washing MR-1 and resuspension in minimal media or lactate supplemented buffer resulted in very low motility from MR-1 in the anaerobic capillary cell.

4.6 Conclusions

MR-1 biofilm quality and electrode coverage directly effects the maximum ET rate achievable in MES. The process of MR-1 colonisation of electrodes thus has important implications for the development of MES. The first step in the process of electrode colonisation is the accumulation of bacteria around the electrode. Depending on If this bacterial accumulation relies on initial random encounters or if a soluble mediator is required for effective MR-1 migration towards electrodes, different approaches would be required for encouraging initial electrode colonisation.

From video tracking experiments using an inhouse developed tracking algorithm built around the Crocker particle tracking algorithm, validated against an independent video processing technique based on Shannon's entropy, it was possible to obtain individual and population level data on MR-1 motile behaviour around electrodes at various potentials. Potentials above the midpoint potential of riboflavin resulted in a positive response from MR-1 towards the electrode with both an increase in swimming velocity and an overall bias in swimming direction towards the electrode. Applying potentials more negative than the midpoint potential caused a negative response toward the electrode. The transition between negative and positive response was relatively sharp with little change observed in increasing (i.e. more positive) the potential above -0.15 V (SHE) or decreasing (i.e. more negative) the potential below -0.25 V (SHE). The response was amplified by adding extra riboflavin whilst no response was observed with the ΔmtrC/ΔomcA deletion mutant deficient in the Mtr pathway which is the predominant extracellular flavin reduction pathway. These results strongly support a flavin mediated energy taxis mechanism for locating electrodes and applicable insoluble electron acceptors. A mutant deficient in flavin secretion (*Δbfe*) was also employed in our experiments, but because of left over anaerobic media in the samples used for experiments the was likely still a significant concentration of riboflavin originating from the LB (specifically the yeast extract) as discussed in the discussion. With an appropriate riboflavin free defined media, the experiments should be repeated using Δbfe and WT MR-1.

5. Summary and Conclusions

S. oneidensis MR-1, has been the subject of intense research due to its application as a model organism for EET and potential use within MES. It is the availability of MR-1's genome sequence, ease of culturing, rapid generation time and dynamic respiration with a diverse range of extracellular terminal electron acceptors that has made it such a popular model organism. The production of electrical energy in an environmentally friendly manner, in conjunction with wastewater treatment, has been a significant driving force behind the continued research around MR-1 and MFC technologies. Unfortunately, even theoretical maximum power densities for MFC are too far below that of cheaper conventional energy sources (including renewables)[154]. However, a shift in goal from large scale electrical power generation to niche applications requiring low power for extended periods of time, novel strategies for biosynthesising high value chemicals and self-sufficient biosensors using the microbe as both detector and transducer, has kept up interest in EET capable organisms and MES [155].

5.1 Surfaces Effects on MR-1 Extracellular Electron transfer and the presence of iron redox cycling

To fully take advantage of MR-1 and other electrogenic organisms within MES a detailed understanding of the ET process between the organism and electrode is required. The two general strategies a bacterium can employ are DET, where the bacteria's respiration is directly linked to the electrode using outer membrane cytochromes as a bridge for transferring electrons, and MET which requires the presence of a redox active mediator for ferrying electrons between the bacteria and electrode. DET is thought to be the predominant pathway in *Geobacter* sp and is generally desired for MES applications for both efficiency and practical reasons. In the case of MR-1 both DET and MET are generally considered to occur concomitantly. Although, the debate continues as to which ET pathway is relevant within its natural habitats and for its use in MES and within the literature one can find support for both DET and MET as the dominant pathway. Electrochemistry and particularly CV is commonly employed for studying MR-1 ET, and it is usual to see two separate waves or peaks corresponding to two separate redox couples. Signals close to -0.2 V (SHE) are mostly assigned to flavin MET whilst signals in the region between 0 to +0.3 V are assigned to DET through outer membrane cytochromes (MtrC and OmcA). The potential of the signal assigned to MtrC/OmcA DET varies significantly between reports and does not fall into the potential ranges measured for OmcA and MtrC using protein film voltammetry (PFV) on multiple surfaces (graphite, ITO, and SAM modified gold with amine and alcohol terminal groups). The inconsistencies between electrochemical results in the literature are not surprising when one considers that the experimental conditions, including the working electrode and media, in addition to the procedures vary greatly from one report to the next.

In **chapter 3** we have demonstrated that the surface properties of electrodes significantly impact EET pathways of MR-1 in MESs. Hydrophilic, non-charged electrodes (gold modified with hydroxy terminated SAMs) show favourable electron transfer kinetics with flavin, enabling efficient ET between MR-1 and electrode with flavin as a mediator. However, negatively charged electrodes (gold modified with carboxylic acid terminated SAMs) exhibit quasi- or irreversible electron transfer with flavins, emphasising an alternative pathway that is observed at higher potentials of ~0.1 V vs SHE. This high-potential pathway has previously been ascribed to MtrC/OmcA DET but, through the addition of deferoxamine, we concluded that the alternative high-potential pathway, in our system, is mediated by soluble iron possibly released by lysing MR-1. In addition to the SAM modified gold electrodes with lactate supplemented buffer, pyrolytic graphite and ITO electrodes along with a defined minimal media were also tested. The same result was obtained after the addition of deferoxamine with all the mentioned electrodes and media/electrolyte. Thus, indicating the Fe redox signal was not just isolated to the SAM modified gold electrodes. Similar iron mediated EET could operate in other MESs and this would explain the wide variation in redox potentials reported in the literature between groups using different electrodes and electrolyte solutions. The redox potential of iron is dependent on its interactions with ligands in solution, e.g. lactate, as well as the surface properties of the electrode material. Although no specific redox peak or wave could be assigned to DET in our system this does not mean that MR-1 is not capable of DET, just that DET does not appear present at a significant level within our system. DET could be a prominent ET pathway for MR-1 growing on metal oxides in their natural habitat. Future MR-1 ET investigation should use mild iron chelators such as deferoxamine to confirm DET mechanisms. For MR-1 to be used in MES applications with high efficiency and performance, new anode materials will need to be developed that promotes DET.

5.2 Tracking MR-1 Trajectories and Flavin Mediated Energy Taxis

Although MR-1 has been researched extensively, the issue of how MR-1 locates and migrates towards electron acceptors, especially insoluble electron acceptors such as electrodes, has not been fully resolved. From a study considering the effects of different holding potentials on the development of electroactive biofilms [48], It was suggested that MR-1 could employ self-secreted flavins for locating insoluble electron acceptors and help with the recruitment of MR-1 to initiate biofilm formation. Using agar plate based assays Li *et al* provided evidence for the utilisation of riboflavin by MR-1 in a mediated energy taxis type mechanism to locate insoluble metal oxides. Issues previously raised regarding agar plate techniques and false positive results led Harris *et al,* who had previously investigated MR-1 taxis using agar plate techniques, to use video microscopy cell tracking with both insoluble metal oxides and electrodes. Harris *et al* proposed a separate model for MR-1 taxis toward insoluble electron acceptors (including electrodes poised at oxidising potentials), termed ‘congregation’ which relies on initial chance encounters of direct contact between MR-1 and acceptor. Recently (published during our research), a report by Kim *et al* [134] provided direct evidence for an MR-1 taxis response up a gradient of oxidised riboflavin by performing cell tracking experiments using a microfluidics device.

To directly examine the effects of flavins on MR-1 in response to electrodes at oxidising potentials, video microscopy cell tracking experiments were carried out using a capillary electrochemical cell. Tracking of MR-1 trajectories (including high velocity trajectories) from bright field microscopy, low frame rate (10 FPS), videos was achieved using a modified Matlab version of the Crocker particle tracking algorithm. In conjunction with allowing the tracking of high velocity bacteria at low frame rates the new algorithm significantly reduce tracking artefacts and provided cleaner data sets. In addition to obtaining quantitative data from the tracked trajectories, pixel level intensity variations were processed to form Shannon entropy maps of video segments which could be used to qualitatively check the tacked data. It is clear by both watching the videos and from the analysed data that MR-1 has a tactic response to electrodes poised at oxidative potentials and that the potential required for switching behaviour (-0.25 to -0.15 V vs SHE) coincides with the midpoint potential of flavins (-0.2V vs SHE). During positive/oxidative potentials > -0.15 V (SHE) both average swimming velocity and the population density of motile bacteria increase with proximity to the electrode. Whilst at negative/reductive potentials < -0.25 V (SHE) the is very little motility and no relationship with distance to the electrode. Switching the potential from negative to positive leads to a fairly quick bacterial response involving a gradual increase in the surrounding bacterial velocity and an overall migration towards the electrode with a quantifiable directional bias. Conversely, switching the potential from positive to negative results in a rapid migration of bacteria away from the electrode and a general slowing down of all the bacteria. The response of MR-1 towards electrodes was present in the absence of any additionally added exogenous flavin but, with the addition of 2 µM riboflavin, the response was significantly enhanced. Although the response of MR-1 reported in **chapter 4** is similar to the response reported by Naelson *et al*, the potential required to elicit the response was significantly different with a potential of +0.75 to +1.0 V vs SHE required in the reports by Naelson *et al*, compared with > -0.15 V vs SHE reported here.

In addition to WT MR-1, experiments were conducted using two mutants, *ΔmtrC/ΔomcA* (Mtr EET pathway deficient) and *Δbfe* (flavin secretion deficient). The *ΔmtrC/ΔomcA* showed no response towards the electrode but maintained an aerotaxis response, thus demonstrating the requirement of EET for taxis towards electrodes. It is important to note that MR-1 uses the Mtr pathway to reduce flavins with MtrC and OmcA as the terminal reductases. Results obtained with *Δbfe* were not significantly different from WT MR-1. The likely presence of significant levels of riboflavin carried over from the yeast extract (used to make the anaerobic media) would explain the lack of difference between WT MR-1 and *Δbfe*.

In the congregation model proposed by Naelson *et al*, initial contact is required between MR-1 and the insoluble electron acceptor to elicit a change in motile behaviour such as increased swimming velocity and reversal frequency. Our results indicate no direct contact with the electrode is required for a switch in behaviour. From the videos MR-1 > 40 µm from the electrode surface can be observed to increase velocity from almost no motility on switching the potential from negative to positive. No contact was observed between switching the potential and a motile response on many occasions including with the *Δbfe* deletion mutant. Overall our results are in keeping with a flavin mediated energy taxis type of mechanism.

>In a small enclosed volume, such as in an electrochemical cell used for whole cell electrochemical experiments, flavins released by the bacteria can build up to significant concentrations (100 to 200 nM) [43]. At these concentrations flavins significantly enhance the ET rate of MR-1, thus the energetic burden in synthesising and excreting flavins can be repaid through enhanced respiration. Flavin MET could also enable more efficient use of a

limited surface area for some insoluble electron acceptors. With a soluble mediator a larger population of bacteria could take advantage of the same geometric surface area. The mentioned conditions (small enclosed volumes) are generally not relevant for either the natural habitats of MR-1 (vast water systems subject to currents) or many MES devices that require continual flow or frequent media exchanges. In these circumstances self-secreted flavins are unlikely to achieve the same kind of concentrations measured in electrochemical cells. Therefore, flavins functioning solely as electron shuttles for MET may not be viable in these environments.

Here we propose MR-1 utilises flavins for multiple roles associated with its EET respiration. Firstly, as an electron shuttle for MET, enabling respiration to continue in situations where the bacteria is in a planktonic state with limited soluble electron acceptors and no insoluble electron acceptors in its immediate vicinity. Secondly, as a means for locating and directing MR-1 towards insoluble electron acceptors (e.g. metal oxides) and initiating colonisation of the surface where it can respire via the more efficient DET pathway. Thirdly, as cofactors for MtrC and OmcA, enabling enhanced DET. The concentrations required for efficient energy taxis could be much lower than for MET. Self-secreted flavins are not just simple redox mediators and could be an important factor for MR-1’s survival in electron acceptor limited niches.

References

1. Golitsch, F., C. Buecking, and J. Gescher, *Proof of principle for an engineered microbial biosensor based on Shewanella oneidensis outer membrane protein complexes.* Biosensors & Bioelectronics, 2013. **47**: p. 285-291.
2. Ji, Q., et al., *Removal of water-insoluble Sudan dyes by Shewanella oneidensis MR-1.* Bioresource Technology, 2012. **114**: p. 144-148.
3. Logan, B.E. and K. Rabaey, *Conversion of Wastes into Bioelectricity and Chemicals by Using Microbial Electrochemical Technologies.* Science, 2012. **337**(6095): p. 686-690.
4. Derby H, H.B., *Bacteriology of butter. IV. Bacteriological studies of surface taint butter*, in *Dairy Industry Section* D. C. F. Curtiss, Editor. 1931, Agricultural Experiment Station, Iowa State College of Agriculture and Mechanic Arts.
5. Macdonell, M.T. and R.R. Colwell, *Phylogeny of the Vibrionaceae, and Recommendation for 2 New Genera, Listonella and Shewanella.* Systematic and Applied Microbiology, 1985. **6**(2): p. 171-182.
6. Janda, J.M. and S.L. Abbott, *The genus Shewanella: from the briny depths below to human pathogen.* Critical Reviews in Microbiology, 2014. **40**(4): p. 293-312.
7. Nealson, K.H. and J. Scott, *Ecophysiology of the Genus Shewanella*. Prokaryotes: A Handbook on the Biology of Bacteria, Vol 6, Third Edition: Proteobacteria: Gamma Subclass, ed. M. Dworkin, et al. 2006. 1133-1151.
8. Hau, H.H. and J.A. Gralnick, *Ecology and biotechnology of the genus Shewanella*, in *Annual Review of Microbiology*. 2007. p. 237-258.
9. Abboud, R., et al., *Low-temperature growth of Shewanella oneidensis MR-1.* Applied and Environmental Microbiology, 2005. **71**(2): p. 811-816.
10. Valentine, R.C. and D.L. Valentine, *Omega-3 fatty acids in cellular membranes: a unified concept.* Progress in Lipid Research, 2004. **43**(5): p. 383-402.
11. Hartshorne, R.S., et al., *Characterization of an electron conduit between bacteria and the extracellular environment.* Proceedings of the National Academy of Sciences of the United States of America, 2009. **106**(52): p. 22169-22174.
12. Shi, L., et al., *Molecular underpinnings of Fe(III) oxide reduction by Shewanella oneidensis MR-1.* Frontiers in Microbiology, 2012. **3**: p. 50.
13. Clarke, T.A., et al., *Structure of a bacterial cell surface decaheme electron conduit.* Proceedings of the National Academy of Sciences of the United States of America, 2011. **108**(23): p. 9384-9389.
14. Carmona-Martinez, A.A., et al., *Cyclic voltammetric analysis of the electron transfer of Shewanella oneidensis MR-1 and nanofilament and cytochrome knock-out mutants.* Bioelectrochemistry, 2011. **81**(2): p. 74-80.
15. Firer-Sherwood, M.A., et al., *Tools for resolving complexity in the electron transfer networks of multiheme cytochromes c.* Metallomics, 2011. **3**(4): p. 344-348.
16. Call, D.F. and B.E. Logan, *Lactate Oxidation Coupled to Iron or Electrode Reduction by Geobacter sulfurreducens PCA.* Applied and Environmental Microbiology, 2011. **77**(24): p. 8791-8794.

17. Pant, D., et al., *A review of the substrates used in microbial fuel cells (MFCs) for sustainable energy production.* Bioresource Technology, 2010. **101**(6): p. 1533-1543.

18. Rabaey, K. and W. Verstraete, *Microbial fuel cells: novel biotechnology for energy generation.* Trends in Biotechnology, 2005. **23**(6): p. 291-298.

19. Santoro, C., et al., *Microbial fuel cells: From fundamentals to applications. A review.* Journal of Power Sources, 2017. **356**: p. 225-244.

20. Yang, W., K.K. Lee, and S. Choi, *A laminar-flow based microbial fuel cell array.* Sensors and Actuators B-Chemical, 2017. **243**: p. 292-297.

21. Vologni, V., et al., *Increased power generation from primary sludge by a submersible microbial fuel cell and optimum operational conditions.* Bioprocess and Biosystems Engineering, 2013. **36**(5): p. 635-642.

22. Pham, T.H., P. Aelterman, and W. Verstraete, *Bioanode performance in bioelectrochemical systems: recent improvements and prospects.* Trends in Biotechnology, 2009. **27**(3): p. 168-178.

23. Turner, A.P.F., *Aims & Scope.* Biosensors and Bioelectronics, 2018.

24. Gralnick, J.A. and D.K. Newman, *Extracellular respiration.* Molecular Microbiology, 2007. **65**(1): p. 1-11.

25. Matias, V.R.F., et al., *Cryo-transmission electron Microscopy of frozen-hydrated sections of Escherichia coli and Pseudomonas aeruginosa.* Journal of Bacteriology, 2003. **185**(20): p. 6112-6118.

26. Graham, L.L., T.J. Beveridge, and N. Nanninga, *PERIPLASMIC SPACE AND THE CONCEPT OF THE PERIPLASM.* Trends in Biochemical Sciences, 1991. **16**(9): p. 328-329.

27. Schuetz, B., et al., *Periplasmic Electron Transfer via the c-Type Cytochromes MtrA and FccA of Shewanella oneidensis MR-1.* Applied and Environmental Microbiology, 2009. **75**(24): p. 7789-7796.

28. Ross, D.E., et al., *Towards Electrosynthesis in Shewanella: Energetics of Reversing the Mtr Pathway for Reductive Metabolism.* Plos One, 2011. **6**(2).

29. Rosenbaum, M.A., et al., *Transcriptional Analysis of Shewanella oneidensis MR-1 with an Electrode Compared to Fe(III)Citrate or Oxygen as Terminal Electron Acceptor.* Plos One, 2012. **7**(2).

30. Paquete, C.M. and R.O. Louro, *Molecular details of multielectron transfer: the case of multiheme cytochromes from metal respiring organisms.* Dalton Transactions, 2010. **39**(18): p. 4259-4266.

31. Liu, X.-W., et al., *Experimental and Theoretical Demonstrations for the Mechanism behind Enhanced Microbial Electron Transfer by CNT Network.* Scientific Reports, 2014. **4**.

32. Myers, C.R. and J.M. Myers, *Cloning and sequence of cymA a gene encoding a tetraheme cytochrome c required for reduction of iron(III), fumarate, and nitrate by Shewanella putrefaciens MR-1.* Journal of Bacteriology, 1997. **179**(4): p. 1143-1152.

33. Tsapin, A.I., et al., *Identification of a small tetraheme cytochrome c and a flavocytochrome c as two of the principal soluble cytochromes c in Shewanella*

oneidensis strain MR1. Applied and Environmental Microbiology, 2001. **67**(7): p. 3236-3244.

34. Meyer, T.E., et al., *Identification of 42 possible cytochrome c genes in the Shewanella oneidensis genome and characterization of six soluble cytochromes.* Omics-a Journal of Integrative Biology, 2004. **8**(1): p. 57-77.

35. Fonseca, B.M., et al., *Mind the gap: cytochrome interactions reveal electron pathways across the periplasm of Shewanella oneidensis MR-1.* Biochemical Journal, 2013. **449**: p. 101-108.

36. Shi, L., et al., *Molecular underpinnings of Fe(III) oxide reduction by Shewanella oneidensis MR-1.* Frontiers in Microbiology, 2012. **3**.

37. Qian, Y.F., et al., *Mapping the Iron Binding Site(s) on the Small Tetraheme Cytochrome of Shewanella oneidensis MR-1.* Biochemistry, 2011. **50**(28): p. 6217-6224.

38. Richardson, D.J., et al., *The porin-cytochrome' model for microbe-to-mineral electron transfer.* Molecular Microbiology, 2012. **85**(2): p. 201-212.

39. Okamoto, A., et al., *In vivo Electrochemistry of C-Type Cytochrome-Mediated Electron-Transfer with Chemical Marking.* ChemBioChem, 2009. **10**(14): p. 2329-2332.

40. Okamoto, A., R. Nakamura, and K. Hashimoto, *In-vivo identification of direct electron transfer from Shewanella oneidensis MR-1 to electrodes via outer-membrane OmcA-MtrCAB protein complexes.* Electrochimica Acta, 2011. **56**(16): p. 5526-5531.

41. Pirbadian, S., et al., *Shewanella oneidensis MR-1 nanowires are outer membrane and periplasmic extensions of the extracellular electron transport components.* Proceedings of the National Academy of Sciences of the United States of America, 2014. **111**(35): p. 12883-12888.

42. Malvankar, N.S. and D.R. Lovley, *Microbial nanowires for bioenergy applications.* Current Opinion in Biotechnology, 2014. **27**: p. 88-95.

43. Marsili, E., et al., *Shewanella Secretes flavins that mediate extracellular electron transfer.* Proceedings of the National Academy of Sciences of the United States of America, 2008. **105**(10): p. 3968-3973.

44. Okamoto, A., et al., *Rate enhancement of bacterial extracellular electron transport involves bound flavin semiquinones.* Proceedings of the National Academy of Sciences of the United States of America, 2013. **110**(19): p. 7856-7861.

45. Ross, D.E., S.L. Brantley, and M. Tien, *Kinetic Characterization of OmcA and MtrC, Terminal Reductases Involved in Respiratory Electron Transfer for Dissimilatory Iron Reduction in Shewanella oneidensis MR-1.* Applied and Environmental Microbiology, 2009. **75**(16): p. 5218-5226.

46. Cooper, R.E., et al., *Ferrihydrite-associated organic matter (OM) stimulates reduction by Shewanella oneidensis MR-1 and a complex microbial consortia.* Biogeosciences, 2017. **14**(22): p. 5171-5188.

47. Lies, D.P., et al., *Shewanella oneidensis MR-1 uses overlapping pathways for iron reduction at a distance and by direct contact under conditions relevant for biofilms.* Applied and Environmental Microbiology, 2005. **71**(8): p. 4414-4426.

48. Roy, J.N., et al., *Applied Electrode Potential Leads to Shewanella oneidensis MR-1 Biofilms Engaged in Direct Electron Transfer.* Journal of the Electrochemical Society, 2013. **160**(11): p. H866-H871.

49. Roy, J.N., et al., *Catalytic biofilm formation by Shewanella oneidensis MR-1 and anode characterization by expanded uncertainty.* Electrochimica Acta, 2014. **126**: p. 3-10.

50. Wu, C., et al., *Electron acceptor dependence of electron shuttle secretion and extracellular electron transfer by Shewanella oneidensis MR-1.* Bioresource Technology, 2013. **136**: p. 711-714.

51. Moens, S. and J. Vanderleyden, *Functions of bacterial flagella.* Critical Reviews in Microbiology, 1996. **22**(2): p. 67-100.

52. Wadhams, G.H. and J.P. Armitage, *Making sense of it all: Bacterial chemotaxis.* Nature Reviews Molecular Cell Biology, 2004. **5**(12): p. 1024-1037.

53. Kearns, D.B., *A field guide to bacterial swarming motility.* Nature Reviews Microbiology, 2010. **8**(9): p. 634-644.

54. Jarrell, K.F. and M.J. McBride, *The surprisingly diverse ways that prokaryotes move.* Nature Reviews Microbiology, 2008. **6**(6): p. 466-476.

55. Trachtenberg, S., *The cytoskeleton of Spiroplasma: A complex linear motor.* Journal of Molecular Microbiology and Biotechnology, 2006. **11**(3-5): p. 265-283.

56. Skerker, J.M. and H.C. Berg, *Direct observation of extension and retraction of type IV pili.* Proceedings of the National Academy of Sciences of the United States of America, 2001. **98**(12): p. 6901-6904.

57. Wolgemuth, C., et al., *How myxobacteria glide.* Current Biology, 2002. **12**(5): p. 369-377.

58. Hoiczyk, E. and W. Baumeister, *The junctional pore complex, a prokaryotic secretion organelle, is the molecular motor underlying gliding motility in cyanobacteria.* Current Biology, 1998. **8**(21): p. 1161-1168.

59. Paulick, A., et al., *Two different stator systems drive a single polar flagellum in Shewanella oneidensis MR-1.* Molecular Microbiology, 2009. **71**(4): p. 836-850.

60. Atsumi, T., L. McCarter, and Y. Imae, *Polar and Lateral Flagellar Mototrs of Marine Vibrio are Driven by Different Ion-Motive Forces.* Nature, 1992. **355**(6356): p. 182-184.

61. Taylor, B.L., I.B. Zhulin, and M.S. Johnson, *Aerotaxis and other energy-sensing behavior in bacteria.* Annual Review of Microbiology, 1999. **53**: p. 103-128.

62. Schweinitzer, T. and C. Josenhans, *Bacterial energy taxis: a global strategy?* Archives of Microbiology, 2010. **192**(7): p. 507-520.

63. Alexandre, G., *Coupling metabolism and chemotaxis-dependent behaviours by energy taxis receptors.* Microbiology-Sgm, 2010. **156**: p. 2283-2293.

64. Ma, Q.H., et al., *The Aer protein of Escherichia coli forms a homodimer independent of the signaling domain and flavin adenine dinucleotide binding.* Journal of Bacteriology, 2004. **186**(21): p. 7456-7459.

65. Gosink, K.K., M.D. Buron-Barral, and J.S. Parkinson, *Signaling interactions between the aerotaxis transducer Aer and heterologous chemoreceptors in Escherichia coli.* Journal of Bacteriology, 2006. **188**(10): p. 3487-3493.

66. Ud-Din, A. and A. Roujeinikova, *Methyl-accepting chemotaxis proteins: a core sensing element in prokaryotes and archaea.* Cellular and Molecular Life Sciences, 2017. **74**(18): p. 3293-3303.

67. Airola, M.V., et al., *HAMP Domain Conformers That Propagate Opposite Signals in Bacterial Chemoreceptors.* Plos Biology, 2013. **11**(2).

68. Kirsch, M.L., et al., *Chemotactic Methylesterase Promotes Adaptation to High-concentrations of Attractant in Bacillus-subtilis.* Journal of Biological Chemistry, 1993. **268**(25): p. 18610-18616.

69. Wu, L., et al., *Genetic and Molecular Characterization of Flagellar Assembly in Shewanella oneidensis.* Plos One, 2011. **6**(6).

70. Li, J., M.F. Romine, and M.J. Ward, *Identification and analysis of a highly conserved chemotaxis gene cluster in Shewanella species.* Fems Microbiology Letters, 2007. **273**(2): p. 180-186.

71. Butler, S.M. and A. Camilli, *Both chemotaxis and net motility greatly influence the infectivity of Vibrio cholerae.* Proceedings of the National Academy of Sciences of the United States of America, 2004. **101**(14): p. 5018-5023.

72. Sourjik, V. and R. Schmitt, *Phosphotransfer between CheA, CheY1, and CheY2 in the chemotaxis signal transduction chain of Rhizobium meliloti.* Biochemistry, 1998. **37**(8): p. 2327-2335.

73. Vladimirov, N. and V. Sourjik, *Chemotaxis: how bacteria use memory.* Biological Chemistry, 2009. **390**(11): p. 1097-1104.

74. Alexander, R.P., et al., *CheV: CheW-like coupling proteins at the core of the chemotaxis signaling network.* Trends in Microbiology, 2010. **18**(11): p. 494-503.

75. Zimmer, M.A., et al., *Selective methylation changes on the Bacillus subtilis chemotaxis receptor McpB promote adaptation.* Journal of Biological Chemistry, 2000. **275**(32): p. 24264-24272.

76. Hamblin, P.A., N.A. Bourne, and J.P. Armitage, *Characterization of the chemotaxis protein CheW from Rhodobacter sphaeroides and its effect on the behaviour of Escherichia coli.* Molecular Microbiology, 1997. **24**(1): p. 41-51.

77. Baraquet, C., et al., *Unexpected chemoreceptors mediate energy taxis towards electron acceptors in Shewanella oneidensis.* Molecular Microbiology, 2009. **73**(2): p. 278-290.

78. Adler, J., *Method for Measuring Chemotaxis and use of Method to Determine Optimum Conditions for Chemotaxis by Escherichia-Coli.* Journal of General Microbiology, 1973. **74**(JAN): p. 77-91.

79. Tso, W.W. and J. Adler, *Negative Chemotaxis in Escherichia-Coli.* Journal of Bacteriology, 1974. **118**(2): p. 560-576.

80. Armitano, J., et al., *The chemical-in-mu well: a high-throughput technique for identifying solutes eliciting a chemotactic response in motile bacteria.* Research in Microbiology, 2011. **162**(9): p. 934-938.

81. Nealson, K.H., D.P. Moser, and D.A. Saffarini, *Anaerobic Electron-Acceptor Chemotaxis in Shewanella-Putrefaciens.* Applied and Environmental Microbiology, 1995. **61**(4): p. 1551-1554.

82. Nealson, K., et al., *A Spectrophotometric Method for Monitoring Tactic Responses of Bacteria Under Anaerobic Conditions.* Journal of Microbiological Methods, 1994. **20**(3): p. 211-218.

83. Li, R., et al., *Soluble Electron Shuttles Can Mediate Energy Taxis toward Insoluble Electron Acceptors.* Environmental Science & Technology, 2012. **46**(5): p. 2813-2820.

84. Bencharit, S. and M.J. Ward, *Chemotactic responses to metals and anaerobic electron acceptors in Shewanella oneidensis MR-1.* Journal of Bacteriology, 2005. **187**(14): p. 5049-5053.

85. Li, R., et al., *Shewanella oneidensis MR-1 Chemotaxis in a Diffusion Gradient Chamber.* Environmental Science & Technology, 2011. **45**(3): p. 1014-1020.

86. Li, J., et al., *The chemical-in-plug bacterial chemotaxis assay is prone to false positive responses.* BMC research notes, 2010. **3**(1): p. 77-77.

87. Arrhenius, S.M., John, *Text-book of electrochemistry*. 1902, London: Longmans. 368.

88. Piccolino, M., *Animal electricity and the birth of electrophysiology: The legacy of Luigi Galvani.* Brain Research Bulletin, 1998. **46**(5): p. 381-407.

89. Newman, J. and K.E. Thomas-Alyea, *Electrochemical Systems*. 2004: John Wiley & Sons.

90. Tutunaru, B., et al., *Spectrophotometry and Electrochemistry of Brilliant Blue FCF in Aqueous Solution of NaX.* International Journal of Electrochemical Science, 2017. **12**(1): p. 396-412.

91. Ye, S.J., et al., *One-step fabrication of hollow-channel gold nanoflowers with excellent catalytic performance and large single-particle SERS activity.* Nanoscale, 2016. **8**(32): p. 14932-14942.

92. Tylka, M.M., et al., *Application of Voltammetry for Quantitative Analysis of Actinides in Molten Salts.* Journal of the Electrochemical Society, 2015. **162**(12): p. H852-H859.

93. Kreysa, G., K.-i. Ota, and R.F. Savinell, *Encyclopedia of applied electrochemistry*. 2014, Springer: New York. p. 2169.

94. Culbertson, C.T., S.C. Jacobson, and J.M. Ramsey, *Diffusion coefficient measurements in microfluidic devices.* Talanta, 2002. **56**(2): p. 365-373.

95. Seeber, R., C. Zanardi, and G. Inzelt, *Links between electrochemical thermodynamics and kinetics.* Chemtexts, 2015. **1**(4).

96. E.R. Cohen, T.C., J.G. Frey, B. Holmström, K. Kuchitsu,. R. Marquardt, I. Mills, F. Pavese, M. Quack, J. Stohner,. H.L. Strauss, M. Takami, and A.J. Thor, *Quantities, Units and Symbols in Physical Chemistry*. 2nd ed ed. IUPAC Green Book. 1993, Oxford: Blackwell Scientific Publications.

97. Silverstein, T.P., *The reaction quotient is unnecessary to solve equilibrium problems.* Journal of Chemical Education, 2005. **82**(8): p. 1149-1149.

98. Bard, A.J. and L.R. Faulkner, *Electrochemical Methods: Fundamentals and Applications*. 2000: Wiley.

99. Oldham, K.B., J.C. Myland, and A.M. Bond, *Electrochemical Science and Technology: Fundamentals and Applications*. Electrochemical Science and Technology: Fundamentals and Applications. 2012. 1-405.

100. Gerischer, H., *Electrode Processes.* Annual Review of Physical Chemistry, 1961. **12**: p. 227-254.

101. Peleg, M., M.D. Normand, and M.G. Corradini, *The Arrhenius Equation Revisited.* Critical Reviews in Food Science and Nutrition, 2012. **52**(9): p. 830-851.

102. Laidler, K.J. and M.C. King, *The Development of Transition-State Theory.* Journal of Physical Chemistry, 1983. **87**(15): p. 2657-2664.

103. D'Souza, S.F., *Microbial biosensors.* Biosensors & Bioelectronics, 2001. **16**(6): p. 337-353.

104. Baron, D., et al., *Electrochemical Measurement of Electron Transfer Kinetics by Shewanella oneidensis MR-1.* Journal of Biological Chemistry, 2009. **284**(42): p. 28865-28873.

105. Breuer, M., et al., *Multi-haem cytochromes in Shewanella oneidensis MR-1: structures, functions and opportunities.* Journal of the Royal Society Interface, 2015. **12**(102).

106. Firer-Sherwood, M., G.S. Pulcu, and S.J. Elliott, *Electrochemical interrogations of the Mtr cytochromes from Shewanella: opening a potential window.* Journal of Biological Inorganic Chemistry, 2008. **13**(6): p. 849-854.

107. Kotloski, N.J. and J.A. Gralnick, *Flavin electron shuttles dominate extracellular electron transfer by Shewanella oneidensis.* Mbio, 2013. **4**(1): p. e00553-12.

108. Artyushkova, K., et al., *Relationship between surface chemistry, biofilm structure, and electron transfer in Shewanella anodes.* Biointerphases, 2015. **10**(1): p. 019013.

109. Peng, L., S.-J. You, and J.-Y. Wang, *Electrode potential regulates cytochrome accumulation on Shewanella oneidensis cell surface and the consequence to bioelectrocatalytic current generation.* Biosensors & Bioelectronics, 2010. **25**(11): p. 2530-2533.

110. Stamou, D., et al., *Uniformly flat gold surfaces: Imaging the domain structure of organic monolayers using scanning force microscopy.* Langmuir, 1997. **13**(9): p. 2425-2428.

111. Boubour, E. and R.B. Lennox, *Stability of omega-functionalized self-assembled monolayers as a function of applied potential.* Langmuir, 2000. **16**(19): p. 7464-7470.

112. Sharma, R., et al., *Label-free electrochemical impedance biosensor to detect human interleukin-8 in serum with sub-pg/ml sensitivity.* Biosensors & Bioelectronics, 2016. **80**: p. 607-613.

113. Okamoto, A., et al., *Uptake of self-secreted flavins as bound cofactors for extracellular electron transfer in Geobacter species.* Energy & Environmental Science, 2014. **7**(4): p. 1357-1361.

114. Worrall, J.A.R., et al., *Myoglobin and cytochrome b_5: A nuclear magnetic resonance study of a highly dynamic protein complex.* Biochemistry, 2002. **41**(39): p. 11721-11730.

115. Coursolle, D. and J.A. Gralnick, *Reconstruction of extracellular respiratory pathways for iron(III) reduction in Shewanella oneidensis strain MR-1.* Frontiers in Microbiology, 2012. **3**: p. 56.

116. Emde, R., A. Swain, and B. Schink, *Anaerobic Oxidation of Glycerol by Escherichia-coli in an Amperometric Poised-Potential Culture System.* Applied Microbiology and Biotechnology, 1989. **32**(2): p. 170-175.

117. Chourey, K., et al., *Transcriptome analysis reveals response regulator SO2426-mediated gene expression in Shewanella oneidensis MR-I under chromate challenge.* BMC Genomics, 2008. **9**: p. 395.

118. Lower, B.H., et al., *Specific bonds between an iron oxide surface and outer membrane cytochromes MtrC and OmcA from Shewanella oneidensis MR-1.* Journal of Bacteriology, 2007. **189**(13): p. 4944-4952.

119. Meitl, L.A., et al., *Electrochemical interaction of Shewanella oneidensis MR-1 and its outer membrane cytochromes OmcA and MtrC with hematite electrodes.* Geochimica et Cosmochimica Acta, 2009. **73**(18): p. 5292-5307.

120. Singh, S. and N. Verma, *Graphitic carbon micronanofibers asymmetrically dispersed with alumina-nickel nanoparticles: A novel electrode for mediatorless microbial fuel cells.* International Journal of Hydrogen Energy, 2015. **40**(17): p. 5928-5938.

121. Luo, Z., et al., *Preparation of Highly Dispersed Reduced Graphene Oxide Decorated with Chitosan Oligosaccharide as Electrode Material for Enhancing the Direct Electron Transfer of Escherichia coli.* Acs Applied Materials & Interfaces, 2015. **7**(16): p. 8539-8544.

122. Du, J., C. Catania, and G.C. Bazan, *Modification of Abiotic-Biotic Interfaces with Small Molecules and Nanomaterials for Improved Bioelectronics.* Chemistry of Materials, 2014. **26**(1): p. 686-697.

123. Cornejo, J.A., et al., *Surface Modification for Enhanced Biofilm Formation and Electron Transport in Shewanella Anodes.* Journal of the Electrochemical Society, 2015. **162**(9): p. H597-H603.

124. Liu, Y. and D.R. Bond, *Long-Distance Electron Transfer by G. sulfurreducens Biofilms Results in Accumulation of Reduced c-Type Cytochromes.* Chemsuschem, 2012. **5**(6): p. 1047-1053.

125. Sun, D., et al., *The effect of biofilm thickness on electrochemical activity of Geobacter sulfurreducens.* International Journal of Hydrogen Energy, 2016. **41**(37): p. 16523-16528.

126. Liu, T., et al., *Enhanced Shewanella biofilm promotes bioelectricity generation.* Biotechnology and Bioengineering, 2015. **112**(10): p. 2051-2059.

127. Kitayama, M., et al., *Structures, compositions and activities of live Shewanella biofilms formed on graphite electrodes in electrochemical flow cells.* Applied and environmental microbiology, 2017.

128. Okamoto, A., K. Hashimoto, and R. Nakamura, *Long-range electron conduction of Shewanella biofilms mediated by outer membrane C-type cytochromes.* Bioelectrochemistry, 2012. **85**: p. 61-65.

129. Lin, T., et al., *Synthetic Saccharomyces cerevisiae-Shewanella oneidensis consortium enables glucose-fed high-performance microbial fuel cell.* Aiche Journal, 2017. **63**(6): p. 1830-1838.

130. Deng, L., et al., *To boost c-type cytochrome wire efficiency of electrogenic bacteria with Fe3O4/Au nanocomposites.* Chemical Communications, 2010. **46**(38): p. 7172-7174.

131. Thormann, K.M., et al., *Initial phases of biofilm formation in Shewanella oneidensis MR-1.* Journal of Bacteriology, 2004. **186**(23): p. 8096-8104.

132. Harris, H.W., M.Y. El-Naggar, and K.H. Nealson, *Shewanella oneidensis MR-1 chemotaxis proteins and electron-transport chain components essential for congregation near insoluble electron acceptors.* Biochemical Society Transactions, 2012. **40**: p. 1167-U29.

133. Harris, H.W., et al., *Electrokinesis is a microbial behavior that requires extracellular electron transport.* Proceedings of the National Academy of Sciences of the United States of America, 2010. **107**(1): p. 326-331.

134. Kim, B.J., et al., *Oxygen Tension and Riboflavin Gradients Cooperatively Regulate the Migration of Shewanella oneidensis MR-1 Revealed by a Hydrogel-Based Microfluidic Device.* Frontiers in Microbiology, 2016. **7**.

135. Bryant, C., D. Atha, and V. Reipa, *Electrochemical Potential Gradient as a Quantitative in Vitro Test Platform for Cellular Oxidative Stress.* Antioxidants, 2016. **5**(3).

136. Peterson, B.W., et al., *Bacterial Cell Surface Damage Due to Centrifugal Compaction.* Applied and Environmental Microbiology, 2012. **78**(1): p. 120-125.

137. Pembrey, R.S., K.C. Marshall, and R.P. Schneider, *Cell surface analysis techniques: What do cell preparation protocols do to cell surface properties?* Applied and Environmental Microbiology, 1999. **65**(7): p. 2877-2894.

138. Gilbert, P., F. Caplan, and M.R.W. Brown, *Centrifugation Injury of Gram-negative Bacteria.* Journal of Antimicrobial Chemotherapy, 1991. **27**(4): p. 550-551.

139. Losic, D., J.G. Shapter, and J.J. Gooding, *Influence of surface topography on alkanethiol SAMs assembled from solution and by microcontact printing.* Langmuir, 2001. **17**(11): p. 3307-3316.

140. Hou, Z.Z., N.L. Abbott, and P. Stroeve, *Electroless gold as a substrate for self-assembled monolayers.* Langmuir, 1998. **14**(12): p. 3287-3297.

141. Lee, S., et al., *Scanning tunneling microscopy of template-stripped Au surfaces and highly ordered self-assembled monolayers.* Langmuir, 2008. **24**(12): p. 5984-5987.

142. Hu, Y., et al., *Trajectory energy minimization for cell growth tracking and genealogy analysis.* Royal Society Open Science, 2017. **4**(5).

143. Balomenos, A.D., et al., *Tracking Single-Cells in Overcrowded Bacterial Colonies*, in *2015 37th Annual International Conference of the Ieee Engineering in Medicine and Biology Society*. 2015. p. 6473-6476.

144. Cai, Q.X., et al., *Singly Flagellated Pseudomonas aeruginosa Chemotaxes Efficiently by Unbiased Motor Regulation.* Mbio, 2016. **7**(2).

145. Crocker, J.C. and D.G. Grier, *Methods of digital video microscopy for colloidal studies.* Journal of Colloid and Interface Science, 1996. **179**(1): p. 298-310.

146. Stuij, S.G., et al., *Critical Casimir interactions between colloids around the critical point of binary solvents.* Soft Matter, 2017. **13**(31): p. 5233-5249.

147. Marshall, M.J., et al., *c-Type cytochrome-dependent formation of U(IV) nanoparticles by Shewanella oneidensis.* Plos Biology, 2006. **4**(8): p. 1324-1333.

148. Nisenbaum, M., et al., *Video processing analysis for the determination and evaluation of the chemotactic response in bacterial populations.* Journal of Microbiological Methods, 2016. **127**: p. 146-153.

149. Stocker, R., *Reverse and flick: Hybrid locomotion in bacteria.* Proceedings of the National Academy of Sciences of the United States of America, 2011. **108**(7): p. 2635-2636.

150. Xie, L., et al., *Bacterial flagellum as a propeller and as a rudder for efficient chemotaxis.* Proceedings of the National Academy of Sciences of the United States of America, 2011. **108**(6): p. 2246-2251.

151. Edwards, M.J., et al., *Comparative structure-potentio-spectroscopy of the Shewanella outer membrane multiheme cytochromes.* Current Opinion in Electrochemistry, 2017. **4**(1): p. 199-205.

152. Coursolle, D., et al., *The Mtr Respiratory Pathway Is Essential for Reducing Flavins and Electrodes in Shewanella oneidensis.* Journal of Bacteriology, 2010. **192**(2): p. 467-474.

153. Lee, J.S. and B.J. Little, *Technical Note: Electrochemical and Chemical Complications Resulting from Yeast Extract Addition to Stimulate Microbial Growth.* Corrosion, 2015. **71**(12): p. 1434-1440.

154. Flynn, J.M., et al., *Enabling Unbalanced Fermentations by Using Engineered Electrode-Interfaced Bacteria.* Mbio, 2010. **1**(5).

155. Foley, J.M., et al., *Life Cycle Assessment of High-Rate Anaerobic Treatment, Microbial Fuel Cells, and Microbial Electrolysis Cells.* Environmental Science & Technology, 2010. **44**(9): p. 3629-3637.